

ABSTRACT

XIN, JIA. SPIN DIFFUSION NMR INVESTIGATIONS OF AMORPHOUS POLYMER ORGANIZATION IN THE SOLID STATE

(Under the direction of Professor Jeffery L. White)

We report a general method, based on intramolecular spin-diffusion, for the measurement and calculation of spin-diffusion coefficients in amorphous polymers and their blends using only NMR data. The basic structural unit that defines ^1H polarization density in polymers is the monomer unit. Using appropriately selected internal reference distances calculated from energy-minimized chain dimension simulations, timescales for the redistribution of ^1H polarization *within* amorphous homopolymers may be used to *independently* calculate maximum values of the spin diffusion coefficients D . This strategy represents an attractive alternative to current methods employed for domain size measurements in polymer blends, which require calibration of spin diffusion coefficients based on comparisons of similar NMR data obtained on model compounds analyzed previously using scattering or microscopy techniques. In this way, many more polymer systems become amenable to study by NMR spin-diffusion methods, since X-ray scattering or microscopy calibrations on representative standards are no longer necessary to define quantitative limits on spin-diffusion coefficients. Experimentally, the fate of proton magnetization is followed with high selectivity using 2D ^1H - ^{13}C solid-state HETCOR sequences incorporating controlled periods of ^1H - ^1H spin-diffusion.

**SPIN DIFFUSION NMR INVESTIGATIONS OF
AMORPHOUS POLYMER ORGANIZATION
IN THE SOLID STATE**

by

XIN JIA

A dissertation submitted to the Graduate Faculty of

North Carolina State University

In partial fulfillment of the

Requirements for the degree of

Doctor of Philosophy

In

CHEMISTRY DEPARTMENT

Raleigh, NC

2004

Approved by:

Alex. I. Smirnov

E. O. Stejskal

Alan E. Tonelli

Jeffery L. White

Chair of Advisory Committee

I dedicate this work to my beautiful and supporting wife,

June Ding

And to my parents who always believe in me and

encourage me to excel

BIOGRAPHY

Xin Jia, the author, was born in Zhe Jiang Province, China in 1974. He graduated from Fudan University in Shanghai with a Bachelor of Science degree in Chemistry. Xin Jia came to Chemistry Department in North Carolina State University to pursue his PhD degree in 2000. He was advised by Professor Jeffery L. White and focused on polymer science and NMR spectroscopy.

Xin Jia was married to June, Ding, and they will have 3 children, potentially 2 boys and one girl.

ACKNOWLEDGMENTS

I would like to take this opportunity to express my sincere gratitude to all who helped me and encouraged me.

The first one I want to thank is my advisor, Professor Jeffery L. White, Chair of my advisory committee, for his guidance, support, consideration, caring and encouragement in the course of my studies and my life. Also I'd like to thank other members of my advisory committees: Professor Alan E. Tonelli, Professor Alex Smirnov, and Professor E. O. Stejskal for their support. Special thank goes to Professor E.O. Stejskal for his kind help and numerous instructive talks about the research and many wonderful contents. I also want to express my gratitude to Dr. Xingwu Wang for his endless help.

I want to thank the following people: Dr. Hanna Gracz, Marcus Hunt, Cristian Rusa. Many thanks to my colleagues and friends: Justyna E. Wolak, Stan S. Toporak, Matthew J. Truitt, Rosimar Rovira-Hernandez. Electronic instrument shop personnels , Mr. Eddie Barefoot, Mr. Tony Radford, Mr. Leonard Page, Mr. Alan Harvel are appreciated for their technical help.

Finally, I would like to express my deep gratitude to my family members, especially my lovely wife for her support and love.

TABLE OF CONTENTS

LIST OF FIGURES	vii
LIST OF TABLES	xi
Chapter 1. Motivation and Introduction	1
1. Motivation.....	1
2. History of NMR.....	5
2.1. Unique features of NMR.....	5
2.2. Discovery of NMR.....	5
3. Short review of the solid-state NMR theory.....	9
3.1. Basics of NMR.....	9
3.2. Essential techniques for solid-state NMR ^{1,32}	16
3.3. Special solid-state NMR sequences.....	28
3.3.1. T ₁ , T ₂ and T _{1ρ}	28
3.3.2. Spin diffusion and spin-diffusion solid-state NMR.....	31
3.3.3. Goldman-Shen experiment – the simplest ¹ H Spin Diffusion Experiment.....	34
Chapter 2. New Method for Determination of Spin-Diffusion Coefficients	36
1. NMR method: 2D solid-state heteronuclear ¹ H- ¹³ C Correlation experiment ...	36
2. Polymers	39
3. Simulation of polymer chain units.....	40
4. Data analysis and Discussion.....	41
5. Heterogeneous systems.....	53
6. Conclusions.....	59
Chapter 3. Enhanced Spin-Diffusion Curves in Solid Polymers by Two-Dimensional Lee-Goldburg and Windowless Multiple-Pulse Experiments.....	60
1. Introduction.....	60
2. Experimental Section.....	61
2.1. Materials	61
2.2. Solid-state NMR methods.....	61
2.2.1. Multipule-pulse Windowless Isotropic Mixing Heteronuclear Correlation Spin Diffusion Experiment (MP-WIM Hetcor).....	61
2.2.2. Frequency-switched Lee-Goldburg Heteronuclear Correlation Spin Diffusion Experiment (FSLG/HHCP Hetcor).....	62
3. Results and Discussion	64
4. Conclusions and Future Work	78
Chapter 4. Two-Dimensional Spin Diffusion NMR Reveals Differential Mixing in Biodegradable Polyester Blends	80
1. Introduction.....	80
2. Experimental section.....	82
2.1. Sample Preparation.....	82
2.2. Solid-state NMR Methods	83
2.3. Simulation of Polymer Chain Units.....	86
3. Results and Discussion	86
4. Conclusions.....	101
Chapter 5. Conclusions and Future Directions.....	102
References:.....	103

APPENDICES	112
MP-WIM Pulse Program used at Bruker Avance 300 MHz instrument.	112
FSLG-LGCP Pulse Program used at Bruker Avance 300 MHz instrument.	115
Preparation and Characterization of Poly (acetoxystyrene)/Poly (ethylene oxide) Blends	117
Polymer-Clay Nanocomposites: Preparation and Characterization.....	118

LIST OF FIGURES

Figure 1. The classical vector model of nuclear spins in a sample.	9
A. In the absence of an applied magnetic field, the nuclear spins (represented by vector arrows) are disordered in their ground states, there are no energy differences between them, and as a result, there is no net nuclear magnetization in the system.	10
B. After applied an external magnetic field B_0 , the nuclear spin vectors reorient parallel or anti-parallel to the applied B_0 field according to the Boltzmann distribution thermal effects, creating net nuclear magnetization.	10
Figure 2. Without an external magnetic field B_0 ($B_0 = 0$), there are no energy differences between all the nuclear spins in a bulk sample. After applying an external magnetic field B_0 ($B_0 > 0$), the thermal effect generates the population difference between the spin up α and spin down β levels according to the Boltzmann distribution.	11
Figure 3. Laboratory frame and rotating frame in the nuclear magnetic field.	14
At rotating frame, the time dependence of the B_1 field will be removed and it will appear to be static.	14
Figure 4. The rotating frame rotates about the z-axis at the frequency of the rf pulse, ω_{rf}	15
Figure 5. On-resonance 90° (a) and 180° (b) rf pulses that flip the nuclear magnetic spins to y' and $-z$ axis, respectively.	16
Figure 6. The magic angle spinning scheme in solid-state NMR experiment. (following reference 5)	19
Figure 7. The effects of magic angle spinning on homonuclear dipole-dipole interaction. The broad line is narrowed by magic angle spinning rates of the order of the dipolar linewidth or higher. For slow MAS speed, broad spinning sidebands appear, and at very slow speed, there is no big effect of removing any of the effects.	21
Figure 8. High power proton dipolar decoupling removes the effects of proton dipolar coupling from the ^{13}C solid-state NMR spectrum. High power irradiation is applied to the ^1H spins at the proton on-resonance frequency during the acquisition of the ^{13}C spin NMR spectrum.	22
Figure 9. Multiple pulse sequences used for removing homonuclear dipolar coupling from solid-state NMR spectrum. In (a) WAHUA (after Waugh, Huber, and HAbleren) ³⁹ sequence and in (b) MREV-8 (after Mansfield, Rhim, Elleman, and Vaughan) ^{40,41} sequences, all pulses are 90° pulses with the indicated phases, multiple times (as indicated by the arrows.) The MREV-8 sequence is actually a two phase-cycled WAHUA sequence.	23
Figure 10. Cross polarization achieved by the Hartmann-Hahn condition, $\gamma_{13\text{C}}B_1 = \gamma_{1\text{H}}B_1'$	25
Figure 11. Cross Polarization Pulse Sequence.	26
Figure 12. CP/MAS spectrum for hexamethyl benzene (HMB).	28
Figure 13. Classical flip-flop of two magnetic dipoles.	31
Figure 14. Schematic Representation of ^1H spin diffusion process. (following reference 26)	33
Figure 15. Goldman-Shen experiment sequence demonstrating ^1H spin diffusion.	34

Figure 16. 2D Solid-State Heteronuclear Correlation pulse sequence (HetCor). Typical experimental parameters include 90° pulse widths 3.2 μs on each channel, spinning speeds 3.5-4.5 kHz, 256-512 scans for each 64 points in t ₁ dimension, typical experimental time 12-24 hours.	37
Figure 17. PC (poly (bisphenol A carbonate)) and PPO (poly (2,6-dimethyl-1,4-phenylene oxide)) simulated chain units.....	40
Figure 18. Simulated structure for a PPO chain demonstrating how the characteristic monomer dimension $x = (l_{cd})^{1/2}$ was calculated.	41
Figure 19. 2D HetCor spectra obtained for PC with spin-diffusion times of (A) 0, (B) 0.1, (C) 3 ms. Note in particular the time-dependent cross-peak intensities for the CH ₃ and aromatic CH groups.	44
Figure 20. (a) The ¹³ C slices at the methyl ¹ H peak (top) and the aromatic ¹ H peak (bottom) for τ _m = 0. (b) The ¹ H slices at the 31 ppm methyl ¹³ C peak (top) and the 128 ppm aromatic ¹³ C peak (bottom) for τ _m = 0. (c) The ¹³ C slices at the methyl ¹ H peak (top) and the aromatic ¹ H peak (bottom) for τ _m = 1 ms. (d) The ¹ H slices at the 31 ppm methyl ¹³ C peak (top) and the 128 ppm aromatic ¹³ C peak (bottom) for τ _m = 1 ms.	45
Figure 21. Spin-diffusion curves for PC constructed from deconvolution of the ¹ H slices at the methyl (31 ppm) and aromatic (128 ppm) ¹³ C shifts in terms of the integrated intensity ratio of (I _{aromatic} / (I _{aromatic} + I _{aliphatic})).	47
Figure 22. 2D HetCor spectra obtained for PPO with spin-diffusion times of (A) 0 ms, (B) 0.05 ms, (C) 3 ms.....	50
Figure 23. Complete spin-diffusion curves for the 2D HetCor experiments for PPO. Here the growth of the aliphatic ¹ H correlation at the 120 ppm aromatic ¹³ C chemical shift is plotted as a function of the square root of the spin-diffusion mixing time.	51
Figure 24. Simulated structure for the PC, where the cylinder inscribes the “effective” monomer size.	53
Figure 25. (top) 2D HetCor spectrum for a monodisperse PS-b-PMMA diblock copolymer obtained using a 5 ms spin-diffusion time, with the summed cross-peak projection for the ¹³ C dimension shown on the top of the plot. (bottom) Selected ¹ H slices through the 128 ppm PS peak as a function of spin-diffusion time τ(tau); the dashed line on the contour plot indicates the slice position.	56
Figure 26. Complete spin-diffusion curves for the PS-b-PMMA in which the ratio of (I _{aliphatic} / (I _{aromatic} + I _{aliphatic})) is plotted vs the square root of the mixing time for the 128 ppm peak. Intramolecular spin-diffusion leads to the short time equilibration with the PS chains, followed by a longer intermolecular polarization transfer between the PS and PMMA blocks.	57
Figure 27. Two dimensional frequency-switched Lee-Goldburg with Hartmann-Hahn Cross-polarization heteronuclear correlation pulse sequence (FSLG/HHCP Hetcor). 1H r.f field strength during FSLG evolution period and TPPM decoupling period were set at 90-95 kHz, correspond with π/2 pulse of 2.65-2.75 μs. A ramp Hartman-hahn cross-polarization pulse is used; cross-polarization time is about 100 us. Magic angle spinning speed should be high than 10 kHz to reduce the dipolar interaction.	64
Figure 28. Representative 2D ¹ H- ¹³ C HetCor plot of the 50K PS-b-PMMA copolymer at a spin-diffusion time of 1 ms for (a) MP-WIM vs. (b) FSLG experiment, demonstrating slightly improved resolution in the ¹ H dimension for the latter. Selected ¹ H slices at the PS aromatic CH signal (indicated by dashed line) are shown below the 2D plots,	

indicating how the spin-diffusion curves in subsequent figures were extracted from the 2D experiments. For the MP-WIM HetCor, MAS spinning speeds of 3.5 – 4.5 kHz were used, while the FSLG HetCor data were collected at 12-13 kHz. Quadrature detection in the second dimension (using TPPI) was insured by appropriate phase cycling and data addition for both the MP-WIM and FSLG experiments^{43,103}. Approximately 40 mg of sample in a 4-mm MAS rotor was used for the MP-WIM experiments, whereas only 10 mg was used for the FSLG data (due to confinement in the most homogeneous region of the r.f. coil)..... 66

Figure 29. Total spin-diffusion curves obtained using Lee-Goldburg (FSLG) vs. multiple-pulse Hetcor (MP-WIM) for (a) PS-b-PMMA with a total molecular weight of 50K (25K blocks for each component); (b) PS-b-PMMA with a total molecular weight of 100K; (c) PS-b-PMMA with a total molecular weight of 200K. In (d), a schematic of a typical spin-diffusion curve resulting from the measurement of only interdomain polarization transfer is shown. The lines are drawn merely to guide the eye in examining the different responses. 72

Figure 30. (a) MP-WIM spin-diffusion curves for PS-b-PMMA with a total molecular weight of 50K, in which the same 2D Hetcor data set was analyzed twice (phasing, slice selection, deconvolution, and intensity ratio determination). (b) MP-WIM spin-diffusion curve for PS-b-PMMA 100K with representative error bars determined by triplicate experiments on four randomly selected spin-diffusion mixing times (details described in the text). (c) MP-WIM spin-diffusion curve for PS-b-PMMA 100K obtained at two different MAS speeds. (d) Plot of 128-ppm PS aromatic C-H slice intensity versus MAS speed for MP-WIM spin-diffusion experiment at two different spin-diffusion times..... 77

Figure 31. Two dimensional Frequency-switched Lee-Goldburg heteronuclear correlation experiment with Lee-Goldburg cross-polarization pulse sequence. ¹H radiofrequency field strength during FSLG evolution period and TPPM decoupling period were set at 90-95 kHz, correspond with $\pi/2$ pulse of 2.65-2.75 μ s. At ¹H LGCP period, radiofrequency field strength is 64-68 kHz, correspond with $\pi/2$ pulse of 3.7-3.9 μ s. ¹³C ramp CP is used, CP time = 100 μ s. MAS speed = 13 kHz. Quadrature detection in t_1 is achieved by TPPI. 84

Figure 32 (a) ¹H Bloch decay spectrum of pure bulk PCL; (b) ¹H Bloch decay spectrum of pure bulk PLLA; (c) ¹H Bloch decay spectrum of coalesced PCL/PLLA blend; (d) ¹³C CP/MAS spectrum for the solution PCL/PLLA blend; (e) ¹³C CP/MAS spectrum for the same sample as in (c). Assignments follow the structure schematic (top). Spectra (a) – (c) were acquired with 13 kHz MAS. Asterisks denote spinning sidebands..... 89

Table 1. ¹H rotating-frame spin-lattice relaxation time constants $T_{1\rho H}$ (in milliseconds) for PCL/PLLA blends versus sample preparation method. 90

Figure 33. Representative two-dimensional ¹H-¹³C solid-state Hetcor plots of the aliphatic ¹³C region for: (a) FSLG/LGCP acquisition on the solvent-cast blend with no spin-diffusion time; (b) same as (a), after 1 ms spin-diffusion time; (c) MP/WIM acquisition on the coalesced blend with no spin-diffusion time; (d) same as (c), after 1 ms mixing time. ¹H slices were extracted at 19 ppm and 65 ppm for the spin-diffusion analysis. Summed projections from each dimension are shown along the ¹³C (horizontal) and ¹H (vertical) axes..... 93

Figure 34. ¹H Spin-diffusion curves extracted from slices at the PLLA CH₃ signal (19 ppm) for the solution-cast (■) and coalesced (●) PCL/PLLA blends. The horizontal

arrows indicate the predicted equilibrium intensity ratios for intramonomer vs. intermolecular (interdomain) spin-diffusion based on the monomer structures. The dashed line in the short time regime is the regression through the first five points of the curve to the intramolecular equilibrium intensity ratio (0.25). From this latter analysis, the equilibration time for intramolecular spin-diffusion was $20 \mu\text{s}^{1/2}$ (τ_{intra} vertical arrow). Additional vertical arrows indicate the equilibration times for intermolecular or interdomain spin-diffusion between PLLA and PCL in the coalesced ($\tau_{\text{coal}} = 88 \mu\text{s}^{1/2}$) and solution-cast ($\tau_{\text{sol}} = 132 \mu\text{s}^{1/2}$) blends, obtained by regression of the four experimental points between the intramolecular and intermolecular plateaus. 94

Figure 35. ^1H Spin-diffusion curve from pure PLLA (■) vs. PLLA in the coalesced blend with PCL(●), demonstrating a decrease in the spin-diffusion coefficient D upon blending. The last data point for the PLLA/PCL coalesced blend is already at the intermolecular equilibrium value, as previously seen in Figure 32. 98

The value of $D_{\text{PLLA}}^{\text{pure}} = 2.1 \times 10^{-12} \text{ cm}^2 \text{ s}^{-1}$ is in agreement with our previous determinations of D 's based on intramonomer spin-diffusion^{94,128}. For the higher- T_g polycarbonate ($T_g = 140 \text{ }^\circ\text{C}$) and lower- T_g polyisobutylene ($T_g = -70 \text{ }^\circ\text{C}$), the previously reported spin-diffusion coefficients were $5.1 \times 10^{-12} \text{ cm}^2 \text{ s}^{-1}$ and $4.4 \times 10^{-14} \text{ cm}^2 \text{ s}^{-1}$, respectively. Since the PLLA T_g is intermediate between these two extreme ($T_g = 60 \text{ }^\circ\text{C}$), an intermediate value of D expected. 98

Figure 36. Biexponential fit for ^1H spin-diffusion curves extracted from slices at the PLLA CH_3 signal (19 ppm) for the coalesced (●) PCL/PLLA blends at figure 32. The biexponential equation is $f = a*(1-\exp(-b*x)) + c*(1-\exp(-d*x))$, the parameters are as following: $a = 2.4302$, $b = 0.0547$, $c = -2.2202$, $d = 0.0495$ $R^2 = 0.948$. The solid line is the two-component fit, with the short time response attributed to intramolecular polarization equilibration, and the long time component to interdomain spin-diffusion. 99

Figure 37. Expanded Hetcor plot of the OCH and OCH_2 region of the spectrum showing that the broad downfield (in the ^{13}C dimension) shoulder off the PLLA peak is clearly correlated to an upfield ^1H shift. 100

LIST OF TABLES

Table 1. ^1H rotating-frame spin-lattice relaxation time constants $T_{\rho\text{H}}$ (in milliseconds) for PCL/PLLA blends versus sample preparation method.	90
Table 2. ^1H spin-lattice relaxation time constants T_1 (in seconds) for PCL/PLLA blends versus sample preparation method.	90

Chapter 1. Motivation and Introduction

1. Motivation

The physical properties of solid polymers, such as thermal, mechanical, electrical, optical, barrier, and ageing mostly depend on two aspects. First, they are determined by their molecular structures, which are their internal properties, and can be cautiously controlled by various chemical syntheses. Secondly, their physical properties also strongly dependent on the structural organization of the macromolecules in the solid state, including morphology, local structure, phase behavior, and molecular dynamics^{1,2,3}. To improve and optimize macromolecular behavior and mechanical properties one needs to understand the structure-property relationships. To deepen the knowledge, the focus needs to be on the development of modern experimental techniques, which can probe microscopic and molecular parameters in the solid state^{1,4} for amorphous macromolecules.

In order to understand the polymers' physical properties, one can divide them into three categories based on length scales⁶. They are (1) the molecular (microscopic) level, at this level, the intra- and intermolecular interactions determine the behavior of the macromolecules properties. The local structure of the polymer chain will organize into a bulk structure, thus generating a variety of physical properties, and making a useful material. (2) the supermolecular(mesosopic) level, at this level, the individual polymer chains aggregate into polymorphs, forming crystalline and amorphous sub-regions. Chain packing becomes extremely important in this level. (3) the morphological level, at this

level, the crystalline and amorphous regions organize respectively into morphological region.

The macroscopic physical properties of polymers are governed by all three length scale levels. Various experimental techniques can be used to probe the microscopic properties^{6,7}. Fourier transform infrared (FT-IR)⁸ and raman spectroscopy⁹ can determine the molecular scale characterization. Small angle X-ray scattering (SAXS)^{10,11}, wide angle X-ray scattering (WAXS)^{12,13,14}, neutron diffraction^{15,16,17,18}, electron scattering¹⁹ and electron microscopy (TEM^{19,20}, SEM^{20,21}, AFM²²) techniques can be used to characterize the macromolecular local order.

X-ray scattering is one of the classic techniques used for polymer characterization. It provides information to answer the question about whether a polymer is crystalline or amorphous, oriented or unoriented and to determine the size of characteristic repeat distances. Also, it can determine the structural information such as the unit cell, space group and atomic coordinates of a crystalline or semicrystalline polymer, which relates to polymer's atomic scale but is averaged over the sample volume (typically on a scale of μm to mm). The WAXS experiment is primarily used as the diffraction measurement over wider angles ($10 - 40^\circ$) and spacing between 1 and 1.1 nm. It can provide valuable information about the morphology in the crystalline region in a polymer¹²⁻¹⁴. Studies show that the WAXS experiment provides better results on heavy atoms but is less sensitive to the lighter atoms such as hydrogen. Neutron scattering can observe the location of hydrogen atoms in a lattice¹⁵⁻¹⁸. The contrast between the scattering cross-sections of hydrogen and deuterium can be used to characterize the distribution of a single labeled chain within a low scattering matrix. Although in principle deuteration does not essentially change the structure of the polymer, studies show that the

thermodynamics between the protonated and deuterated polymer may be different. This concerns whether the local structures of the polymer have been changed by the insertion of the labeled polymer. Electron scattering and electron microscopy techniques are based on high energy electrons scattering in the polymer structure and the diffraction patterns resemble those obtained from X-rays. Electron scattering is mainly applied to very highly crystalline materials. The resolution of these techniques can be at the 0.1 nm level and provides useful information that is below the resolution limit of the conventional optical microscope. Transmission electron microscopy (TEM) has been used to visualize the chain packing in polyethylene type polymer²⁰. This method required the section of the samples below 100 nm, which allow the electron beam to pass through the material. The TEM method can provide electron diffraction data that can be used to calculate the molecular spacing in crystalline phases in the polymer material. The alternative approach to electron microscopy is scanning electron microscopy (SEM) ²⁰. In SEM the backscattered electrons contain an energy which is the characteristic of the atoms that produce the scattering²¹. Since the resolution of light atoms such as carbon and oxygen at SEM is very poor, this method is only useful for heavy atoms.

In the past 20 years, solid state nuclear magnetic resonance (SSNMR) advancements have added new possibilities in polymer physical and chemical property characterizations^{1-4,23,24}.

Many of the macroscopic properties of polymers, blends, composites, and their copolymers arise from variation of the physical and chemical local structures. In general, the properties of these local structure organizations can be studied by the well-established techniques, such as light, X-ray, or neutron scattering, scanning or transmission electron

microscopy, and dielectric or mechanical relaxation. However, an experimental determination and characterization of local structure, and the resulting morphology at length scales shorter than about 50 nm in amorphous polymers and other noncrystalline compounds is difficult. In addition, the information content in small-angle X-ray diffraction is often insufficient due to a low contrast⁴.

Recently, solid-state spin diffusion NMR methods have been introduced to interrogate the essential characteristics of the local structure, as well as the morphology of the amorphous macromolecules and their blends. These spin diffusion methods determine the time dependent spin diffusion polarization transfer under the influence of nuclei dipolar interactions. From this, the distance information (domain size for blends, composites, and copolymer) can be obtained with the introduction of a spin diffusion coefficient. Some excellent reviews have been published in this area^{25,26}.

In the following research, we report some general solid-state spin diffusion NMR methods, based on intramolecular spin diffusion, for the measurement and calculation of spin-diffusion coefficients in amorphous polymers and their blends using only NMR data. The basic structural unit that defines ¹H polarization density in polymers is the monomer unit. Using appropriately selected internal reference distances calculated from energy-minimized chain dimension simulations, time scales for the redistribution of ¹H polarization within amorphous homopolymers may be used to independently calculate maximum values of the spin-diffusion coefficient. These methods are able to solve the structure/distance problem from NMR, i.e., spin diffusion coefficient D, without reference to other method because amorphous polymer samples are not amenable to scattering, diffraction techniques.

2. History of NMR

2.1. Unique features of NMR

NMR was rapidly accepted in physics and chemistry and has been applied in many directions because of its inherent, unique features. Since the radiation (Megahertz frequencies) used in NMR experiments is monochromatic, it avoids the burden to render broad-band radiation in other spectroscopic experimental techniques. There are only very small energy changes involved in the transition between nuclear spin energy levels. Thus, the NMR experiment causes only a slight perturbation of the system in contrast to optical spectroscopy experiments. As a result, the information obtained from NMR experiments will represent the bulk properties of the macromolecules. A related point in the NMR experiment is that the spacing of the nuclear spin energy levels increases with the applied external magnetic field, B_0 . Also, the Boltzmann factor is larger at higher fields, increasing the sensitivity further.

2.2. Discovery of NMR

Discovery of Nuclear Magnetic Resonance

NMR was discovered independently by E.M. Purcell and Felix Bloch in 1946²⁷. Both of them shared the Nobel Physics Prize in 1952 "for their development of new methods for nuclear magnetic precision measurements and discoveries in connection therewith".

Fourier Transform NMR Spectroscopy (FT-NMR)

Nuclear Magnetic Resonance (NMR) spectroscopy is one of the most powerful tools in modern science. Since its discovery, NMR has found applications from physics to chemistry, biosciences, material research and medical diagnosis.

The development of NMR as a routine analytical technique in these fields parallels the development of electromagnetic technology. During World War II, Purcell worked on the development and application of RADAR at MIT's Radiation Lab. His work during that project was mainly concerned with the production and detection of radiofrequency energy and the absorption of such energy by matter. This project preceded the discovery of NMR and contributed to his understanding of NMR and related phenomena.

Throughout the next several decades, NMR spectroscopists mostly utilized a technique known as continuous wave (CW) spectroscopy. In continuous wave spectroscopy, either the magnetic field was held constant and the oscillating field was swept in frequency to plot the on-resonance portions of the spectrum, or more frequently, the oscillating field was kept at a fixed frequency, and the magnetic field was swept through the transitions. The limitation of this technique is that it probes each of the frequencies in succession, resulting in a poor signal-to-noise (S/N) ratio.

NMR spectroscopists found that the signal-to-noise ratio (S/N) can be improved by the signal averaging method. The signal averaging method increases signal-to-noise ratio (S/N) by the square-root of the number of signals scanned. A technique called Fourier transform NMR spectroscopy (FT-NMR) (first noted by Norberg) can process the signal averaging time it takes to acquire a scan much faster by allowing a range of frequencies to be scanned immediately. The FT-NMR technique has been made more practical with

the development of modern computers capable of performing the computationally-intensive mathematical transformation of the data from the time domain to the frequency domain, to produce a spectrum.

In the fall of 1963 Richard R. Ernst at Varian Associates in Palo Alto under the guidance of Dr. Weston Anderson, found FT-NMR can significantly increase NMR's signal-to-noise ratio by irradiating the sample with a short radiofrequency pulse. Detectors record the decay of this excitation as a time-dependent pattern, known as the free induction decay (FID). This time-dependent pattern, when processed through the Fourier transform, reveals the frequency-dependent pattern of nuclear resonances, the NMR spectrum. According to Fourier theory, the shorter the pulse, the broader the range of frequencies it contains. R. R. Ernst was awarded the Nobel Prize for chemistry in 1991 "for his contributions to the development of the methodology of high resolution nuclear magnetic resonance (NMR) spectroscopy"²⁷.

The use of pulses of various shapes, frequencies, and durations, in specifically-designed patterns, gives the spectroscopists great flexibility in determining what portions of a molecule, or what intra- and intermolecular dynamic processes, to study. The gain in sensitivity over several decades has opened many new research directions in the following several decades till now, such as the application of high resolution NMR spectroscopy to molecules adsorbed on solid surfaces, and biological macromolecular NMR.

Two and Multi-dimensional NMR Spectroscopy

Two dimensional nuclear magnetic resonance spectroscopy (2D NMR) belongs to the FT-NMR spectroscopy categories where there are at least two pulses, and the time between the pair of pulses is varied. The first dimension is the frequency of the excitation

(t_2), and the second dimension is based on the time differential between the pair of pulses (t_1). The final spectra will be Fourier transformed, expressing the first and second dimension as frequencies (F_1 and F_2). In multidimensional nuclear magnetic resonance spectroscopy, there will be a sequence of pulses, and at least one variable time period. For example, in 3D, two time periods will be varied, while in 4D, three will be varied.

These time intervals allow spin magnetization transfer between nuclei in the external magnetic field and therefore NMR spectroscopists can detect the interactions between nuclei that generate the spin magnetization transfer. The kinds of interactions that can be detected are usually divided into two categories. The first is through-bond interactions, such as J coupling interaction. And the second is through-space interactions, such as dipole-dipole interaction, an example of which is nuclear Overhauser interaction.

Development of Powerful Magnets

Since the intensity of NMR signals, and hence the sensitivity of the technique, depend on the strength of the magnetic field, the NMR technique has also advanced over the decades with the development of more powerful magnets. The commercial magnets were first available around 1953-1955 from M. E. Packard, J. N. Shoolery, and H. E. Weaver. At that time, Varian Associates (Palo Alto, California) had shipped their first three high-resolution NMR spectrometers (frequency at 60 MHz), to the Humble Oil Company in Texas, to the DuPont Experimental Station in Delaware, and to the Shell Development Company in California. Currently, there are 900 MHz to 1 GHz commercial superconducting electromagnets available. These developments of powerful superconducting electromagnets increase the sensitivity of NMR signals manifolds²⁸.

3. Short review of the solid-state NMR theory

3.1. Basics of NMR

Classical vector model of the nuclear spin^{5,30,31}

When looking at a classical model of NMR, we will only consider the net nuclear spin magnetization coming from the nuclei in the sample and its behavior in magnetic fields. Without an applied external magnetic field, all nuclear spins are degenerated meaning they are disordered in their ground states with no energy differences between them (Figure 1A). In this dissertation, we will exclusively deal with spin $\frac{1}{2}$, therefore, here we will only consider the spin $\frac{1}{2}$ conditions. All the nuclear spins have nuclear magnetic moment μ , when they are placed in a strong external magnetic field B_0 , they will reorient either parallel or anti-parallel to the applied nuclear magnetic field B_0 from disordered ground states. Figure 1B shows the nuclear spin reorientation after they are placed in an external magnetic field B_0 .

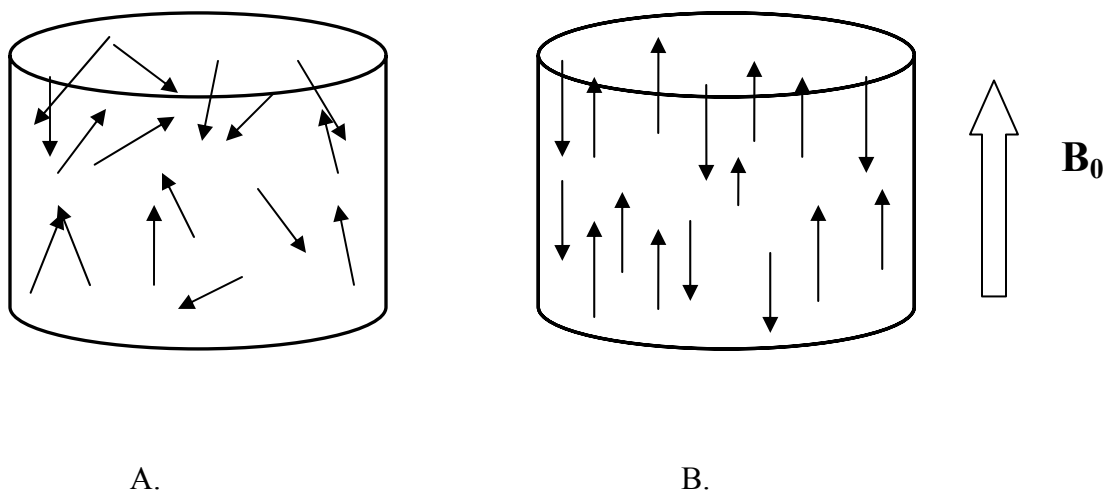


Figure 1. The classical vector model of nuclear spins in a sample.

A. In the absence of an applied magnetic field, the nuclear spins (represented by vector arrows) are disordered in their ground states, there are no energy differences between them, and as a result, there is no net nuclear magnetization in the system.

B. After applied an external magnetic field B_0 , the nuclear spin vectors reorient parallel or anti-parallel to the applied B_0 field according to the Boltzmann distribution thermal effects, creating net nuclear magnetization.

The relationship between the nuclear spin magnetic moment μ and angular momentum L can be defined by the following equation:

$$\mu = \gamma L \quad (1)$$

In this equation, γ is the nuclear spin's magnetogyric ratio. The magnetogyric ratio γ is individual to each type of nuclei. In NMR, the applied magnetic field is generally placed along the z direction. Following the application of a strong external magnetic field B_0 , the nuclear spins will precess about this field at the frequency which is defined by the equation:

$$\omega = -\gamma B_0 \quad (2)$$

The frequency ω is called the Larmor precession frequency of the nuclear spins, γ is the magnetogyric ratio of the nuclei, and B_0 is the applied magnetic field strength. If ω has the traditional units of rad sec^{-1} and the magnetic field B_0 has units of Tesla ($1\text{T} = 10^4$ Gauss), the magnetogyric ratio γ will have the units of $\text{rad sec}^{-1} \text{T}^{-1}$. Thus, the proton frequency ω in the applied magnetic field B_0 will be $\omega = 2.6751 * 10^8 B_0 \text{ rad sec}^{-1}$. Since NMR spectroscopists like to use f_0 (units is Hz) instead of ω (rad sec^{-1}) for the Larmor precession frequency, the above equation can be defined as:

$$f_0 = \gamma / 2\pi B_0 \quad (3)$$

Here, the proton Larmor frequency f_0 will be $f_0 = 42.575 B_0$ MHz, where units of B_0 is still Tesla. For example, when $B_0 = 7.03$ Tesla, the proton Larmor frequency f_0 will be 300.00 MHz. The direction of the bulk spin magnetization is anti-parallel to B_0 when γ is negative, such as electron. While it will be parallel to B_0 when γ is positive, such as ^1H , and ^{13}C .

Boltzmann distribution and the Spin temperature²⁹

After applying an external magnetic field B_0 , an energy difference between the two states of the nucleus (spin up α and spin down β) is created. It is noticed that there are more nuclei in the lower level (spin up α) than the upper level (spin down β), though the population differences are so small that there is generally only one more nuclei in the lower level in one million nucleus bulk samples.

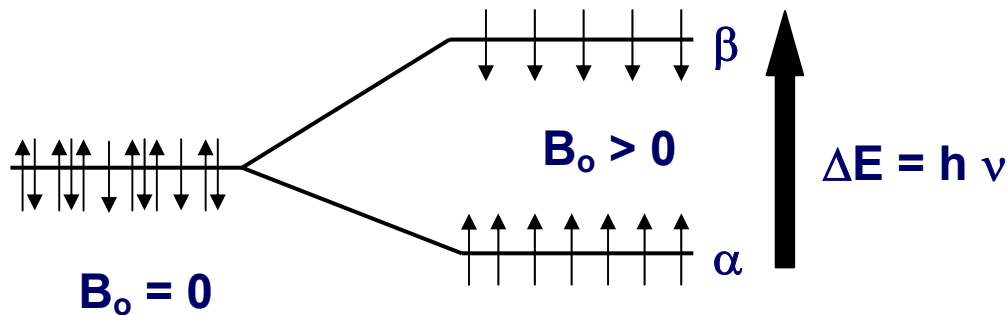


Figure 2. Without an external magnetic field B_0 ($B_0 = 0$), there are no energy differences between all the nuclear spins in a bulk sample. After applying an external magnetic field B_0 ($B_0 > 0$), the thermal effect generates the population difference between the spin up α and spin down β levels according to the Boltzmann distribution.

The population difference of the two spin levels at an absolute temperature T can be defined by the energy difference of the Boltzmann distribution.

$$N_{\beta} / N_{\alpha} = e^{-\Delta E / kT} = e^{h\gamma / kT} \quad (4)$$

Under general conditions the value of $h\gamma$ will be much smaller than the value of kT , so the Boltzmann distribution equation can be simplified to the following:

$$N_{\beta} / N_{\alpha} = 1 - h\gamma / kT \quad (5)$$

When applying the Boltzmann distribution to the nuclear magnetization system, it will be very useful to define a spin temperature term “ T_s ”, which can simulate the general temperature term in the regular thermal equilibrium system.

$$N_{\beta} / N_{\alpha} = e^{-\Delta E / kT_s} = e^{h\gamma / kT_s} \quad (6)$$

We can see that it is very convenient to use the spin temperature T_s to describe the phenomenon of an NMR experiment. When the experiment starts, the radio frequency irradiation will find a population difference between the upper and lower levels. There are more spins in the lower energy state (spin up α) than higher energy state (spin down β). The effect of the rf irradiation is that it makes more of the spin up (α) go up than the spin down (β) to go down. After several transitions take place, N_{α} will decrease and N_{β} will increase so that the ratio in equation 4 will increase and approach unity. Through the spin temperature term in equation 6, we can imagine that there is an increase of spin temperature T_s in the spin system: a “warming up” of the nuclear magnetization spin system. We should notice that after the ratio in equation 4 or 6 approaches unity, any further applied radiofrequency irradiation will no longer have any impact on the spin

system and produce no more net absorption. At that time, the spin system has reached saturation.

The effect of radiofrequency pulses

An electromagnetic wave, such as a radiofrequency (rf) pulse can excite nuclear magnetization. When the nuclei are excited, they will absorb energy and jump from lower levels to higher levels, and eventually they will relax back to lower levels and emit extra energies. The NMR detects the absorption of the electromagnetic radiation, and converts it to signal seen in an NMR spectrum. Only nuclei with spin number (I) $\neq 0$ can absorb/emit electromagnetic radiation. This radiofrequency wave generates an oscillating magnetic field B_1 , which interacts with the nuclei in addition to the static applied external nuclear magnetic field B_0 in the NMR experiment. The rf pulse is arranged in a position so that its nuclear magnetic field can oscillate along a direction perpendicular to z and B_0 field. The B_1 oscillating field can be divided into two frequency components which rotate about B_0 field in opposite directions. We defined the two frequencies as $\pm\omega_{rf}$. When introduced a rotating frame of reference which rotates at frequency ω_{rf} around the B_0 laboratory frame, the effect of this B_1 field will be most easily seen. In this rotating frame of reference, the B_1 field appears static, which means its time dependence is removed.

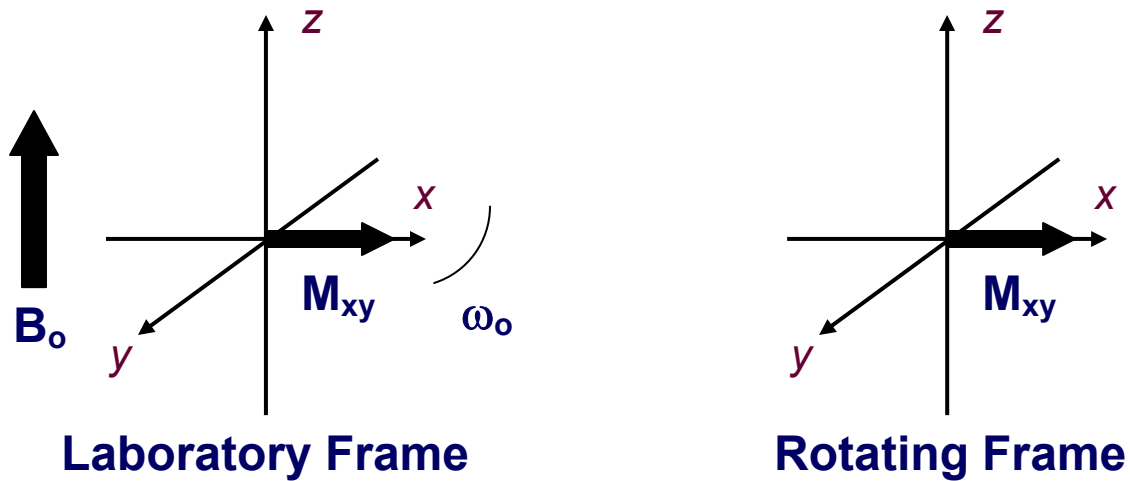


Figure 3. Laboratory frame and rotating frame in the nuclear magnetic field.

At rotating frame, the time dependence of the B_1 field will be removed and it will appear to be static.

On resonance, off resonance rf pulse and flip angle

Let's look at the effect of a rotating frame in the condition without the rf pulse.

When the nuclear spin vector is put in the B_0 field, a static, uniform nuclear magnetic field, the nuclear spin vector M will precess around B_0 at a frequency ω_0 in the laboratory frame. Now, if an on-resonance pulse is applied, meaning $\omega_0 = \omega_{rf}$, the nuclear spins will appear stationary in the rotating frame. The only effective field left in the rotating frame will be the B_1 field, while the B_0 field is removed in this frame. The nuclear spins will precess about the B_1 field at the following frequency:

$$\omega_1 = \gamma B_1 \quad (7)$$

Here, ω_1 is known as the nutation frequency. The pulse does not have to be applied on-resonance. Sometimes, the rf pulse is applied as an off-resonance pulse, which tilts the magnetic field B_1 to some place in the xz plane instead of the xy plane. Indeed, there will

be many cases in the solid-state NMR experiments when pulses are applied off-resonance. For example, in the later chapters, the frequency switched Lee-Goldburg cross polarization experiment has to apply the LG frequency pulse, which is an off-resonance pulse. In the rotation frame, the Larmor precession frequency is reduced from ω_0 to $\omega_0 - \omega_{rf}$ about B_0 , which means the effective field along the z axis in the rotation frame is $(\omega_0 - \omega_{rf}) / \gamma$, rather than zero. As a result, the total nuclear magnetic field in the rotating frame can be expressed with the following equation:

$$B_{eff} = \sqrt{B_0^2 (1 - \omega_{rf} / \omega_0)^2 + B_1^2} \quad (8)$$

The magnetization will precess around the resultant effective field B_{eff} as shown in Figure 4.

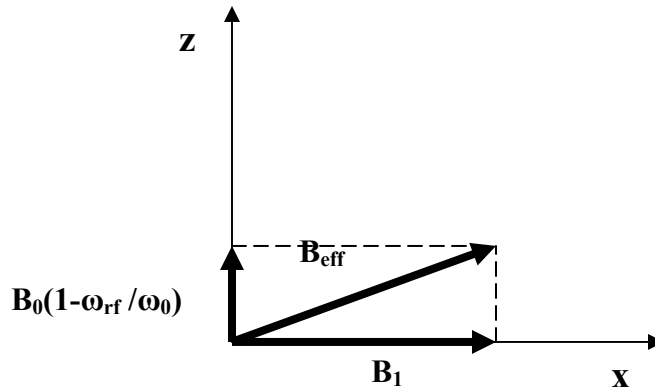


Figure 4. The rotating frame rotates about the z-axis at the frequency of the rf pulse, ω_{rf} .

The magnetic field B_1 due to the applied rf pulse appears static in the rotating frame. While the external static field B_0 is reduced to $B_0(1 - \omega_{rf} / \omega_0)$ in the rotating frame. The B_{eff} is the net effective field that the nuclear spin magnetization precesses around.

The flip angle, θ_{rf} , is the angle that the on-resonance pulse turns the nuclear magnetization during time τ_{rf} :

$$\theta_{rf} = \omega_1 \tau_{rf} = \gamma B_1 \tau_{rf} \quad (9)$$

Thus, a 90° pulse, or $\pi/2$ pulse is the rf pulse that flips the nuclear magnetic spin $\theta_{rf} = \pi/2$ or 90° from B_1 field. If B_1 field points in x' direction, the magnetization will flip from the z -axis to y' axis. A 180° or π pulse will flip the spins to the $-z$ axis.

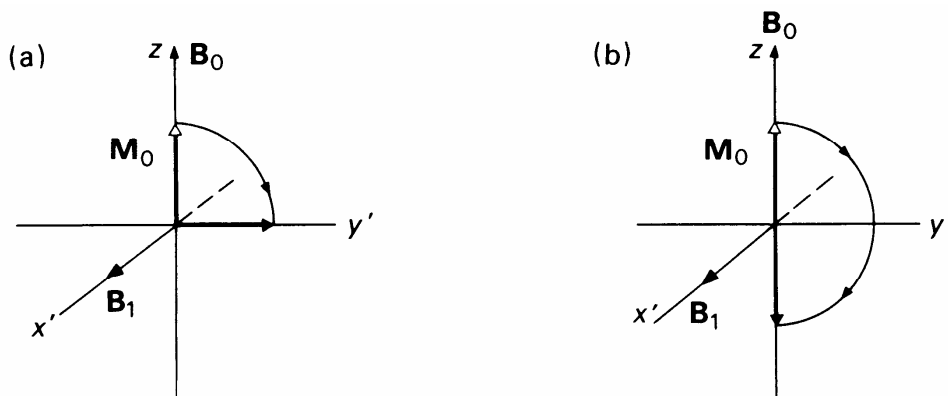


Figure 5. On-resonance 90° (a) and 180° (b) rf pulses that flip the nuclear magnetic spins to y' and $-z$ axis, respectively.

3.2. Essential techniques for solid-state NMR^{1,32}

Introduction

A solid-state NMR spectrum is much harder to acquire as opposed to a solution-state NMR spectrum. Mainly, in solution NMR, rapid polymer chain motion averages the chemical shift anisotropy and the dipolar interactions to almost zero. In solids, the polymer matrix restricts chain motion, and high-resolution spectra can be observed only after using rapid magic angle spinning to average the chemical shift anisotropy and high-power irradiation during signal acquisition to average the ^1H - ^{13}C dipolar interactions. In some cases more sophisticated NMR methods are used, usually consisting of applying a series of pulses in which the phases are alternated to remove a particular type of interaction. For example, in experiments where spin diffusion would complicate the results, such as the multiple pulse HetCor pulse sequence, it is possible to apply a series of pulses to the protons that quench spin diffusion. In other experiments, such as the 2D exchange pulse sequence, it is possible to obtain information about oriented polymers by synchronizing the pulses and signal acquisition to the sample rotation. In frequency and phase switched Lee-Goldburg HetCor experiments one uses the combination of complex off-resonance rf pulses and fast magic angle spinning to suppress the homonuclear and heteronuclear dipolar interactions.

The resolution in solid-state NMR is typically not as good as that for solutions. In favorable cases the linewidths can be as good as 50 Hz. This arises in part because the averaging of the chemical shift anisotropy and the ^1H - ^{13}C dipolar interactions by magic angle spinning and high-power decoupling is not as efficient as the averaging by chain motion in solution. In amorphous materials the linewidths have contributions from variations in the magnetic susceptibility and can be greater. The lines are sharper for

crystalline polymers as opposed to amorphous materials because they exist in a more uniform environment. The polymer matrix restricts chain motion so the γ -gauche effects are not averaged as in solution, thus the lines of amorphous polymers are inhomogeneously broadened by γ -gauche effects from a distribution of conformations.

In solid-state NMR, generally we will have to deal with anisotropic powder samples. The resultant solid-state NMR spectrum of a powder sample contains broader lines, in other words “powder patterns”. During the last 20 years, solid-state NMR spectroscopy gained a manifold achievement in both signal intensities and spectral resolution. The improvements were achieved via various pathways, such as macroscopic sample rotation (Magic-Angle-Spinning and Off-Magic-Angle-Spinning)^{33,34}, combining high-speed mechanical rotation of the sample with ingenious manipulations of the nuclear spins such as multiple-pulse irradiation, high-power decoupling and cross polarization³⁵, two-dimensional and higher-dimensional NMR techniques.^{36,37,38,26}

Magic angle spinning

Removal of chemical shift anisotropy and heteronuclear dipole-dipole interaction

Magic angle spinning (MAS) is used routinely in solid-state NMR experiments. The primary goal of MAS is to remove the effects of chemical shift anisotropy and to assist in the removal of heteronuclear dipolar interaction. At very high magic angle spinning speed, (above 10 kHz), MAS will also tend to remove the homonuclear dipolar interaction from solid-state NMR spectra, as we will see in the frequency-switched Lee-Goldberg experiment.

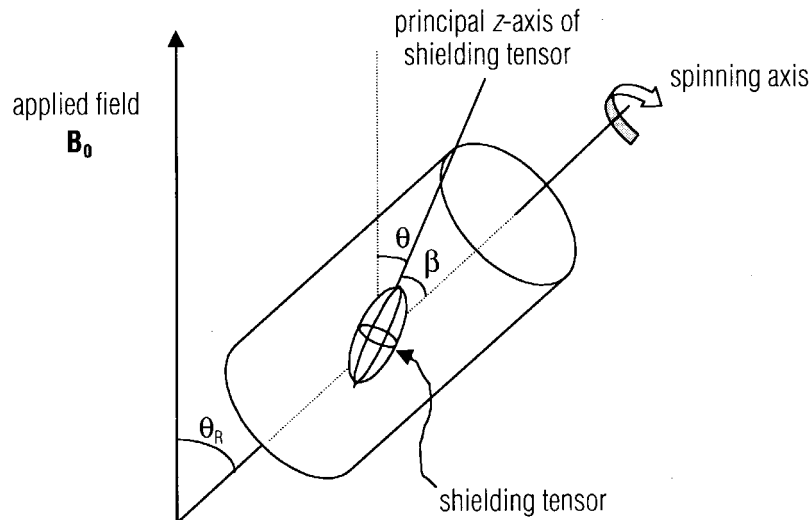


Figure 6. The magic angle spinning scheme in solid –state NMR experiment. (following reference 5)

The sample spins in a cylindrical rotor about a spinning axis oriented at the magic angle ($\theta_R = 54.7^\circ$) with respect to the applied magnetic field B_0 .

In solution NMR spectra, due to the rapid tumbling of the molecules, the effects of chemical shift anisotropy (CSA) and dipolar interaction almost disappear. The rate of change of molecular orientation is fast relative to the effect of CSA, and dipole-dipole interaction, thus averaging the $(3\cos^2\theta - 1)$ dependence of the transition frequencies. Here, the angle θ is the angle of the shielding tensor with respect to the applied field B_0 . In solid –state NMR, the motion is not that fast relative to the CSA and dipole-dipole interaction, hence we will use the magic angle spinning to achieve similar result to solution NMR. After we put the rotor containing the solid sample in the direction inclined

at the magic angle ($\theta_R = 54.7^\circ$) to the applied magnetic field B_0 , the average of $(3\cos^2\theta - 1)$ in these conditions can be shown with the following equation:

$$(3\cos^2\theta - 1) = \sqrt{(3\cos^2\theta_R - 1)(3\cos^2\beta - 1)} \quad (10)$$

Angle β and θ_R are defined in Figure 6. Since θ_R is set to be the magic angle 54.7° , then $(3\cos^2\theta_R - 1) = 0$, thus the average of $(3\cos^2\theta - 1)$ is zero too. In conclusion, providing the MAS spinning speed is fast enough, the effect of CSA and dipole-dipole interaction will approach to zero.

Fast MAS for removal of homonuclear dipole-dipole interaction

Magic angle spinning can be used for removing the effects of homonuclear dipole-dipole interaction if the MAS rate is high enough. When the MAS rate is very slow, meaning much less than the dipolar linewidth, MAS will have very little effect on removing all the effects including homonuclear and heteronuclear dipole-dipole interaction and CSA. The broad line will still exist as the line in the absence of spinning. At intermediate MAS rates, centered around quarter or a half of the dipolar linewidth, spinning sidebands will appear. The spinning sidebands associated with CSA and heteronuclear dipole-dipole interactions are all sharp lines, while those associated with homonuclear dipolar interactions are usually broadlines. When the MAS rate is high enough, usually much faster than the dipolar linewidth, all the three effects will be removed, making the lines narrow.

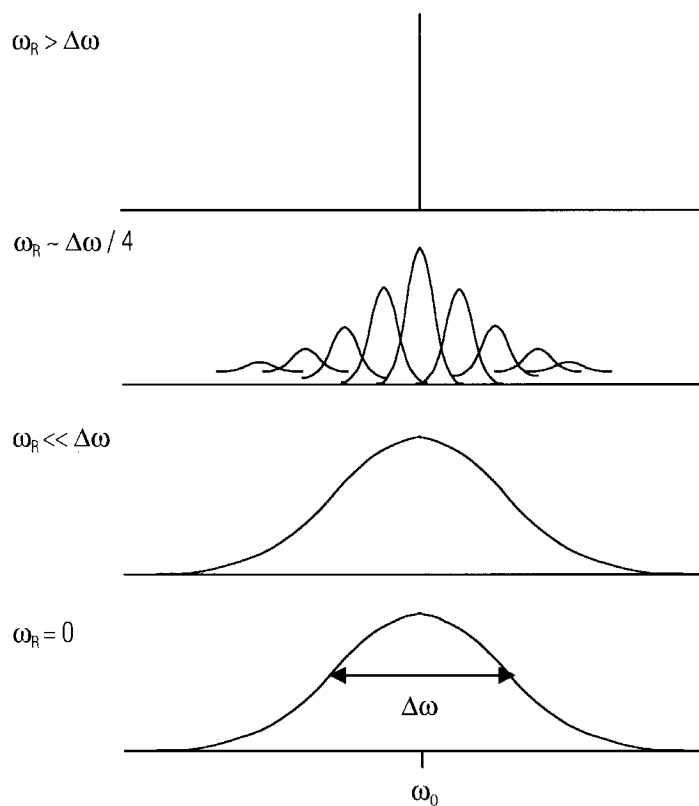


Figure 7. The effects of magic angle spinning on homonuclear dipole-dipole interaction. The broad line is narrowed by magic angle spinning rates of the order of the dipolar linewidth or higher. For slow MAS speed, broad spinning sidebands appear, and at very slow speed, there is no big effect of removing any of the effects.

High power proton dipolar decoupling

When observing a dilute spin, e.g. ^{13}C spins with ^1H or other abundant spins existing in the same nuclear magnetic spin system, broadening due to heteronuclear dipole-dipole interaction often causes additional problems to the already weak spectrum, since the ^{13}C only has about 1.1% abundance. High power decoupling is a simple technique which can be used to remove the heteronuclear dipole-dipole interaction, and achieve relatively good intensity and narrow peaks in the ^{13}C solid-state NMR spectrum.

In the case of dipolar-coupled ^1H and ^{13}C spin pairs, where ^{13}C spins' signals are needed to be observed, the application of high power decoupling will consist of applying a continuous irradiation of very high power (100-1000 watts) at the frequency of the proton resonance. In other words, following the ^{13}C pulse sequence, while the ^{13}C FID is being acquired, continuous high power ^1H irradiation decoupling is applied.

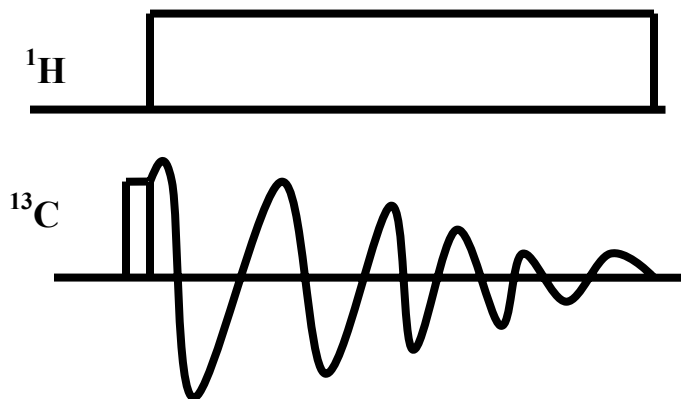


Figure 8. High power proton dipolar decoupling removes the effects of proton dipolar coupling from the ^{13}C solid-state NMR spectrum. High power irradiation is applied to the ^1H spins at the proton on-resonance frequency during the acquisition of the ^{13}C spin NMR spectrum.

Multiple pulse decoupling sequences

As described in Section 3.2, magic angle spinning can be used to remove the effects of homonuclear dipole-dipole interaction from the solid-state NMR spectrum, providing the rate of MAS is fast relative to the homonuclear dipolar linewidth. An alternative way to remove this interaction is to use a multiple pulse decoupling sequences.

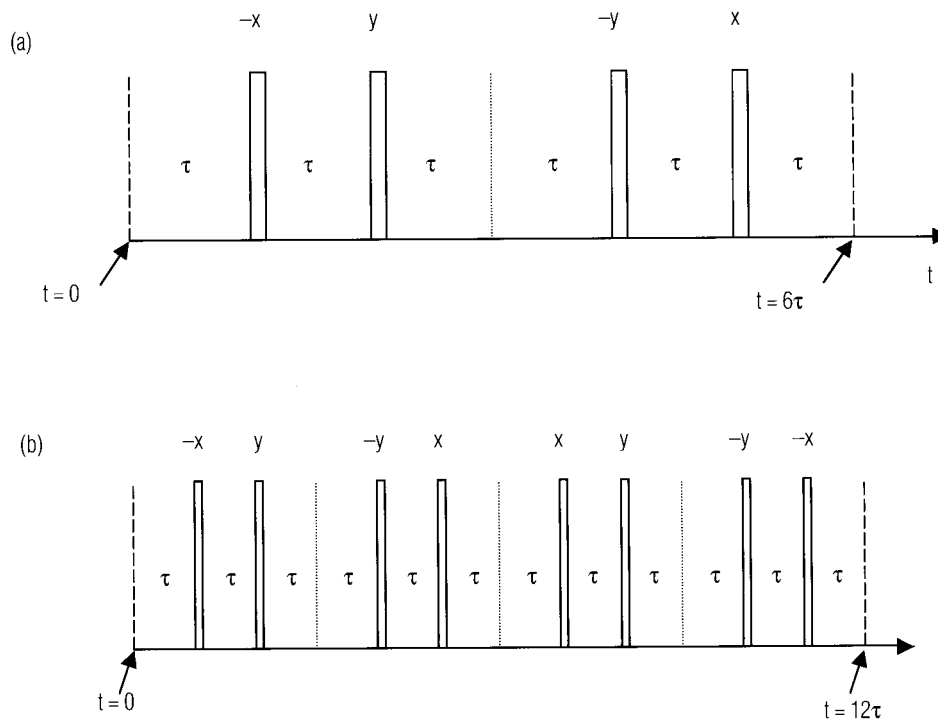


Figure 9. Multiple pulse sequences used for removing homonuclear dipolar coupling from solid-state NMR spectrum. In (a) WAHUHA (after Waugh, Huber, and HAberlen)³⁹ sequence and in (b) MREV-8 (after Mansfield, Rhim, Elleman, and Vaughan)^{40,41} sequences, all pulses are 90° pulses with the indicated phases, multiple times (as indicated by the arrows.) The MREV-8 sequence is actually a two phase-cycled WAHUHA sequence.

Many useful multiple pulse sequences exist in literature. The first, and also one of the simplest, is the WAHUHA sequence, shown in Figure 9 (a). The MREV-8 sequence is a modification of the simple WAHUHA sequence, is also widely applied. In a later section, we will use the BLEW-12^{42, 43} sequence to remove homonuclear dipolar coupling during the two dimensional heteronuclear correlation pulse sequence. The multiple pulse sequences are arranged in such a way that the effect of the dipolar Hamiltonian on the nuclear magnetization approaches zero.

Cross polarization and Hartmann-Hahn condition

Introduction

In numerous NMR experiments, there is a need to transfer energy between different sets of magnetic nuclei with different precession frequencies in order to enhance the signal. This can be achieved via cross polarization under the Hartmann-Hahn condition⁴⁴. Transfer of energy from one kind of nuclei to another is facilitated if the two different nuclei have the same resonance frequency. The most common example of the cross polarization energy transfer is between ¹H and ¹³C. Clearly, since the proton resonance frequency is a factor of four larger than that of ¹³C, the transfer of energy between them is forbidden. We can think of an experiment which places ¹³C nuclei in a high magnetic field and the ¹H nuclei in one-fourth as strong a field so as to achieve the same frequency. The condition here is the following:

$$\gamma_{13\text{C}}\mathbf{B}_0 = \gamma_{1\text{H}}\mathbf{B}_0' \quad (11)$$

Obviously, it is difficult to have two magnetic fields differing by a factor of four at the protons and ¹³C nuclei in the same molecules, but these difficulties are overcome under the Hartmann-Hahn condition. The first step in the Hartmann-Hahn process is to bring each set of nuclei to XY plane by a $\pi/2_x$ degree pulse. Next, each set of nuclei needs to be spin-locked to the Y axis by either a series of π_y pulses or equivalent continuous irradiation at the appropriate frequencies, then achieving the following state:

$$\gamma_{13\text{C}}\mathbf{B}_1 = \gamma_{1\text{H}}\mathbf{B}_1' \quad (12)$$

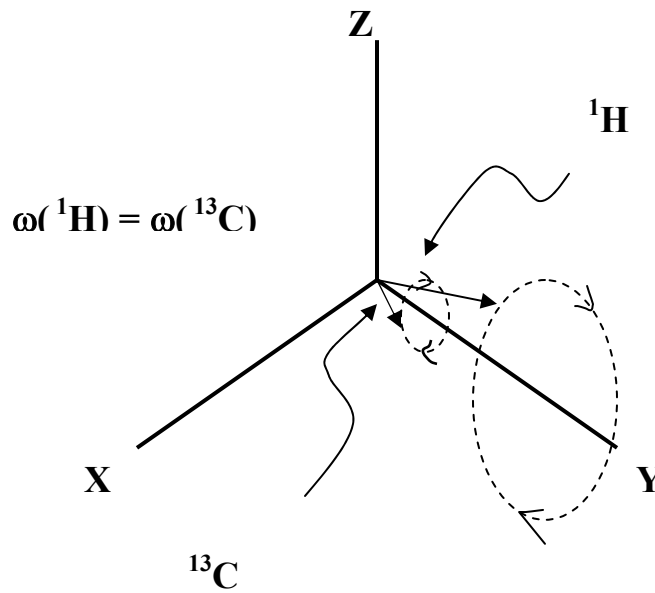


Figure 10. Cross polarization achieved by the Hartmann-Hahn condition, $\gamma_{13\text{C}}B_1 = \gamma_{1\text{H}}B_1'$

The Hartmann-Hahn condition is demonstrated in Figure 10. During these conditions, both sets of nuclei, within their respective rotating frames, precess with the same frequency about the Y-axis, thereby providing an opportunity for exchange of energy via coupled spin flip-flops.

CP pulse sequence

Figure 11 shows the cross polarization pulse sequence.

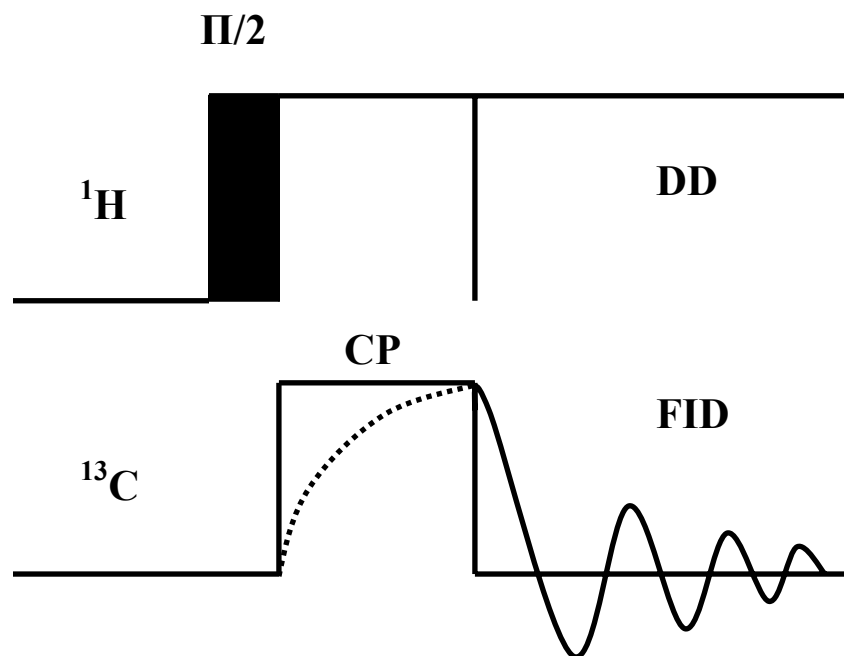


Figure 11. Cross Polarization Pulse Sequence.

After a $\pi/2$ excitation pulse on protons, transverse ^1H magnetization is locked while ^{13}C magnetization is created if the spin lock fields match the Hartmann-Hahn condition. Subsequently, the signal is observed under high power dipolar decoupling. The CP experiment is performed under magic angle spinning to attain the best signal. In combination with magic angle spinning, high resolution conditions are obtained for solid samples²², yielding isotropic signals with the characteristic chemical shift dispersion of ^{13}C and a typical linewidth of ~ 1 ppm. The CP/MAS experiment is the basis for many two- and multi-dimensional solid-state NMR experiments.

Experimental parameters

The MAS rotation frequency should be chosen high enough to average out the chemical shift anisotropy but not too high because sample heating due to rotor friction occurs. Typically, values between 3 and 6 kHz are reasonable for solid samples at high

magnetic field. The typical pulse length for the ^1H 90° excitation pulse should be on the order of 3-4 μs . The spin lock field on one channel should be set to approximately 50 kHz, while the corresponding spin lock field of the other channel is best determined experimentally for each sample. (the Hartmann-Hahn condition turns out to be dependent on the MAS frequency and shaped spin lock pulses may become necessary for efficient polarization transfer.)²³ Modern spectrometers allow for parameter optimization by sweeping through the power setting for the spin lock until maximum signal intensity is found. In organic solids, typical contact times to achieve maximal intensity are in the range of 0.5 to 1 ms. During acquisition, high power ^1H decoupling with a typical radio frequency (rf) field strength of 60-80 kHz should be applied. Best results are obtained with TPPM (two pulse phase modulation) scheme²⁴. Typical signal acquisition times are determined by the linewidth but should not exceed ~ 25 ms to avoid rf heating. A relaxation delay of 2-5 s between successive scans should be allowed for protons to fully relax and to prevent sample heating.

Figure 12 shows a CP/MAS spectrum for hexamethylbenzene running at MAS rate 4.5 kHz with 16 total scans.

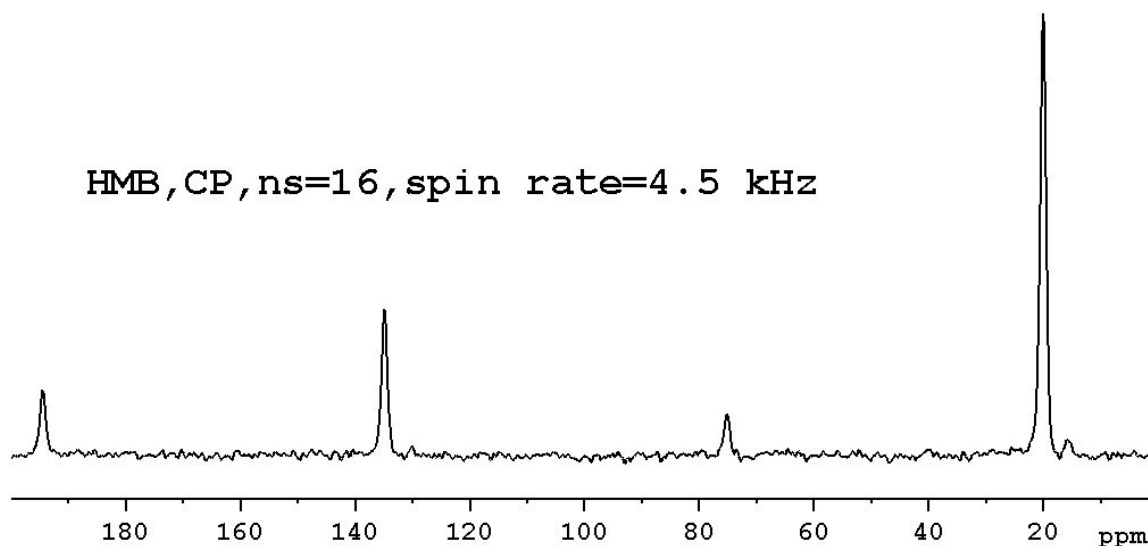


Figure 12. CP/MAS spectrum for hexamethyl benzene (HMB)

3.3. Special solid-state NMR sequences

3.3.1. T_1 , T_2 and $T_{1\rho}$

T_1 relaxation (also called longitudinal relaxation, spin lattice relaxation time⁴⁵) is a measure of the relaxation rate along the z axis. During this relaxation, the nuclear magnetization will lose its energy in the system to the surroundings (lattice) as heat. Examples of energy loss mechanisms include nuclear spins dipolar couple with other spins, or interaction with paramagnetic particles, etc. There are two ways to measure the T_1 relaxation time. The first is the inversion-recovery pulse sequence, which consists of $180^\circ - \tau - 90^\circ$ (observe)⁴⁶⁻⁴⁸. The 180°_x flip pulse inverts the M_0 (Magnetization) to the $-z$ axis, and then it decays exponentially back to M_0 as described by the following equation:

$$M_t = M_0 \{1 - 2 \exp[-(t/T_1)]\} \quad (13)$$

From the equation, we can see that when M is fully inverted, M will relax from $-M_0$ through zero to $+M_0$. And when we get the time (t_z) required for M to reach zero, we can calculate T_1 by the equation:

$$T_1 = t_z / \ln 2 = t_z / 0.693 \quad (14)$$

At this point, there is no X/Y magnetization, so there will be no way to see the signal in order to quantify T_1 . To solve this problem, we can apply a 90° pulse at particular intervals after the original 180° pulse. This way, the relaxed magnetization is flipped to the transverse plane (XY plane), and the receiver coil can detect the signals. A second way to measure the T_1 relaxation time is via the saturation-recovery pulse sequence. A limitation of using this method to measure T_1 is that spin-spin relaxation (T_2) in the xy plane must be much faster than the spin-lattice relaxation (T_1) in the z direction. The pulse sequence is $90^\circ - \tau - 90^\circ$ (observe). In this case, if the magnetization is placed in the xy plane by applying a 90° pulse, it will decay to zero before significant spin-lattice relaxation (T_1) occurs and then the magnetization will grow back to equilibrium in the z direction. Finally a 90° pulse is applied to acquire the signal. In order to make sure that the system is fully saturated, there is a preparation step which can be achieved using two common methods. Usually, one can apply a series of hard pulses with only short delays between them so that there is not enough time for the system to return to equilibrium and the whole spectrum becomes saturated. The hard pulses are always set up using 90° pulses. An alternative way is to use broadband ^1H decoupling, which will rapidly saturate the proton magnetization. The equation to calculate or map the spin-lattice relaxation time (T_1) in the saturate-recovery pulse sequence is the following:

$$M_t = M_0 \{1 - \exp[-(t/T_1)]\} \quad (15)$$

T_2 relaxation (also called transverse relaxation, spin-spin relaxation⁴⁵) is used to measure the rate of relaxation in the xy plane. T_2 relaxation does not involve energy exchange with the lattice, but it does exchange energy between spins, via a flip-flop type mechanism. The process causes a loss in phase coherence between spins. Instrumental

imperfections have a serious effect on T_2 measurements. The observed decay is always faster than $1/T_2$ because of the magnetic field inhomogeneity. Here each nuclear spin in the bulk sample experiences a slightly different local B_0 , thus each spin will precess at a slightly different frequency from the other nuclear spins. The result is a “fanning out” with a loss in phase coherence. We can use the Carr-Purcell-Meiboom-Gill (CPMG) pulse sequence to eliminate this inhomogeneous magnetic field contribution and get the real value of T_2 . The CPMG pulse sequence is the following: $90^\circ_{+x} - \tau - [180^\circ_y - 2\tau]_n - 180^\circ_y - \tau$ (Acq). The pulse sequence generates a spin echo pulse in the transverse plane (xy plane), and refocuses the magnetic field inhomogeneity effect by repeating $- [180^\circ_y - 2\tau]_n$ times. The value of T_2 can then be calculated by this equation

$$\mathbf{M}_y(t) = \mathbf{M}_y(0) \exp[-(t/T_2)] \quad (16)$$

$T_{1\rho}$ is known as the spin lattice relaxation time in the rotating frame⁴⁹⁻⁵¹. The pulse sequence is $90^\circ_x - B_{1y} - \tau - \text{observe}$. An on-resonance 90° pulse is first applied along x' to bring the magnetization along y' . The phase of this pulse is then shifted by 90° so that it is now applied along y' , followed by a 90° shift pulse or a “spin locking” pulse⁵²⁻⁶⁰. The magnetization is now spin locked by B_{1y} and it will undergo no precession in the rotating frame. However, the magnitude of the magnetization is far larger than can be maintained by B_1 , since it was developed in B_0 , which is several orders of magnitude greater than B_1 . Therefore, with time, the magnetization will decay with time to a value of $(B_1/B_0) M_0$, which is very small. This is very important for the $T_{1\rho}$ measurement because in the absence of this spin locking pulse, there would be simple decay of the y' magnetization due to T_2 relaxation processes. The spin-lattice relaxation in the rotating frame is characterized by the following equation,

$$M_y(t) = M_y(0) \exp[-(t/T_{1\rho})] \quad (17)$$

3.3.2. Spin diffusion and spin-diffusion solid-state NMR

The next focus will be on spin-diffusion in solid-state NMR experiments applied to amorphous polymers, blends and composites. This method is used to interrogate the local structure, dynamics, miscibility and the relationship between them. This method is very attractive since it does not require isotopic labeling,⁶¹⁻⁶³ a neutron source, or any special sample preparation treatments.

Bloembergen first introduced the term “spin diffusion” in 1947⁶⁴. Spin diffusion is actually a result of oscillating local transverse dipolar fields. Figure 13 shows the classical flip-flop of two magnetic dipoles. Many oscillating fields can lead to spin diffusion relaxation, also referred to as spin diffusion equilibrium.

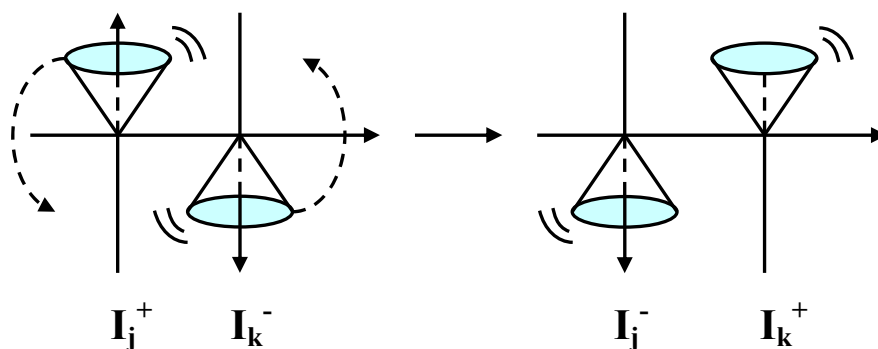


Figure 13. Classical flip-flop of two magnetic dipoles.

In the modern NMR theory and experiments, it is found that the term “spin diffusion” does not provide an appropriate description of the physical basis of the process. This

phenomenon is actually based on reversible coherent dipolar evolution⁶⁵ and does not represent a diffusion process in the classical sense. “Dipolar magnetization transfer” is a more correct description. The characteristics of the dipolar magnetization transfer depend somewhat on the spin species concerned, in particular on its abundance and on the strength of the dipolar coupling compared with other interactions. The most important spin diffusion processes in polymeric systems are among ¹H and ¹³C nuclei. Here we will focus on the ¹H spin diffusion process. Since the proton-proton dipolar coupling in typical organic polymers is by far the more dominating interaction, this allows for the ¹H spin diffusion process to be very efficient. The time dependence of the ¹H spin diffusion process contains information on the domain sizes in heterogeneous materials, for example, in structures with small domains, the magnetization equilibrates between domains faster than that in systems with large domains⁶⁷⁻⁷¹. The spin diffusion equilibrium occurs via the shortest paths, or in other words, spin diffusion can probe a “typical smallest diameter”. For example, ¹H spin diffusion can probe domain diameters from about 0.5nm to 200 nm. In the range below 5 nm, the “domain” may often be more correctly denoted as heterogeneities. However, spin diffusion is equally efficient for domains and heterogeneities.

Spin diffusion experiments are exchange experiments, consisting of an evolution or selection period, a mixing time (t_m), and a detection period. Figure 14 shows the schematic representation of the ¹H spin diffusion experiment.

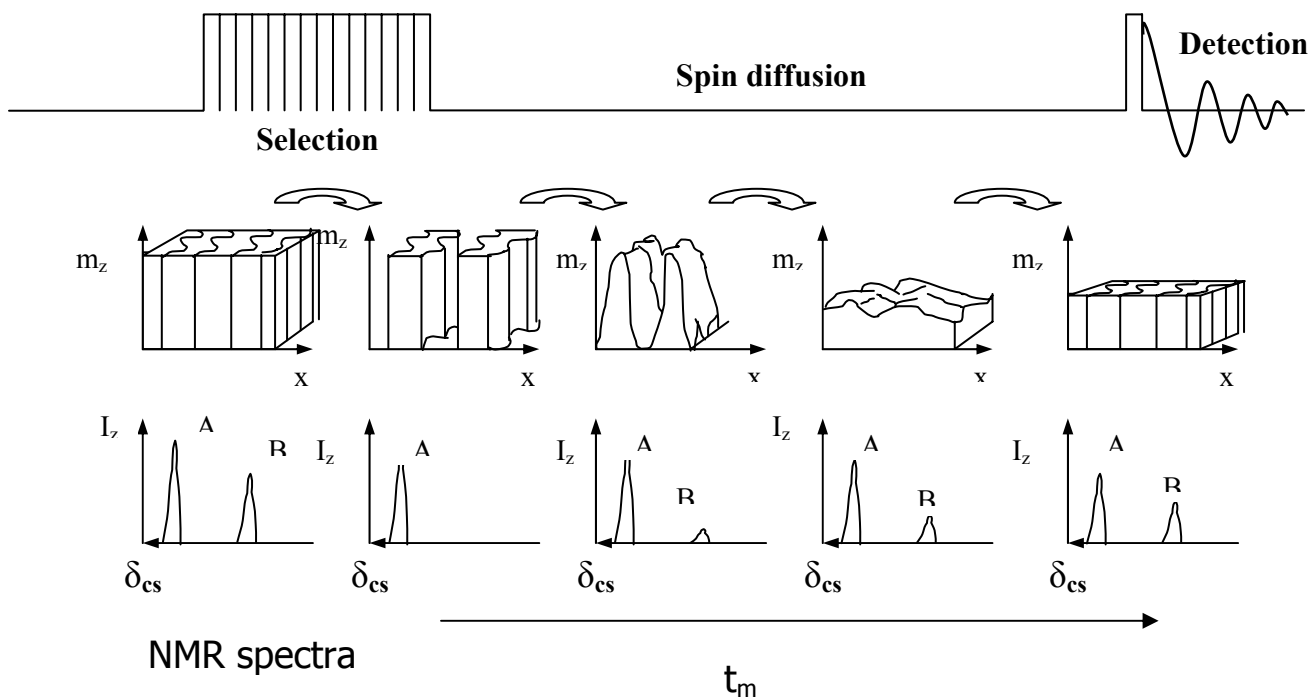


Figure 14. Schematic Representation of ^1H spin diffusion process. (following reference 26)

In order to let the spin diffusion occur, a spatially inhomogeneous distribution of z magnetization must be generated during the evolution period. In the most favorable case, the magnetization of one component is selected, while the magnetization of the rest of the components in the polymer is suppressed. During the exchange process (t_m), the magnetization of the selected component (denoted as the source region) diffuses out of the source region into its surrounding initially devoid of magnetization. Next, the distribution of all magnetization components in the sample is monitored in the NMR spectrum. For small domains, the magnetization equilibrium will occur fast, while in large structures, the magnetization from the source can only slowly penetrate into relatively thin boundary layers of the other domains. Consequently, the t_m dependence of the spin diffusion exchange is reflected in the spectrum intensities taken after the mixing time, thus providing direct information on domain sizes.

In order to experimentally describe the observed diffusive behavior of z magnetization transfer, here, we introduce the spin diffusion coefficient D , which can be determined as

$$D = \Omega * a^2 \quad (18)$$

The term Ω is the spin magnetization diffusion rate, corresponding to the rate of the dipolar coupling, and a is the spacing distance between the spins.

3.3.3. Goldman-Shen experiment – the simplest ^1H Spin Diffusion Experiment

The selection of ^1H magnetization in spin-diffusion experiments can be based on differences in the decay of the transverse proton magnetization, which is due to the differences in the dipolar coupling. This is the basis of the Goldman-Shen experiment⁶⁶. Figure 15 shows the principles of the Goldman-Shen experiment, which is the simplest

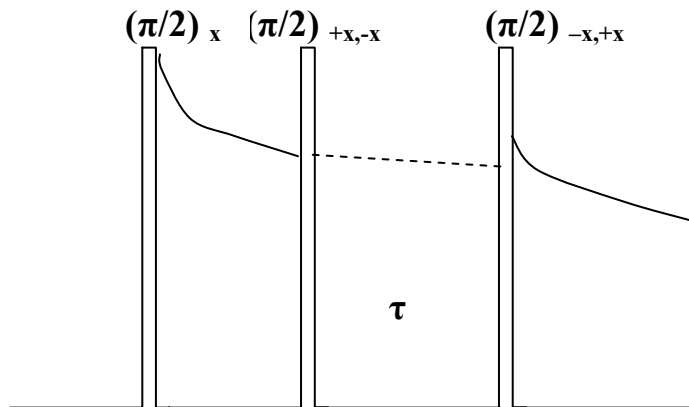


Figure 15. Goldman-Shen experiment sequence.

^1H spin diffusion experiment, and is applicable to systems consisting of both rigid and mobile regions. The first of the three $\pi/2$ pulses flips the ^1H magnetization to the XY plane. After a certain time (around $30\ \mu\text{s}$), the magnetization of the rigid components will diphas due to their strong dipolar coupling, thus only the ^1H magnetization from the mobile regions will remain. The second pulse flips this magnetization back to the z-axis after which a spin diffusion time is followed. During the mixing time, the mobile region diffuses its ^1H magnetization to the rigid regions and then the third pulse terminates the mixing time. The magnetization is detected to monitor the spin diffusion.

Chapter 2. New Method for Determination of Spin-Diffusion Coefficients

1. NMR method: 2D solid-state heteronuclear ^1H - ^{13}C Correlation experiment

Rigid, high T_g polymers, such as poly (bisphenol A carbonate) (PC) and poly (2, 6-dimethyl-1, 4-phenylene oxide) (PPO), have much longer correlation times of motions, and similar T_2 values, due to stronger homonuclear dipolar interactions. Due to these properties, methods such as the dipolar filter sequence or traditional Goldman-Shen sequence are not applicable for generating a ^1H polarization gradient within the monomer units of such rigid, high T_g , amorphous polymers.

The 2D solid-state HetCor (Heteronuclear correlation) experiment of Burum and Bielecki⁴³ is used to measure intramonomer spin diffusion behavior in rigid, amorphous polymers. The dominant interaction between ^1H and ^{13}C nuclei in most of these polymers is the direct heteronuclear dipolar coupling, and this interaction depends entirely on the distance between the nuclei, regardless of chemical bonding⁷²⁻⁷⁸. Therefore, the HetCor experiment provides a method for studying spin diffusion behavior, which depends entirely on the distance between the nuclei. Some advantages of the HetCor experiment are that no special manipulation of the proton spin reservoir (e.g., dipolar filter sequence) is required to generate an initial polarization gradient and all local ^1H magnetization is preserved prior to the spin diffusion period⁷⁹⁻⁸³. Therefore, all the spin magnetization

behavior is representative exactly of the bulk polymer. Another advantage is that the pulse sequence separates the proton resonance over a much larger ^{13}C chemical shift range, therefore, this technique can provide the well-resolved proton chemical shift information whereas it is impossible with any standard, 1D spectroscopic technique. As such, this technique may detect different polarization transfer processes occurring simultaneously over different length scales in blends or block polymers. The complete experiment is illustrated in Figure 16.

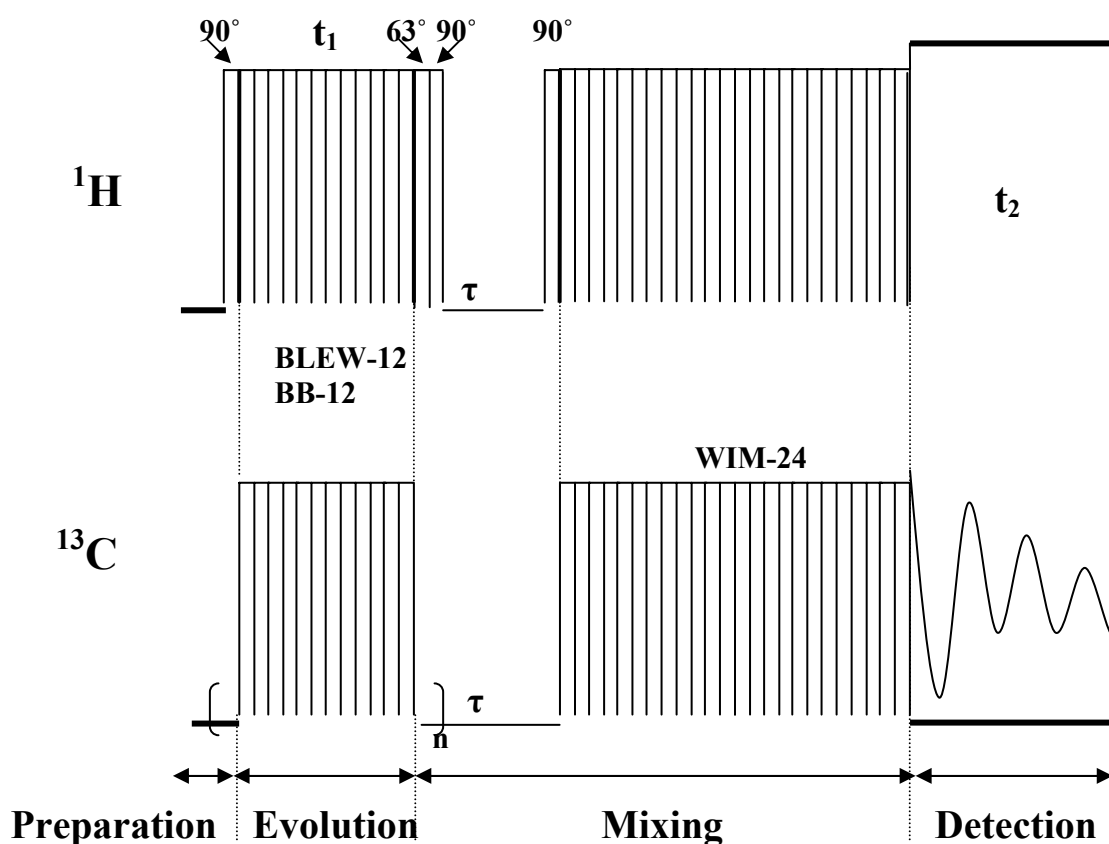


Figure 16. 2D Solid-State Heteronuclear Correlation pulse sequence (HetCor). Typical experimental parameters include 90° pulse widths $3.2 \mu\text{s}$ on each channel, spinning speeds $3.5\text{-}4.5 \text{ kHz}$, $256\text{-}512$ scans for each 64 points in t_1 dimension, typical experimental time $12\text{-}24$ hours.

The HetCor pulse sequence has four parts including preparation, evolution, mixing and detection, which are common to virtually all 2D NMR experiments. From Figure 16, it can be seen that at first the spin system is prepared by a single $\pi/2$ pulse, followed by the evolution time during which the protons are allowed to evolve in order to “label” them according to their chemical shift. After the evolution period, a spin diffusion time is inserted during which the ^1H spin magnetization diffuses to other ^1H nuclei in the polymer efficiently according to the distance between them. Then, a special cross polarization period is applied to transfer polarization selectively from the protons to the carbon spins via the heteronuclear dipolar interaction. Finally, the ^{13}C FID is acquired with proton decoupling. During the entire experiment, the sample is rotated at the magic angle in order to suppress broadening due to chemical shift anisotropy⁸⁶.

Phase cycling is added to the pulse sequence to suppress potential artifacts. In order to obtain a useful HetCor spectrum, it is necessary to effectively suppress both the ^1H - ^1H homonuclear dipolar interaction and the ^1H - ^{13}C heteronuclear dipolar interaction during the evolution period. The HetCor pulse sequence applies the BLEW-12⁴² sequences (a windowless multiple-pulse decoupling sequence) to proton spins, while simultaneously applying the BB-12 (a windowless multiple-pulse decoupling sequence by Burum and Bielecki) to ^{13}C spins. The BLEW-12 sequence suppresses homonuclear dipolar coupling, and BB-12 averages out the heteronuclear dipolar coupling, and also suppresses ^{13}C - ^{13}C homonuclear dipolar coupling. To maintain the ^1H magnetization purely from its own chemical shift, we also need to suppress the homonuclear dipolar coupling during the mixing period. The WIM-24 (Windowless isotropic mixing) was selected as the most effective method to obtain optimum polarization transfer through heteronuclear dipolar interaction, while simultaneously suppressing the homonuclear dipolar interaction during

the mixing period. Also, the cycling of the overall ^{13}C WIM-24^{84, 85} can eliminate any quadrature interactions, which might otherwise result from an improperly balanced receiver.

All the experiments were done on a Bruker DSX-300 instrument. The $\pi/2$ pulse widths were 3.2 μs on each channel. The experimental verification of proper HetCor performance was done using monoethyl fumarate (fumaric acid monoethyl ester). The carbon correlations to both olefinic and acidic protons were observed⁸⁷. The chemical shift-scaling factor in the ^1H dimension was measured experimentally to be 0.42, close to the theoretical 0.47 value. The proton frequency was shifted off-resonance by 5 kHz from the carrier to avoid any zero frequency artifacts and take advantage of second averaging effects. The spinning speed was set to approximately 3.5-4.5 kHz. The spinning speed value is a good compromise between the need to suppress the ^{13}C spinning sidebands and ensuring good polarization transfer performance. The spinning speed periods (285-333 μs) were larger than twice the WIM cycle length (total cross polarization time equals 76.8 μs), therefore preventing signal elimination or attenuation due to a refocusing of the ^{13}C - ^1H dipolar interaction at the end of each rotor period. 256-512 scans were taken for each of 64 points in the t_1 dimension, and recycle delays of 3-4 s were used. The total experiment time was typically 12- 24 hours. Quadrature detection was maintained in the t_1 dimension via TPPI (time-proportional phase incrementation). The data were processed with 50 Hz line broadening and zero filling to 1024 points in the t_1 dimension prior to Fourier transformation.

2. Polymers

The polymers investigated were poly (bisphenol A carbonate)(PC), and poly (2,6-dimethyl-1,4-phenylene oxide)(PPO). The molecular weight of PC and PPO were 100,000 g/mol and 60,000 g/mol, respectively. They are used without any further modification. Figure 17 shows the monomer structures of PC and PPO.

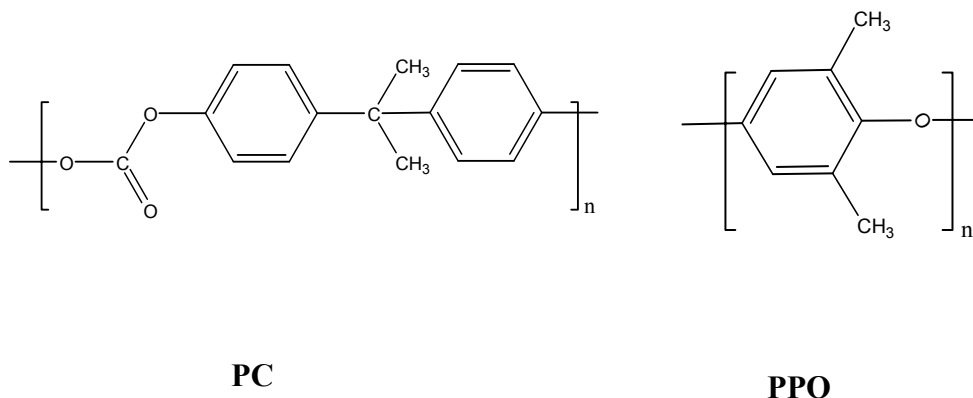


Figure 17. PC (poly (bisphenol A carbonate)) and PPO (poly (2,6-dimethyl-1,4-phenylene oxide)) simulated chain units.

3. Simulation of polymer chain units

Monomer size was determined via molecular chain dynamics calculations and dimensional measurements on chains with degree of polymerization = 100, using Insight II molecular modeling package (Polymer version 3.0.0) with PCFF force field parameters running on a Silicon Graphics IRIS Indigo workstation. Energy minimization was computed with 5000 iterations of an adjusted basis-steepest descents algorithm. Dynamics simulations were carried out at a constant temperature of 300K for 5 ps with time step of 1 fs. The characteristic dimension of the monomer x is defined as follows:

$$x = (l_c * d_c)^{1/2} \quad (19)$$

Here, l_c and d_c are the length and diameter, respectively, of the cylinder that inscribes the space-filling dimensions of the monomer. From this model, we extract $x_{\text{PPO}}=0.59$ nm and $x_{\text{PC}}=0.61$ nm. Figure 18 shows the simulated structures of PPO.

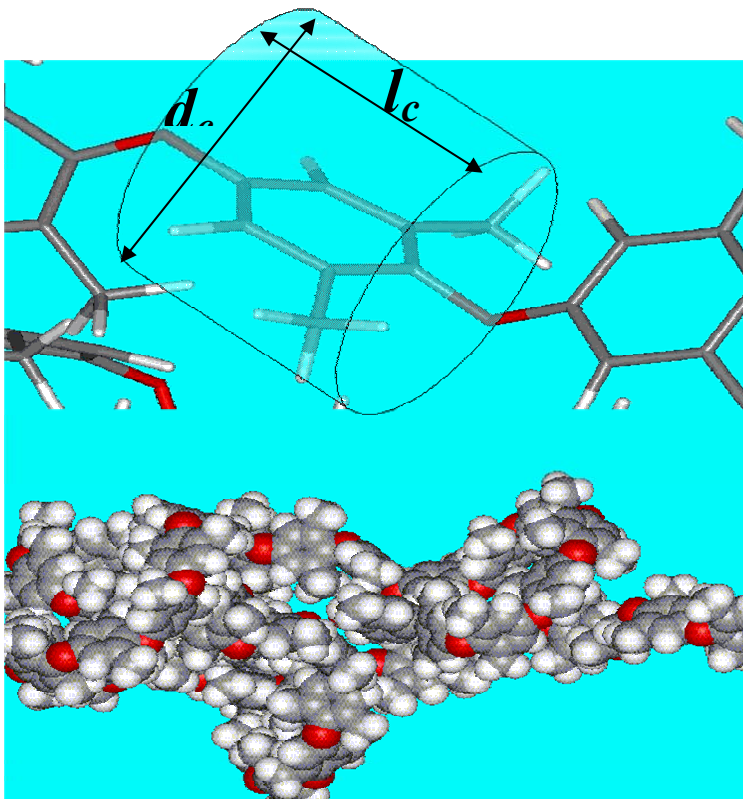


Figure 18. Simulated structure for a PPO chain demonstrating how the characteristic monomer dimension $x = (l_c d_c)^{1/2}$ was calculated.

4. Data analysis and Discussion

As stated in chapter 2.1, the 2D solid-state HetCor experiment is particularly useful for these rigid, high T_g , amorphous polymers.

Figure 19 shows selected 2D HetCor spectra for neat PC obtained with 0, 0.1, and 3 ms spin diffusion times. The horizontal axis (F2) corresponds to the ^{13}C chemical shift

range (0 to +160 ppm), and the vertical axis (F1) corresponds to the proton chemical shift range (-5 to +15 ppm). Contour spots in the spectra result from individual ^{13}C - ^1H pairs, correlated by the through-space ^{13}C - ^1H dipolar interactions. The chemical shift of the ^1H and ^{13}C for each pair can be obtained from the F1 and F2 axes, respectively. Horizontal (^{13}C) and vertical (^1H) projections of the two-dimensional spectra are shown above and to the left. At $\tau = 0$ (Figure 19A), we can observe that there are no aromatic cross-peaks for the CH_3 peak (at 31 ppm) and for the quaternary isopropylidene carbon at 42 ppm, and there are no aliphatic cross-peaks for any of the three aromatic carbons (120- 150 ppm region).

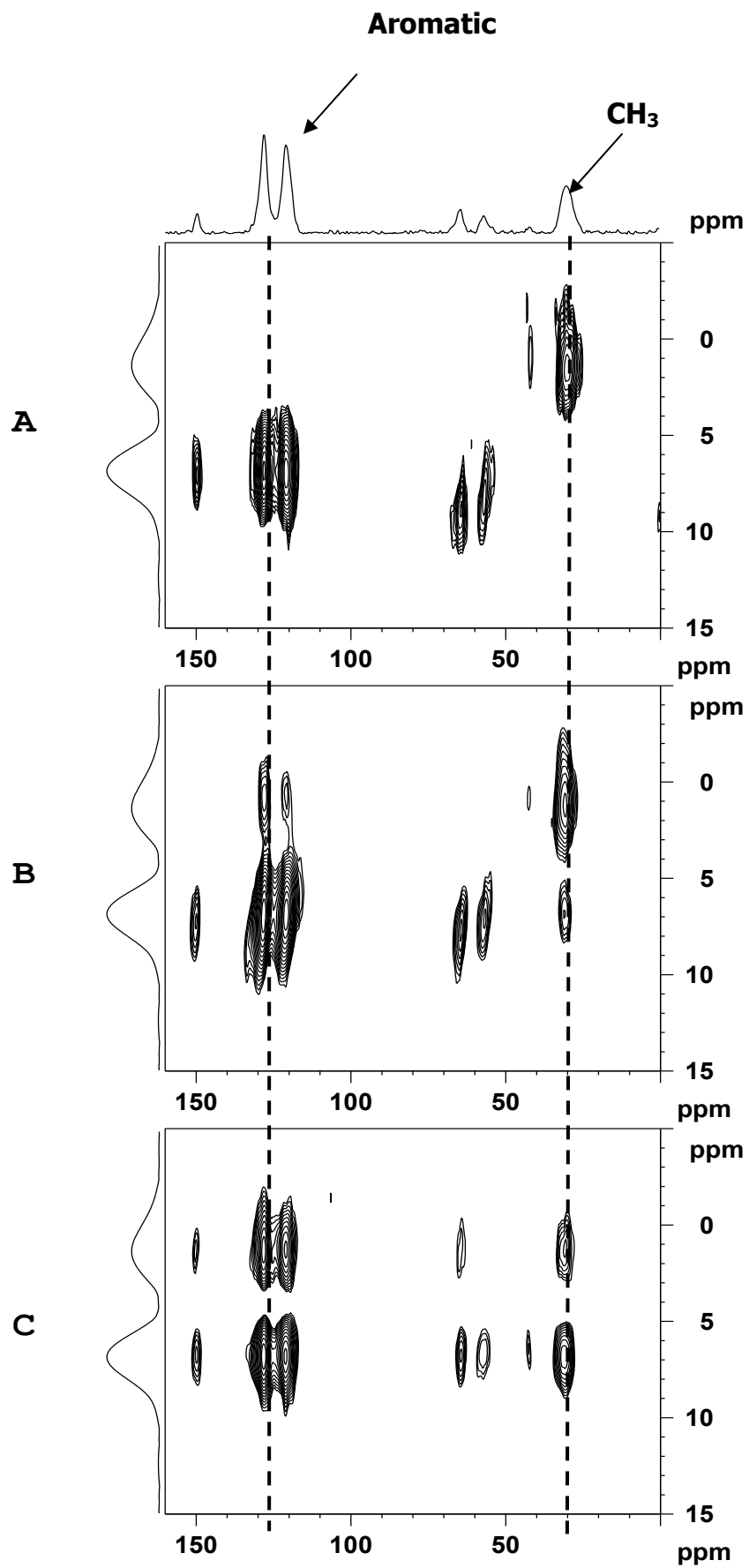


Figure 19. 2D HetCor spectra obtained for PC with spin-diffusion times of (A) 0, (B) 0.1, (C) 3 ms. Note in particular the time-dependent cross-peak intensities for the CH₃ and aromatic CH groups.

From these observations, we find that without the spin diffusion time, the protonated sites (bond length ~ 0.108 nm) are nearly fully polarized and show strong intensities, while the nonprotonated sites with nearest neighbor protons (0.2- 0.3 nm) show smaller intensities, and protons at distances greater than about 0.3 nm are not detected. When inserting a spin diffusion time before the cross polarization period, the ^1H - ^1H dipolar interactions will have time to take effect. Thus, we can observe that the cross-peaks at ^{13}C aliphatic chemical shifts corresponding to the aromatic ^1H chemical shifts, e.g., the CH₃ peak at 31 ppm, increase with the mixing time. Simultaneously, the cross-peaks at ^{13}C aliphatic chemical shifts, which correspond to the aliphatic ^1H chemical shifts, decrease with the spin diffusion time. Conversely, the ^1H aliphatic cross-peaks grow at aromatic ^{13}C chemical shift positions (120-130 ppm), while ^1H aromatic cross-peaks decay at the aromatic ^{13}C chemical shift positions. We can take ^{13}C slices (cross-section) at the aromatic and aliphatic ^1H chemical shifts, and also ^1H slices (cross-section) at the aromatic and aliphatic ^{13}C chemical shifts. Through these cross-sections we can observe how the ^1H spin magnetization polarizes through the ^1H - ^1H dipolar interactions. Figure 20 shows the cross-sections for either slice types for PC methyl and aromatic ^{13}C - ^1H pairs at conditions of no mixing versus equilibrium spin diffusion.

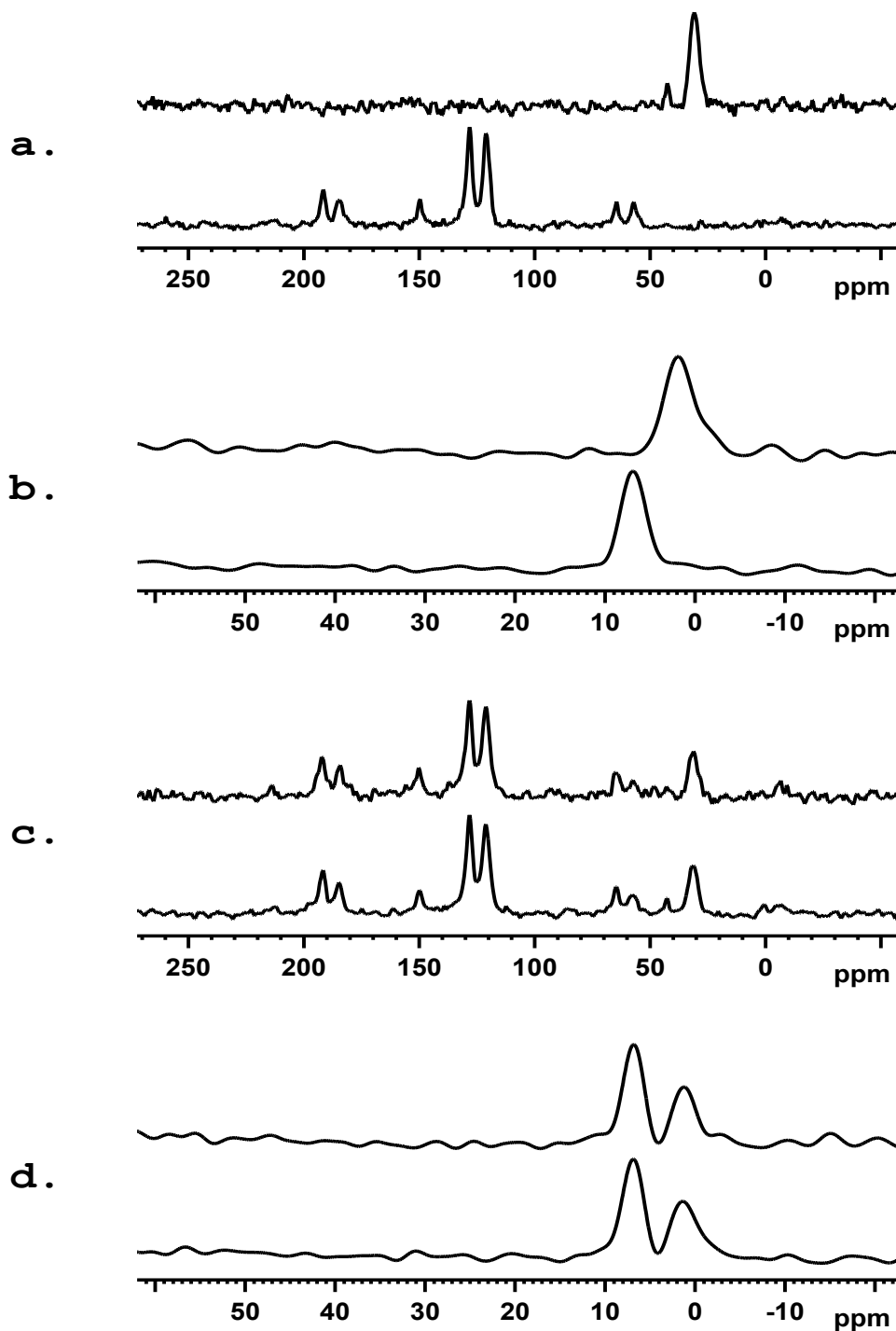


Figure 20. (a) The ^{13}C slices at the methyl ^1H peak (top) and the aromatic ^1H peak (bottom) for $\tau_m = 0$. (b) The ^1H slices at the 31 ppm methyl ^{13}C peak (top) and the 128 ppm aromatic ^{13}C peak (bottom) for $\tau_m = 0$. (c) The ^{13}C slices at the methyl ^1H peak (top) and the aromatic ^1H peak (bottom) for $\tau_m = 1$ ms. (d) The ^1H slices at the 31 ppm methyl ^{13}C peak (top) and the 128 ppm aromatic ^{13}C peak (bottom) for $\tau_m = 1$ ms.

In Figure 20a-d, the top slice shown comes from a methyl position, either ^1H or ^{13}C , and Figure 20a,b compares slice types for no spin diffusion, while Figure 20c,d compares those chemical shifts after equilibrium has been reached. We should notice that the slices taken at the CH_3 positions (the top slice) always have reduced signal-to-noise ratio relative to their aromatic counterparts (lower slice in each set). This is due to the reduced isotropic ^1H - ^{13}C polarization transfer efficiency for a rapidly rotating methyl group relative to the more rigid aromatic ^{13}C - ^1H pairs. Since there are fewer peaks and no sidebands for the ^1H slices, these ^1H slices can be used to extract spin-diffusion curves. Quantitative analysis of the ^1H aromatic and methyl slices for each of the mixing times in the PC experiment results in the spin-diffusion curves shown in Figure 21. The spin diffusion curves are constructed by plotting the ratios of the cross-peak intensity of aromatic protons to the summation of cross-peak intensities of aromatic and aliphatic protons at any ^{13}C chemical shifts in each spin-diffusion mixing time.

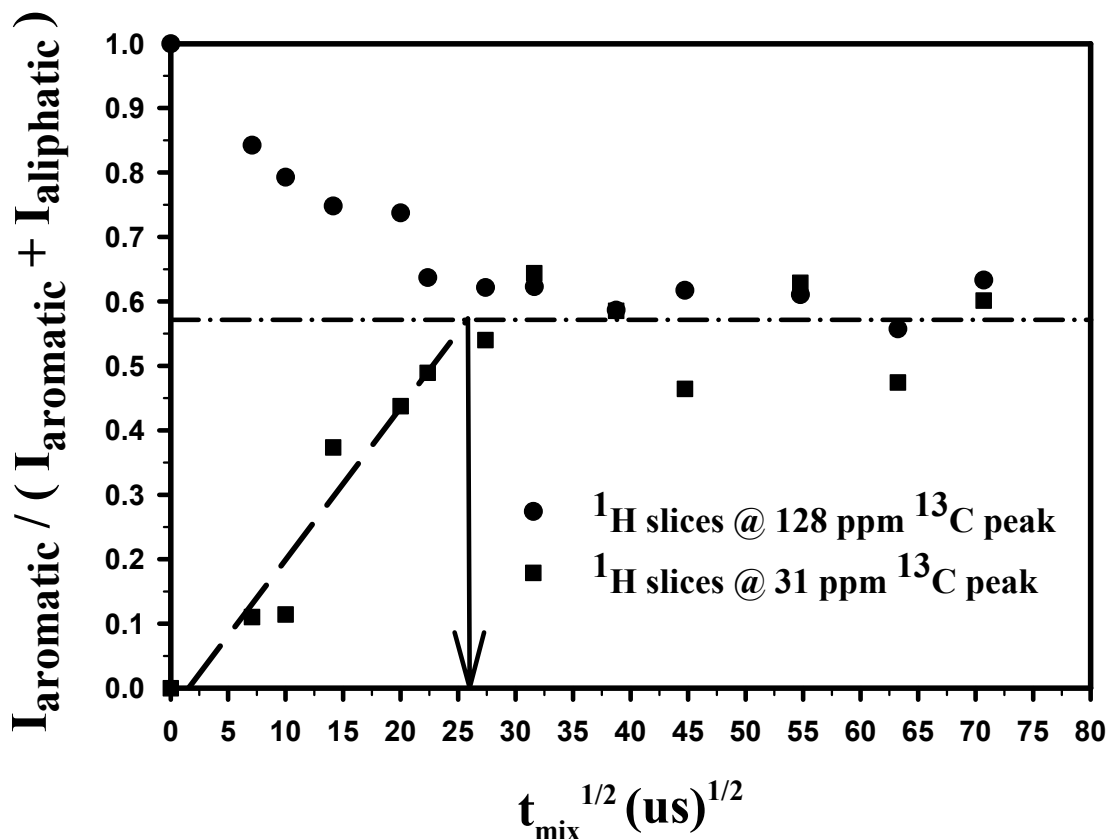


Figure 21. Spin-diffusion curves for PC constructed from deconvolution of the ^1H slices at the methyl (31 ppm) and aromatic (128 ppm) ^{13}C shifts in terms of the integrated intensity ratio of ($I_{\text{aromatic}} / (I_{\text{aromatic}} + I_{\text{aliphatic}})$).

Here, we pick CH_3 ^1H slices at 31 ppm aliphatic ^{13}C peaks and ^1H slices at 128 ppm aromatic ^{13}C peaks to calculate the previously stated ratio. On the basis of a least-squares analysis of the first six data points for the rising curve obtained from the CH_3 slices (since the spin diffusion reaches equilibrium at the sixth mixing time data point), we can get a line. The intersection of that line with the line denoting the equilibrium slice polarization ratio, defines the equilibrium mixing time $(\tau_{\text{m,eq}})^{1/2} = 26 \mu\text{s}^{1/2}$. The equilibrium ratio is defined by the PC structure, which contains eight aromatic and six aliphatic protons. Hence, when spin diffusion reaches equilibrium, the ^1H spin magnetization will distribute

according to the numbers of the protons in the chain. The theoretical ($I_{\text{aromatic}} / (I_{\text{aromatic}} + I_{\text{aliphatic}})$) ratio of 0.57 agrees very well with what is observed experimentally from the Figure 21.

2D HetCor contour plots are shown in Figure 22 for PPO at 0, 50 μs , and 3 ms spin diffusion times.

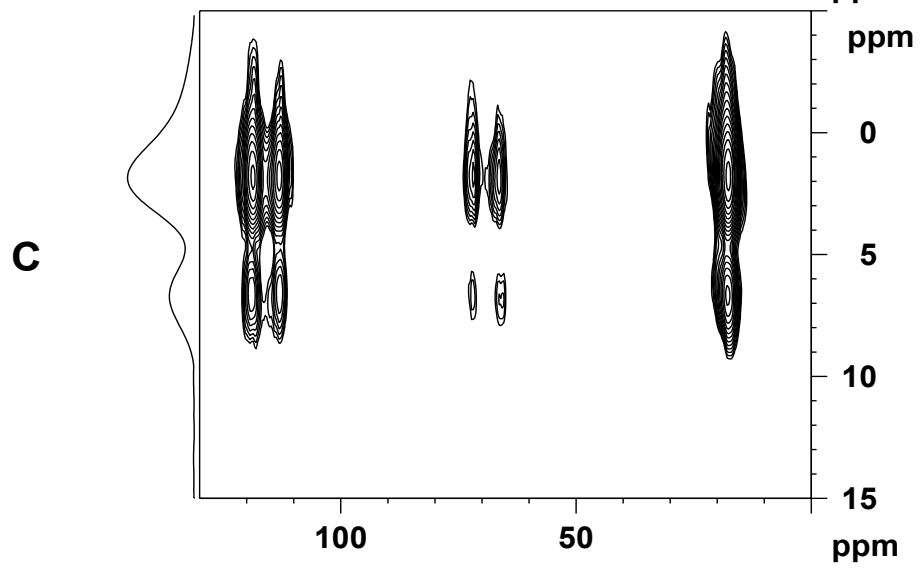
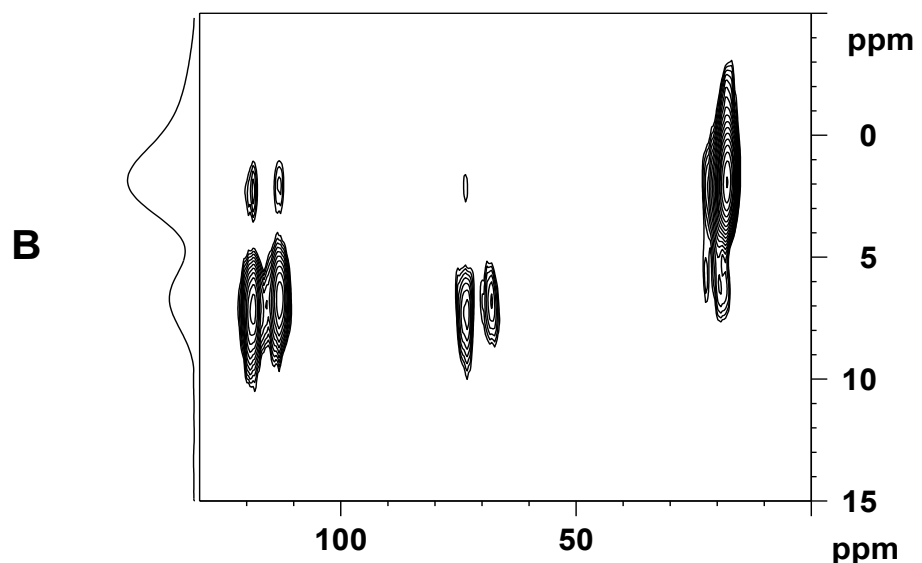
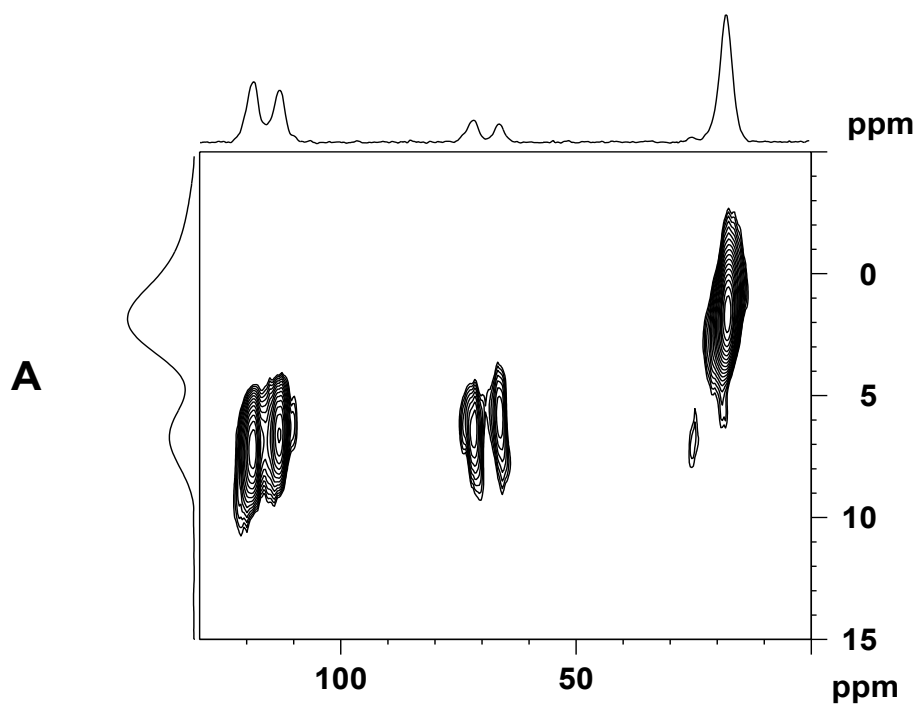


Figure 22. 2D HetCor spectra obtained for PPO with spin-diffusion times of (A) 0 ms, (B) 0.05 ms, (C) 3 ms.

In order to eliminate any potential contributions from sidebands, quantitative analysis of the spin diffusion curves for PPO was measured from $(I_{\text{aliphatic}} / (I_{\text{aliphatic}} + I_{\text{aromatic}}))$ ratios of ^1H slices through 120 ppm aromatic ^{13}C peak instead of using the ratios of $(I_{\text{aromatic}} / (I_{\text{aromatic}} + I_{\text{aliphatic}}))$ for PC. Considering the spinning speed used in this PPO HetCor experiment, a small aromatic sideband would contribute to ^1H aromatic intensity at CH_3 carbon slice positions, and therefore, we would use the above stated ratio to avoid this sideband contribution. The complete PPO spin-diffusion curves are shown in Figure 23. Similarly, on the basis of least-squares analysis of the first six data points, and the intersection with the spin diffusion equilibrium line $((I_{\text{aliphatic}} / (I_{\text{aromatic}} + I_{\text{aliphatic}})) = 0.75)$, (defined by the monomer size of PPO), we show that the $(\tau_{\text{m,eq}})^{1/2} = 23 \mu\text{s}^{1/2}$.

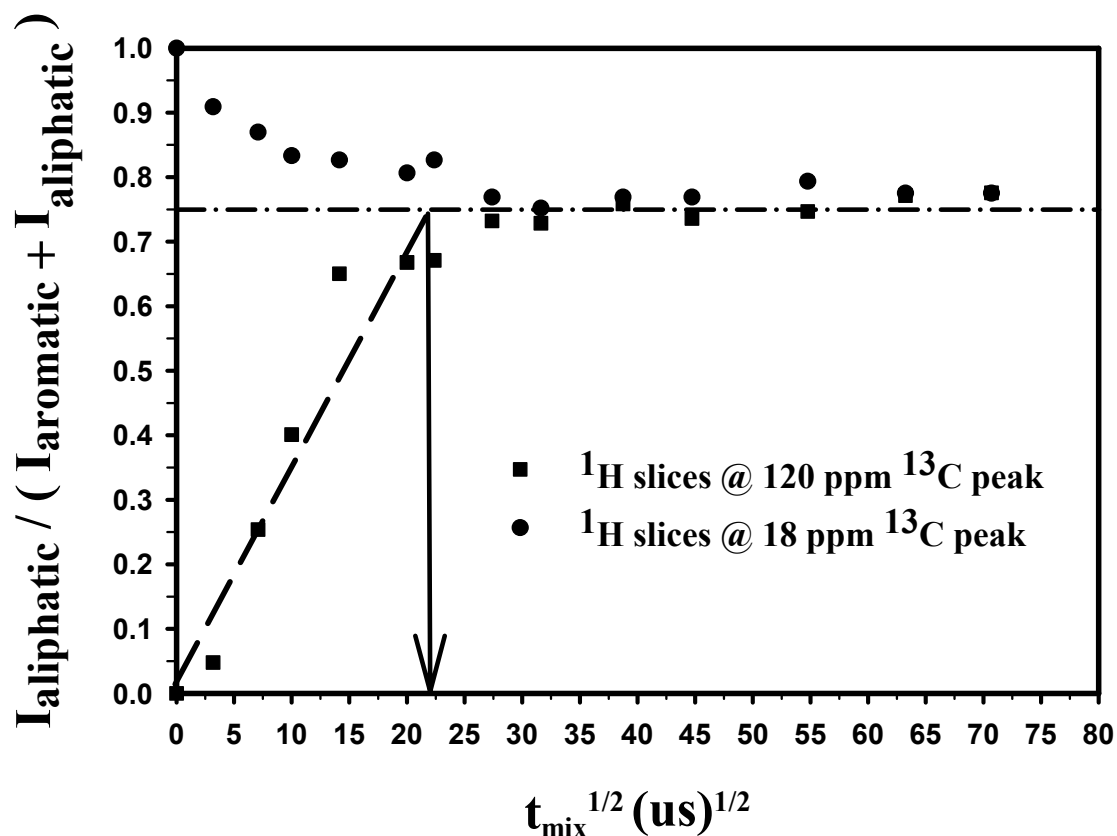


Figure 23. Complete spin-diffusion curves for the 2D HetCor experiments for PPO. Here the growth of the aliphatic ^1H correlation at the 120 ppm aromatic ^{13}C chemical shift is plotted as a function of the square root of the spin-diffusion mixing time.

Notice that the PPO polymer equilibrates a little bit faster than the PC, since it is less rigid. But basically, the values of the $(\tau_{\text{m,eq}})^{1/2}$ are fairly similar for both PC and PPO. The reason comes from the nearly identical “effective” monomer size of each polymer. The “effective” monomer size is defined as the basic ^1H -bearing repeat unit, thus though PC is a chemically larger monomer unit, it only requires one-half of its monomer structure to define the ^1H polarization stoichiometry and is therefore very similar to PPO.

Figure 19 shows the chain structure, and schematic for defining “effective” monomer size from the simulated PC chain. The scheme for PPO is shown in Figure 18. From these models, we get $x_{PC} = 0.61$ nm and $x_{PPO} = 0.59$ nm. Right now, we can calculate the spin-diffusion coefficients (D) from the following equation:

$$D = (\pi x^2) / (4\tau) \quad (20)$$

Here, x is the “effective” monomer size (from the simulations) and τ is the spin-diffusion equilibrium time (from the determination of $(\tau_{m,eq})^{1/2}$ with the HetCor experiments). This equation is identical to the equation reported by Spiess,^{61, 26, 88} except that we have not included the scaling factors which model the morphology or dimensionality of two-phase systems with finite domain sizes.

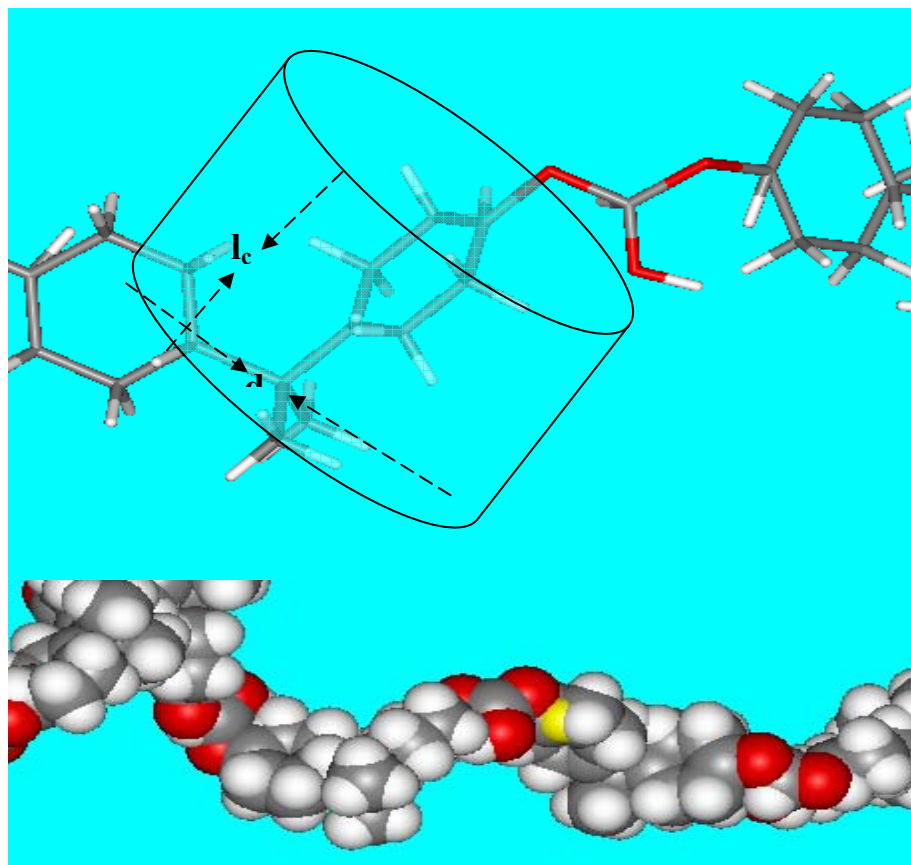


Figure 24. Simulated structure for the PC, where the cylinder inscribes the “effective” monomer size.

Since the proton polarization will diffuse through the shortest internuclear distances and there is no finite interface for the pure polymers, the intramonomer polarization spin diffusion will dominate polarization transfer. Thus, for PC and PPO, the calculated values of D are $4.2 * 10^{-12}$ and $5.2 * 10^{-12}$ cm^2/s , respectively. These results are in complete agreement with the published values of spin-diffusion coefficients for rigid, amorphous polymers, which are reported as ranging from $1 * 10^{-12}$ to $9 * 10^{-12}$ cm^2/s with exact values dependent upon the polymer dynamics^{61,62,26,89-90}. We should note that while the PC and PPO polymer exhibit reduced dipolar couplings relative to other glassy polymers due to their high methyl group content, the reason we used them as initial model system is that they only have two proton spin populations (aromatic and methyl). However, this is not a limitation to this method, since the HetCor experiment can resolve all the ^1H - ^{13}C spin pair contours, no matter how chemically different they are, and whether or not they reach polarization equilibrium.

5. Heterogeneous systems

The 2D solid-state spin-diffusion/heteronuclear correlation experimental strategy can be used to measure changes in spin-diffusion coefficient for a polymer, once it is blended with another polymer. It is known that individual polymer chain dynamics can change upon blending with other polymers, and as a result, it will alter the value of the spin-diffusion coefficient. Unlike other methods based on ^1H relaxation or line width

calibrations, the HetCor experiment can resolve intramolecular and interchain spin-diffusion polarization, and thus avoid the error from the interchain spin-diffusion polarization when calculating the D after blending.

The domain size χ_{dis} from polarization transfer phenomenon, or the spatial propagation of ^1H magnetization is typically described for a binary polymer blend according to Equation 21:⁶¹

$$x_{dis} = \left(\frac{\rho_1\varphi_1 + \rho_2\varphi_2}{\varphi_1\varphi_2} \right) \left(\frac{4\varepsilon\varphi_{dis}\sqrt{D_1D_2}}{\sqrt{\pi}(\rho_1\sqrt{D_1} + \rho_2\sqrt{D_2})} \sqrt{\tau_m} \right) \quad (21)$$

Here, ρ represents the proton density of each component, φ represents the volume fraction, D_i represents the spin-diffusion coefficient for homopolymer component i , τ_m represents the equilibration time, and ε represents the number of orthogonal directions for polarization transfer to occur. Since it is well-known that the polymer chain dynamics can change upon blending, using D values obtained from neat polymers in equation 21 may lead to erroneous length scales of mixing. But length scale of mixing depends only on the square root of D , and therefore errors in D do not translate into large errors in x . The ability to independently measure an upper limit for D on the sample of interest is often more important than the precise value of its D . Placing an upper limit on D via the HetCor experiment results in a maximum distance for domain sizes, or heterosegmental contacts, in the blends. So the revised D values determined from observing intramolecular spin-diffusion for each polymer in the blend provide accurate dimensional quantification and referencing of intermolecular mixing. We have found this is true for

several blends and copolymers that have large differences in T_g , e.g., polyisobutylene-polystyrene copolymers⁹¹, polystyrene/poly (vinyl methyl ether), and polycarbonate/polycaprolactone blends.

The advantages of using intramolecular polarization as a reference point for heterogeneous systems are also apparent in blends or copolymers from polymers with similar T_g 's. Figure 25 shows selected results from a symmetric PS-b-PMMA diblock copolymer, with each block having a molecular weight of ca. 55 000 g/mol.

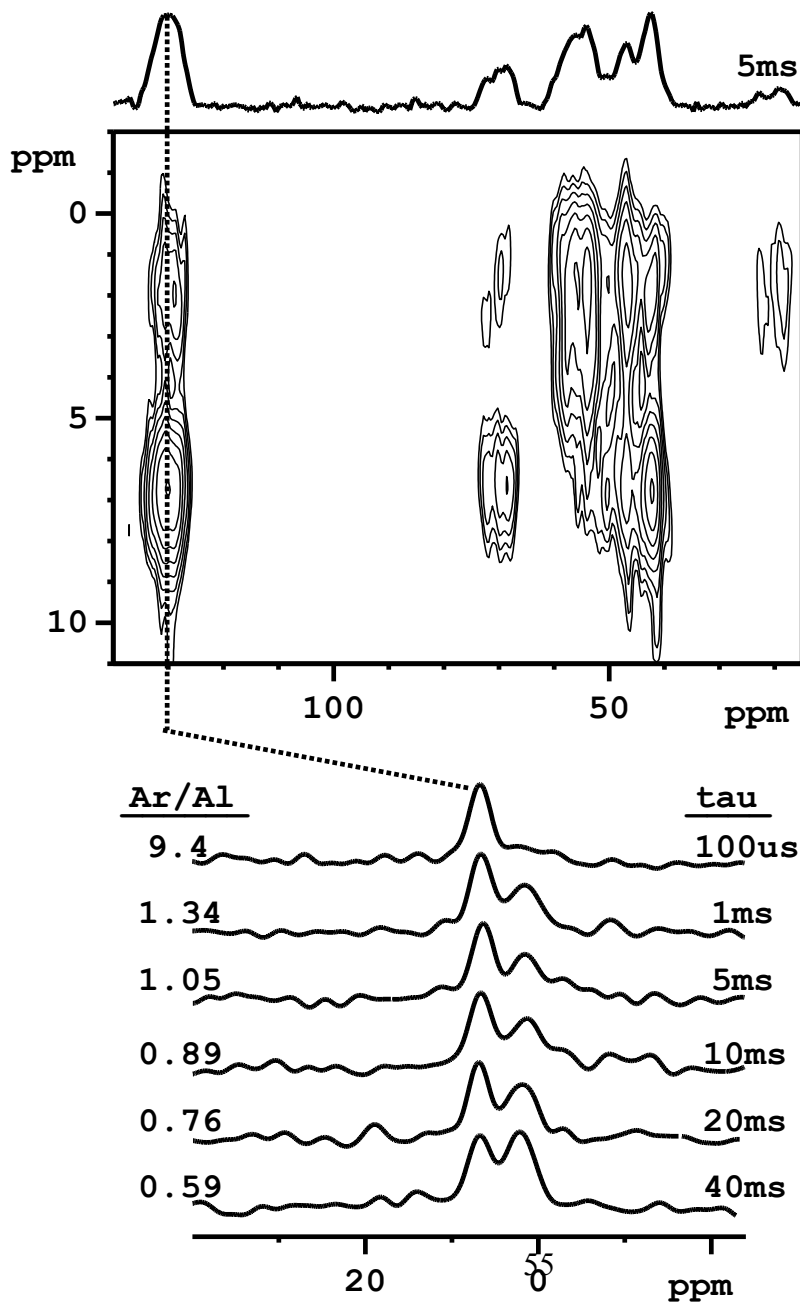


Figure 25. (top) 2D HetCor spectrum for a monodisperse PS-b-PMMA diblock copolymer obtained using a 5 ms spin-diffusion time, with the summed cross-peak projection for the ^{13}C dimension shown on the top of the plot. (bottom) Selected ^1H slices through the 128 ppm PS peak as a function of spin-diffusion time $\tau(\text{tau})$; the dashed line on the contour plot indicates the slice position.

We notice from Figure 25, that most of the cross-peaks in the spectrum have contributions from each of the two different polymers, and as long as there is one resolved peak in the ^{13}C spectrum, the quantitative length scale of mixing may be determined. In this PS-b-PMMA copolymer, we observe that the aliphatic region from 30 to 60 ppm region contains many overlapping peaks from both polymer constituents, but the PS protonated aromatic carbons at 128 ppm are well resolved, and can be used to quantitatively measure both the intramolecular and intermolecular spin diffusion. From the detailed data in Figure 26, we observe that the monomeric stoichiometric ratio for PS ($I_{\text{aliphatic}} / (I_{\text{aromatic}} + I_{\text{aliphatic}}) = 0.375$ (within a PS monomer, three aliphatic protons, and five aromatic protons) is achieved in less than 400 μs . A well-defined plateau region is observed after intramolecular equilibration, but prior to significant intermolecular spin diffusion. If the block polymers were completely phase-separated, with no spin diffusion between the blocks, the slice ratio for the 128 ppm peak would not increase over the 0.375 value.

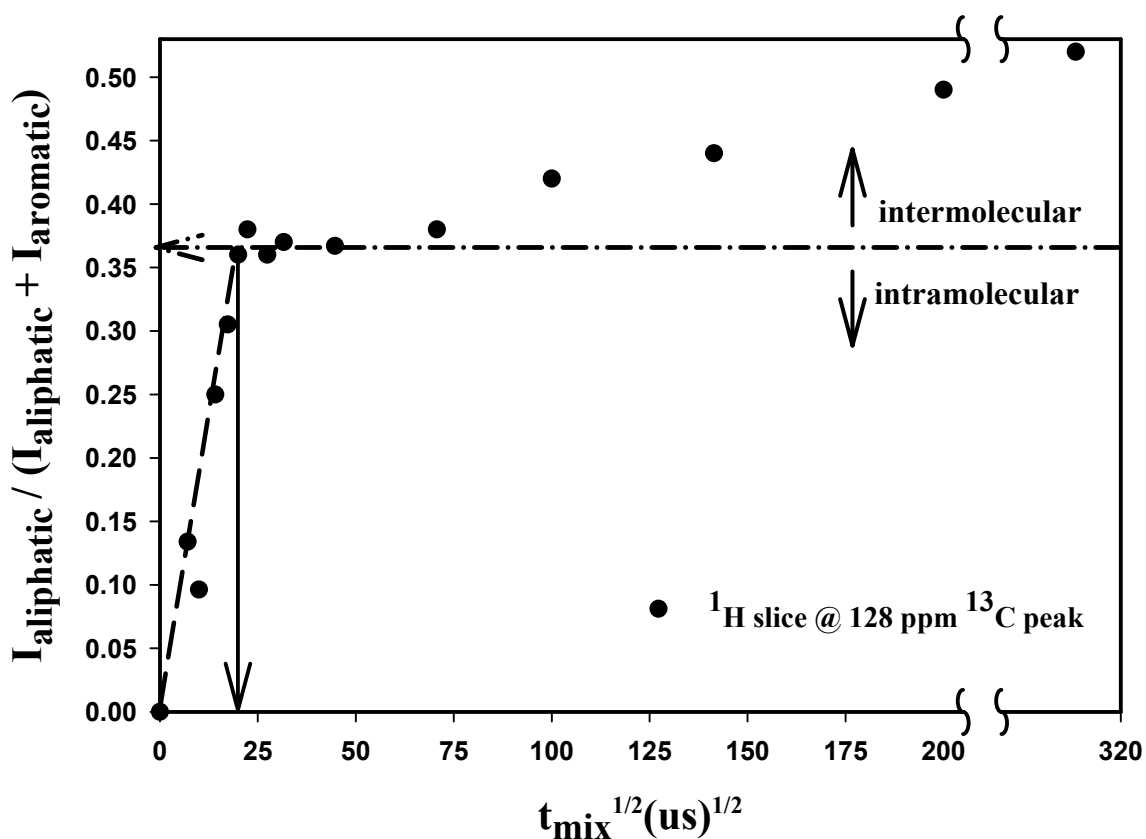


Figure 26. Complete spin-diffusion curves for the PS-b-PMMA in which the ratio of ($I_{\text{aliphatic}} / (I_{\text{aromatic}} + I_{\text{aliphatic}})$) is plotted vs the square root of the mixing time for the 128 ppm peak. Intramolecular spin-diffusion leads to the short time equilibration with the PS chains, followed by a longer intermolecular polarization transfer between the PS and PMMA blocks.

However, from Figure 26, we observe that as mixing time increases from zero, the ratio increases, reaches a plateau region, then continues to go up until it reaches the 0.6875 ratio, which comes from the intermolecular ($I_{\text{aliphatic}} / (I_{\text{aromatic}} + I_{\text{aliphatic}})$) ratio (within the copolymer structure, there are totally 11 aliphatic protons, and 5 aromatic protons). This means that the intermolecular spin diffusion does take place between the two blocks on a time scale significantly longer than spin diffusion within the individual

polymers. On the time scale of 100 ms, there is nearly complete spin diffusion within all protons of each block. We should note here that the spin-lattice relaxation T_{1H} will effect the long time spin diffusion, even so, this is extremely useful information for this polymer system, since the $T_{1\rho H}$ values are not the same for the two blocks, but the T_{1H} values are equal (1.0 ± 0.1 s for all protons in the copolymer). This is a common situation for nanoscale phase morphology in polymers, and on the basis of these experiments, we can define the length scale of mixing quantitatively, instead of defining only possible upper and lower limits based on $T_{1\rho H}$ and T_{1H} values.

A complete analysis begins by measuring intramolecular spin-diffusion equilibration to determine the value of D for the PS and PMMA blocks. From Figure 26, based on similar analysis for the neat PC or PPO, we get $(\tau_{eq})^{1/2}$ for PS = $18.75 \mu s^{1/2}$. The calculated “effective” monomer dimension for PS from the simulation software is 0.55 nm. It yields a spin diffusion coefficient of $D_{PS} = 6.9 * 10^{-12} \text{ cm}^2\text{s}^{-1}$ using equation 20. For the PMMA block, a similar analysis of slice ratios through the $-\text{OCH}_3$ carbon at 53 ppm and the $-\text{CH}_3$ carbon at 18 ppm indicates an intramolecular equilibration at $(\tau_{eq})^{1/2} = 20 \mu s^{1/2}$. Since their ^1H chemical shifts were well-resolved at zero mixing time, and this region has little or no overlap with other PS peaks in the ^{13}C dimension, we can easily follow the convergence of line shape/ ^1H chemical shift as methyl, methylene, and methoxyl polarization equilibrates within the PMMA units. No aromatic intensity was observed in the PMMA slices for mixing times less than 1 ms. So with calculated monomer size for PMMA, which is 0.50 nm, yielding $D_{PMMA} = 5.0 * 10^{-12} \text{ cm}^2\text{s}^{-1}$. Solving equation 21 for $\tau_{eq} = 100$ ms, and neglecting spin-lattice relaxation effects, the length scale of mixing for the individual PS and PMMA domains in the diblock

copolymer system is 18 nm. This is in agreement with the possible limits from the $T_{1\rho\text{H}}$ and $T_{1\text{H}}$ data (solving the diffusion equation for time limits of 15ms and 1s, respectively) and exemplifies the utility of experiments that simultaneously provide resolved intramolecular and intermolecular spin-diffusion information.

6. Conclusions

The analysis of spin diffusion of the polarization transfer within monomer units has been shown to provide quantitative spin-diffusion coefficients D , which are in agreement with those published in literature. Though ^1H static line width or relaxation methods can be used to get good estimates for D based on the fairly large amount of data in literature on model systems, such experiments usually cannot show the changes in D that may occur when a blend or copolymer is formed. While in the absence of well-characterized model polymers, and other forms of scattering data, the method described above provides a nice quantitative analysis. The 2D solid-state HetCor experiment is particularly attractive since only one resolved peak in the ^{13}C spectrum is required for measuring spin diffusion, and often the intrachain and interchain events may be separately measured and a quantitative limit on miscibility may be established. Furthermore, since all ^1H polarization is preserved for the initial condition, the results are more representative of the bulk morphology than those obtained with initial conditions generated by motional filters.

Chapter3. Enhanced Spin-Diffusion Curves in Solid Polymers by Two-Dimensional Lee-Goldburg and Windowless Multiple-Pulse Experiments

1. Introduction

^1H spin-diffusion NMR experiments are attractive for revealing the size and organization of morphological heterogeneities in solids polymers.^{61,62,93} Isotopic labeling is not required, and there are many spectroscopic and dynamic contrast mechanisms by which dissimilar components in the sample may be differentiated.^{78,26} Spin-diffusion experiments rely on the calculable spatial propagation of polarization from one region of a solid to another. Knowing the magnetization transfer rate, and the time required for all magnetization to equilibrate within the sample volume, one can determine the minimum dimension of domains (polymer-rich regions) in a heterogeneous copolymer or blend.⁹³ Analysis of spin-diffusion data has been primarily limited to the long-time response associated with polarization equilibration between morphologically distinct polymer domains. Recently, we published a detailed account of the short-time response in spin-diffusion experiments using the multiple-pulse windowless isotropic mixing (MP-WIM) HetCor sequence,⁴³ which can be used to independently calculate spin-diffusion coefficients in a pure or multiple-component polymer system.⁹⁴ In this contribution, we demonstrate that the same 2D solid-state Hetcor/spin-diffusion experiment provides superior resolution and sensitivity to polarization transfer at the intermediate times characteristic of interdomain/intermolecular spin-diffusion, with the most reliable results obtained using the Lee-Goldburg⁹⁵⁻¹¹² variant of the Hetcor experiment.

2. Experimental Section

2.1. Materials

The polystyrene-block-poly(methyl methacrylate) (PS-*b*-PMMA) diblock copolymers with each block have molecular weights $M_w \approx 55\,000$ was prepared by Polymer Laboratories, Ltd. They were monodisperse with $M_w/M_n = 1.1$. The PS-*b*-PMMA diblock copolymer with each block molecular weights $M_w \approx 25\,000$, and $M_w \approx 100\,000$ were obtained from Polymer Sources, Inc. They are prepared by living anionic polymerization in THF at -78°C using BuLi initiator in the presence of LiCl. Polystyrene macroanions were end capped with a unit of diphenyl ethylene (DPE) before adding methylmethacrylate (MMA) monomer.¹¹³⁻¹¹⁶

All the PS-*b*-PMMA diblock copolymers were conducted solid-state NMR experiments as received without any further treatments.

2.2. Solid-state NMR methods

2.2.1. Multipule-pulse Windowless Isotropic Mixing Heteronuclear Correlation Spin Diffusion Experiment (MP-WIM Hetcor)

The MP-WIM HetCor experiment was used to obtain the 2D solid-state heteronuclear correlation data. 90° pulse widths were $3.2\ \mu\text{s}$ on each channel (Figure 1). In all experiments, only one windowless isotropic mixing (WIM) cycle (total polarization time = $76.8\ \mu\text{s}$) was used. All experiments were done on a Bruker DSX-300 instrument. The

experimental verification of proper HetCor performance was done using monoethylfumarate (fumaric acid monoethylester) to both olefinic and acidic protons were observed.¹⁸ For measuring spin-diffusion throughout the polymer, controlled periods of $^1\text{H} - ^1\text{H}$ spin diffusion were introduced prior to the isotropic $^1\text{H}/^{13}\text{C}$ polarization transfer step. The chemical shift-scaling factor in the ^1H dimension was measured experimentally to be 0.42 (near the theoretical 0.47 value), and the proton frequency was shifted off-resonance by 5 kHz from the carrier to avoid any zero-frequency artifacts and take advantage of second averaging effects. Spinning speeds of 3.5 – 4.5 kHz were used to minimize potential sideband overlap with peaks of interest, and to insure good polarization transfer performance. The spinning speed periods (285 - 333 μs) were larger than twice the WIM cycle length, thereby preventing signal elimination or attenuation due to a refocusing of the C-H dipolar interaction at the end of each rotor period. Typically, 256-512 scans were taken for each of 64 points in the t_1 dimension, and recycle delays of 3-4 seconds were used. The total experiment time was typically 12-24 hours. Quadrature detection was maintained in the t_1 dimension via use of TPPI. The data were processed with 50 Hz line broadening and zero-filled to 1024 points in the t_1 dimension prior to Fourier transformation. The spin-diffusion analysis was performed by extracting individual ^1H slices in the second dimension and quantitatively deconvoluting the aromatic:aliphatic intensity ratios using PeakFit software from Jandel Scientific.

2.2.2. Frequency-switched Lee-Goldburg Heteronuclear Correlation Spin Diffusion Experiment (FSLG/HHCP Hetcor)

Frequency-Switched Lee-Goldburg (FSLG) heteronuclear ^1H - ^{13}C correlation with Hartmann-Hahn cross polarization spin diffusion (FSLG/HHCP Hetcor) experiment⁹⁵⁻¹¹² is an alternative way to get the similar spin diffusion result. This experiment coupled with fast magic angle spinning (MAS) allows the registration of 2D spectra with high resolution both in the proton and carbon dimension. The pulse sequence starts with one $\pi/2$ pulse and one magic angle θ_m pulse, directly followed by a train of frequency and phase switched Lee-Goldburg pulses in the xz plane. After the LG evolution period, a $\pi/2$ minus magic angle ($90^\circ - \theta_m$) pulse turns the proton spins to the $-z$ direction, followed by a spin diffusion time. After the spin diffusion time, a $\pi/2$ pulse turns the proton spins back to xy plane, then a spin lock period is applied, after that, with the high power proton decoupling, ^{13}C FID is acquired. The experiments were run with two τ LG period; the time period τ was optimized to 8.4 μs . The efficient transfer of magnetization to the carbon nuclei at FSLG/HHCP experiment was performed applying RAMP-CP sequence. (Since FSLG pulse sequence runs at high MAS spin speed, WIM-24 is not applied due to a refocusing of the ^1H - ^{13}C dipolar interaction at the end of each rotor period.) The RAMP-CP contact time was kept short (not more than 500 μs) to avoid the proton homonuclear spin diffusion process taking place during that period. The figure 27 shows the FSLG/HHCP Hetcor pulse sequence.

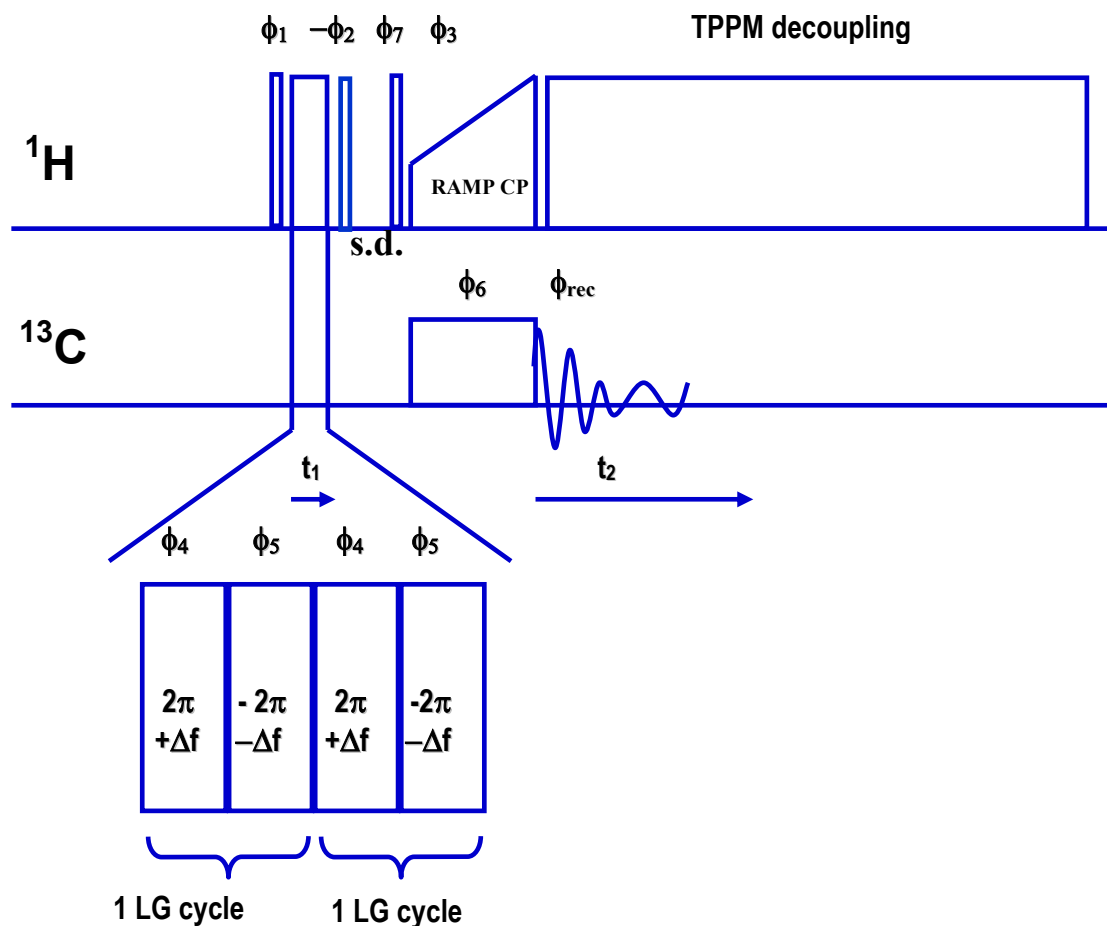
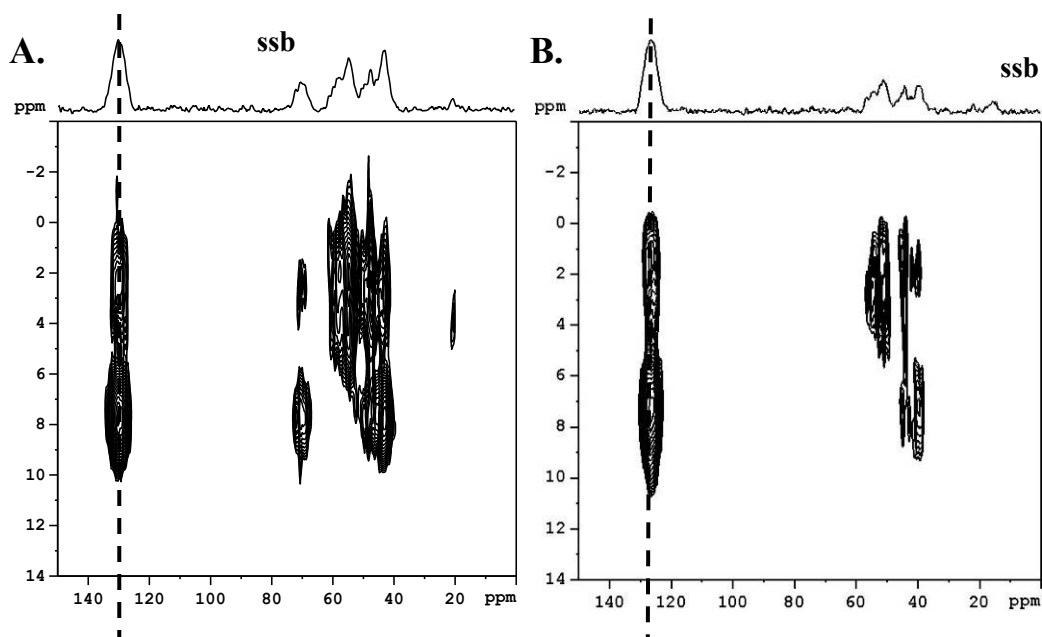


Figure 27. Two dimensional frequency-switched Lee-Goldburg with Hartmann-Hahn Cross-polarization heteronuclear correlation pulse sequence (FSLG/HHCP HetCor). ^1H r.f field strength during FSLG evolution period and TPPM decoupling period were set at 90-95 kHz, correspond with $\pi/2$ pulse of 2.65-2.75 μs . A ramp Hartman-hahn cross-polarization pulse is used; cross-polarization time is about 100 μs . Magic angle spinning speed should be high than 10 kHz to reduce the dipolar interaction.

3. Results and Discussion

Figure 28 shows an example of the 2D spin-diffusion HetCor data obtained for a symmetric PS-b-PMMA diblock copolymer with individual block sizes of 25,000 g/mole, using either the multiple-pulse windowless isotropic mixing (MP-WIM)⁴³ or frequency-switched Lee-Goldburg cross-polarization (FSLG)¹⁰³ 2D sequences. Details of the pulse sequences, changes in the spectral features with increasing spin-diffusion time, and

calculation of spin-diffusion coefficients D were previously discussed.⁷⁻⁹ Here we mention only that any individual carbon in the polymer which experiences a direct dipole coupling with a nearby proton, i.e. a coupled spin-pair, will give rise to a contour at the respective ^{13}C and ^1H chemical shift. With the introduction of a spin diffusion time in the experiment prior to the ^1H - ^{13}C polarization transfer step (a 24-pulse WIM for MP-WIM, or 100 μs ramped cross-polarization for FSLG), chemically distinct protons exchange magnetization with each other, thereby resulting in an additional correlation for any carbon peak. Polarization transfer from ^1H 's to ^{13}C 's is assumed to be isotropic, i.e., only isolated C-H spin pairs are involved in the dipolar transfer. A key advantage of the Hetcor/spin-diffusion strategy is that all ^1H magnetization is preserved in the experiment; there is no partial selection or destruction of polarization based on chemical shift or mobility filters. This insures that the sampled spin response is representative of the bulk polymer. Figure 28a, taken with a 1 ms spin-diffusion time, has two ^1H correlations for each ^{13}C peak. If one quantitatively examines the ^1H cross-section (slice) through the 128-ppm aromatic ^{13}C peak as a function of spin-diffusion time, the relative ratios of the aromatic and aliphatic ^1H peaks change in regular fashion. This is illustrated in Figure 28b, in which slices for four selected spin-diffusion times are presented. Comparison of the deconvoluted peak intensity ratio with the monomer structure indicates the time at which intramonomer equilibration is reached. Any change in the intensity ratio from this stoichiometric limit indicates spin-diffusion between different polymer regions or domains.



$$I_{\text{aliphatic}} / (I_{\text{aliphatic}} + I_{\text{aromatic}})$$

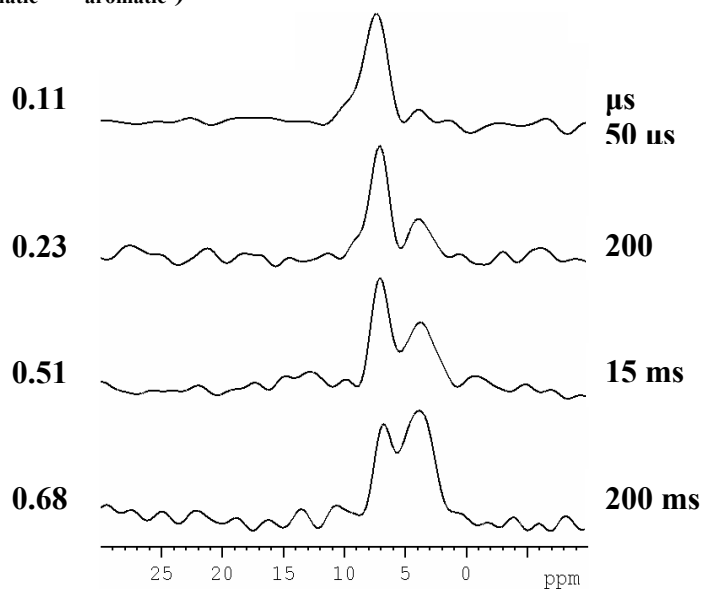
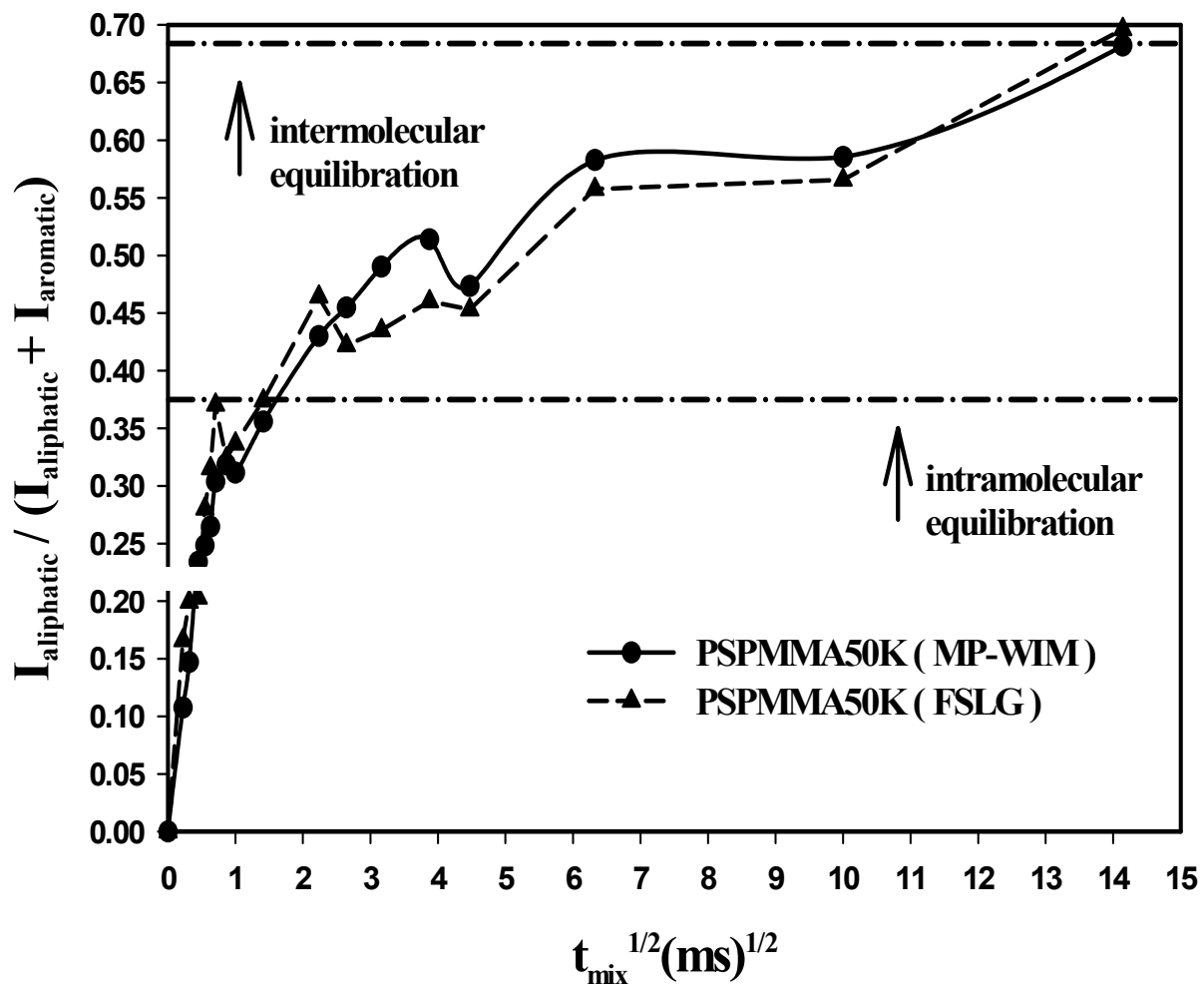


Figure 28. Representative 2D ^1H - ^{13}C HetCor plot of the 50K PS-*b*-PMMA copolymer at a spin-diffusion time of 1 ms for (a) MP-WIM vs. (b) FSLG experiment, demonstrating slightly improved resolution in the ^1H dimension for the latter. Selected ^1H slices at the PS aromatic CH signal (indicated by dashed line) are shown below the 2D plots, indicating how the spin-diffusion curves in subsequent figures were extracted from the 2D experiments. For the MP-WIM HetCor, MAS spinning speeds of 3.5 – 4.5 kHz were used, while the FSLG HetCor data were collected at 12-13 kHz. Quadrature detection in the second dimension (using TPPI) was insured by

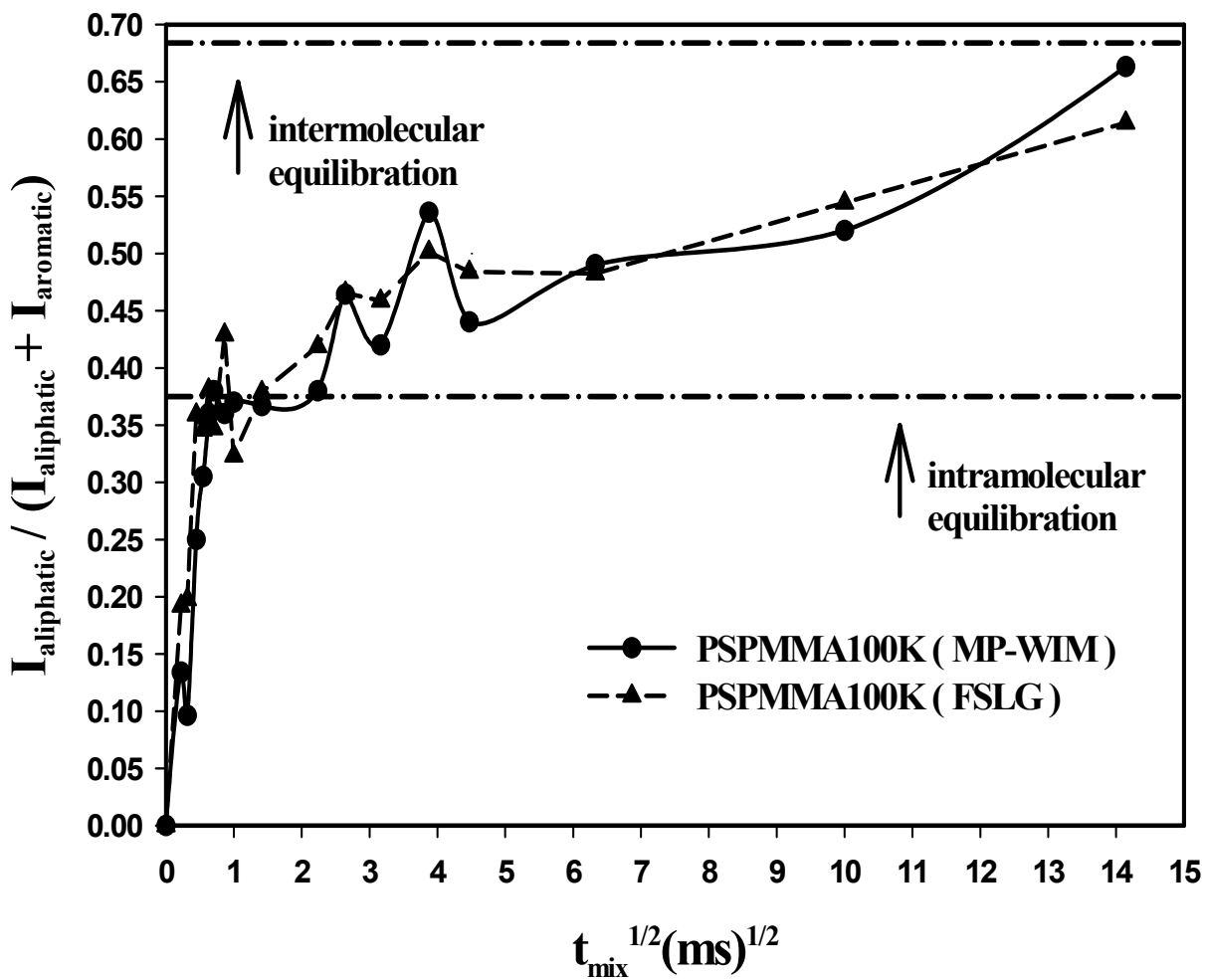
appropriate phase cycling and data addition for both the MP-WIM and FSLG experiments^{43,103}. Approximately 40 mg of sample in a 4-mm MAS rotor was used for the MP-WIM experiments, whereas only 10 mg was used for the FSLG data (due to confinement in the most homogeneous region of the r.f. coil).

The complete ¹H slice ratios obtained from the 128-ppm aromatic ¹³C resonance, at eighteen spin-diffusion times, are shown in Figures 29a-c for three PS-b-PMMA copolymers differing in their respective block sizes. Results from both the MP-WIM and FSLG experiments are presented for each copolymer. The symmetric copolymers are identified by their total molecular weight, e.g., 200K refers to the diblock containing 100,000 g/mole blocks each of PS and PMMA. Each experimental data point represents a nine-hour experiment. It is important to note that the ordinate is plotted as the ratio of signal intensities (aliphatic signal fraction), thereby removing T₁ effects for systems *with common T_{1H} values*.¹¹⁸ However, if the block sizes become large enough, disparate T_{1H}'s may exist, and must be considered. As anticipated from earlier work, the initial slopes of all curves in Figure 29 are invariant (for both the FSLG and MP-WIM data)⁹⁴, while the time required for intermolecular polarization equilibration increases with increasing molecular weight **M** (lamellar thickness $\propto \mathbf{M}^{2/3}$) of each block in the copolymer.^{93,119} The defining characteristic of the spin-diffusion curves in Figure 29 is that the detection of polarization transfer at very short times allows complete resolution of the discontinuity resulting from polarization transfer across the interface. In other words, the oft-cited sigmoidal curve is detected *following* the initial fast rate due to intramolecular magnetization equilibration. This provides a useful offset of the induction period from the zero-intensity region typically reported when measuring the growth of signals in one domain due to spin-diffusion from other regions of the polymer. With the transition between intramolecular and interdomain polarization transfer now clearly defined, the

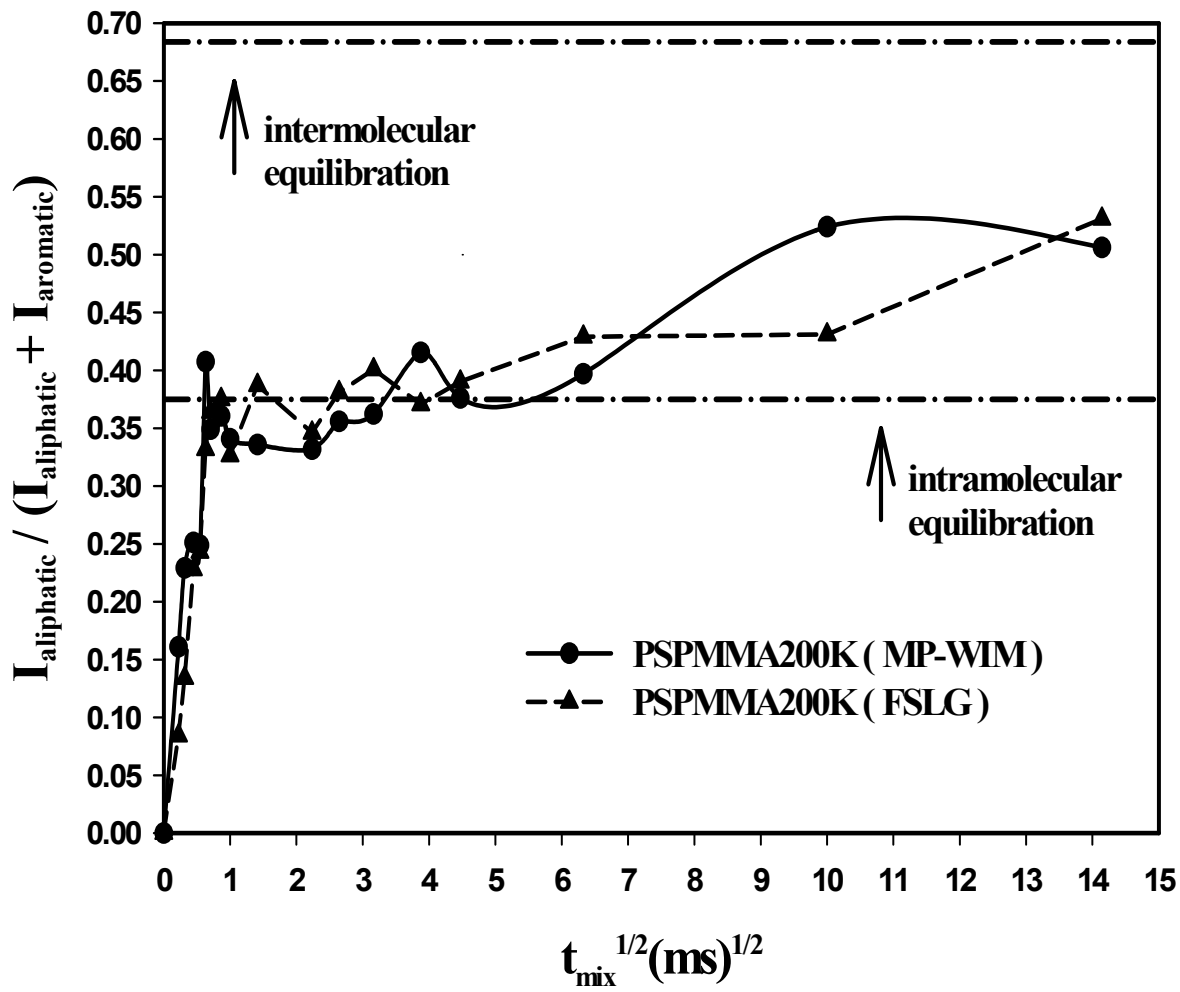
length of the induction period clearly increases for larger block sizes. For comparison, Figure 29d shows a schematic representing a typical spin-diffusion curve obtained by any of a number of methods that do not resolve intramolecular vs. inter-domain events (e.g., Goldman-Shen, dipolar filter, chemical shift filter, etc.¹¹⁷). Typically, these types of experiments either select, or selectively destroy, magnetization from one component in a binary blend/copolymer, and the return of that magnetization is measured versus time. As such, the curve starts at zero intensity, as shown in 29d, and any oscillations that may be present in the initial polarization growth are lost in the noise. Indeed, a survey of published curves similar to 29d indicates that fluctuations near the zero line that are larger than the noise in the curve often occur, but the simple fact that the signal is so small *at short interdomain polarization transfer times* precludes any quantitative interpretation of the effect. In the majority of cases, experiments of the type represented by Figure 29d are completely sufficient for studying phase behavior, since one is most often interested in determining mixing length scales in a heterogeneous system, i.e., inter-domain spin-diffusion. Further, such methods are less time-consuming than the data shown in Figures 29a-c. However, the ability to detect the full spin-diffusion response, and resolve the transition region between intra- and intermolecular transfer, is necessary for a complete, fundamental understanding of polarization transfer in amorphous, heterogeneous polymer systems.



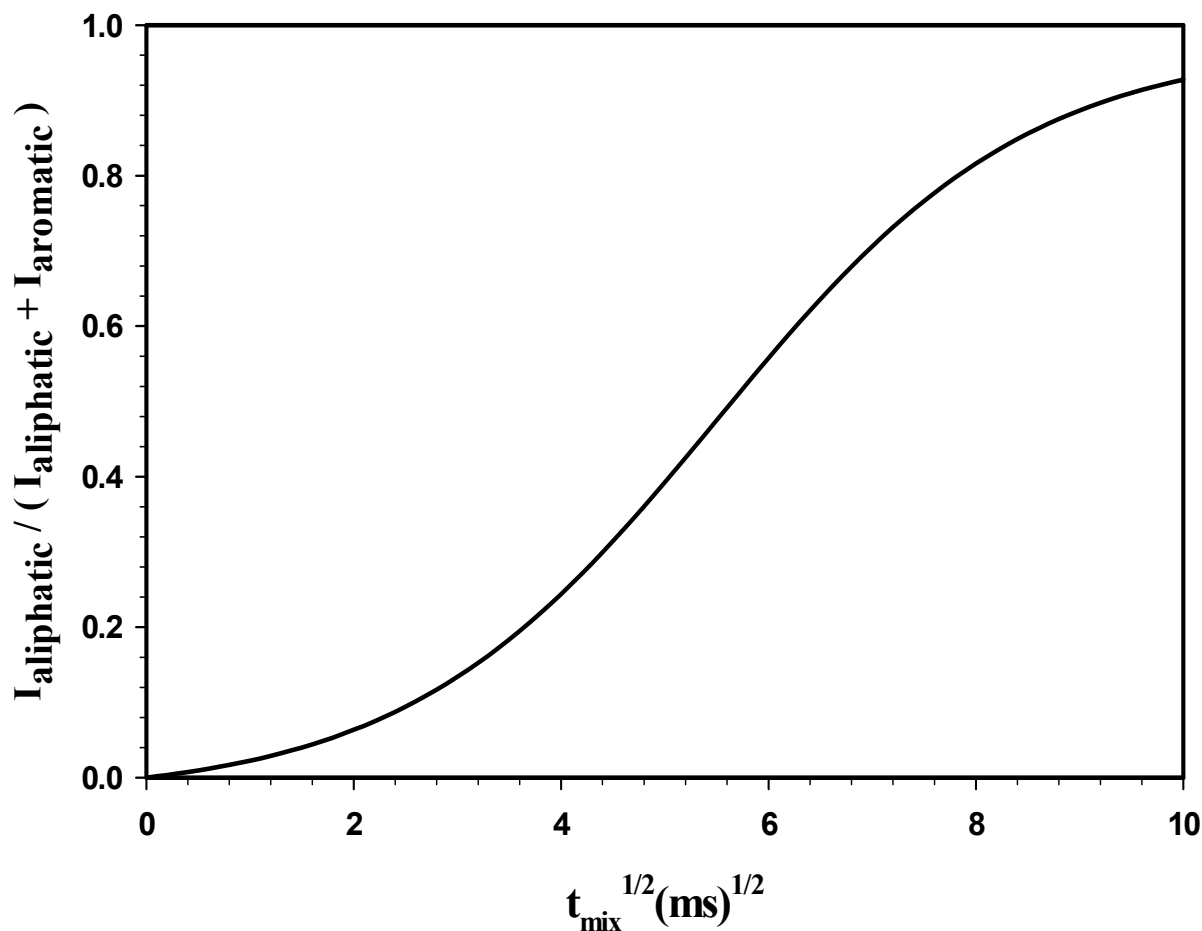
A.



B.



C.

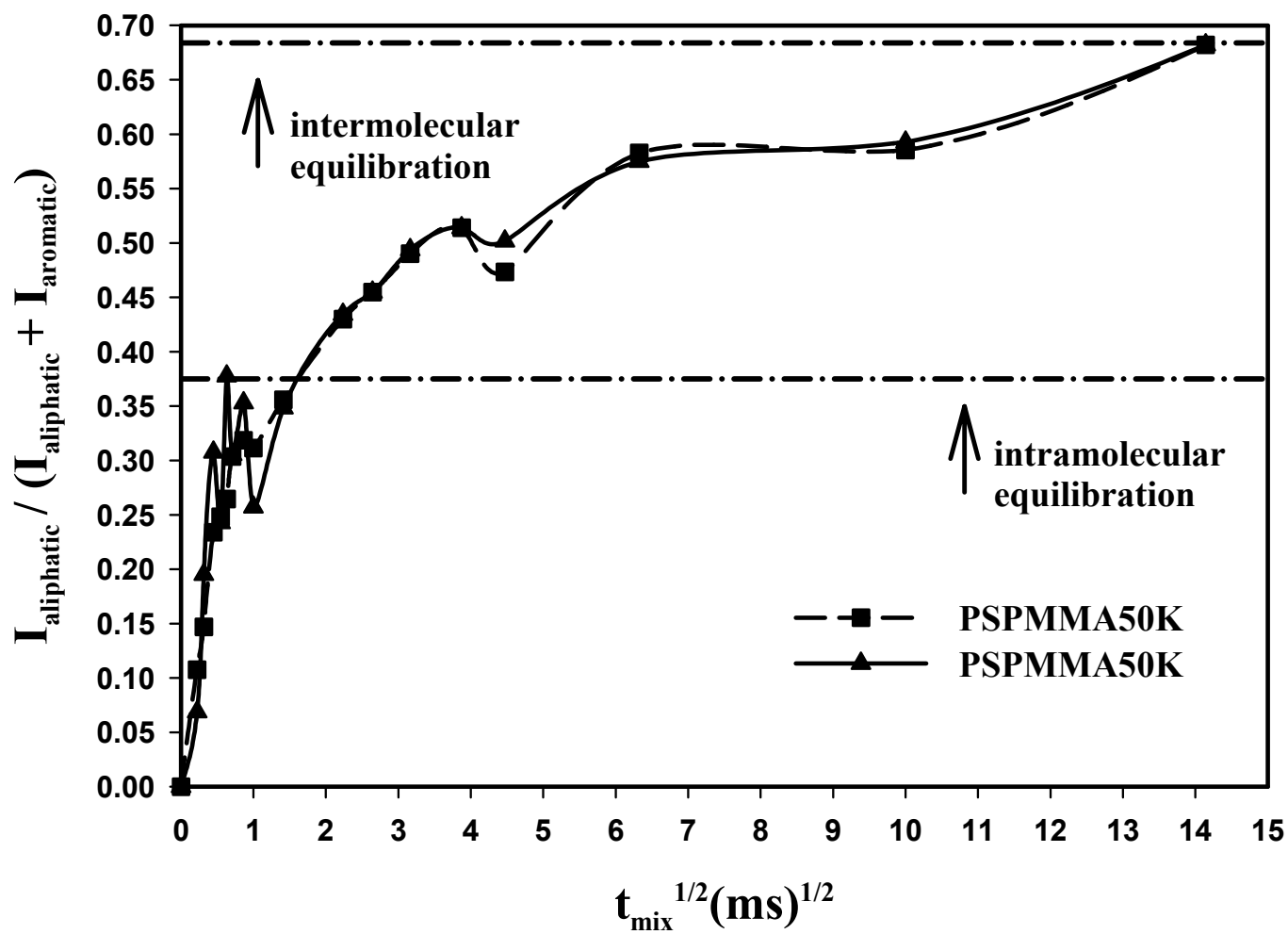


D.

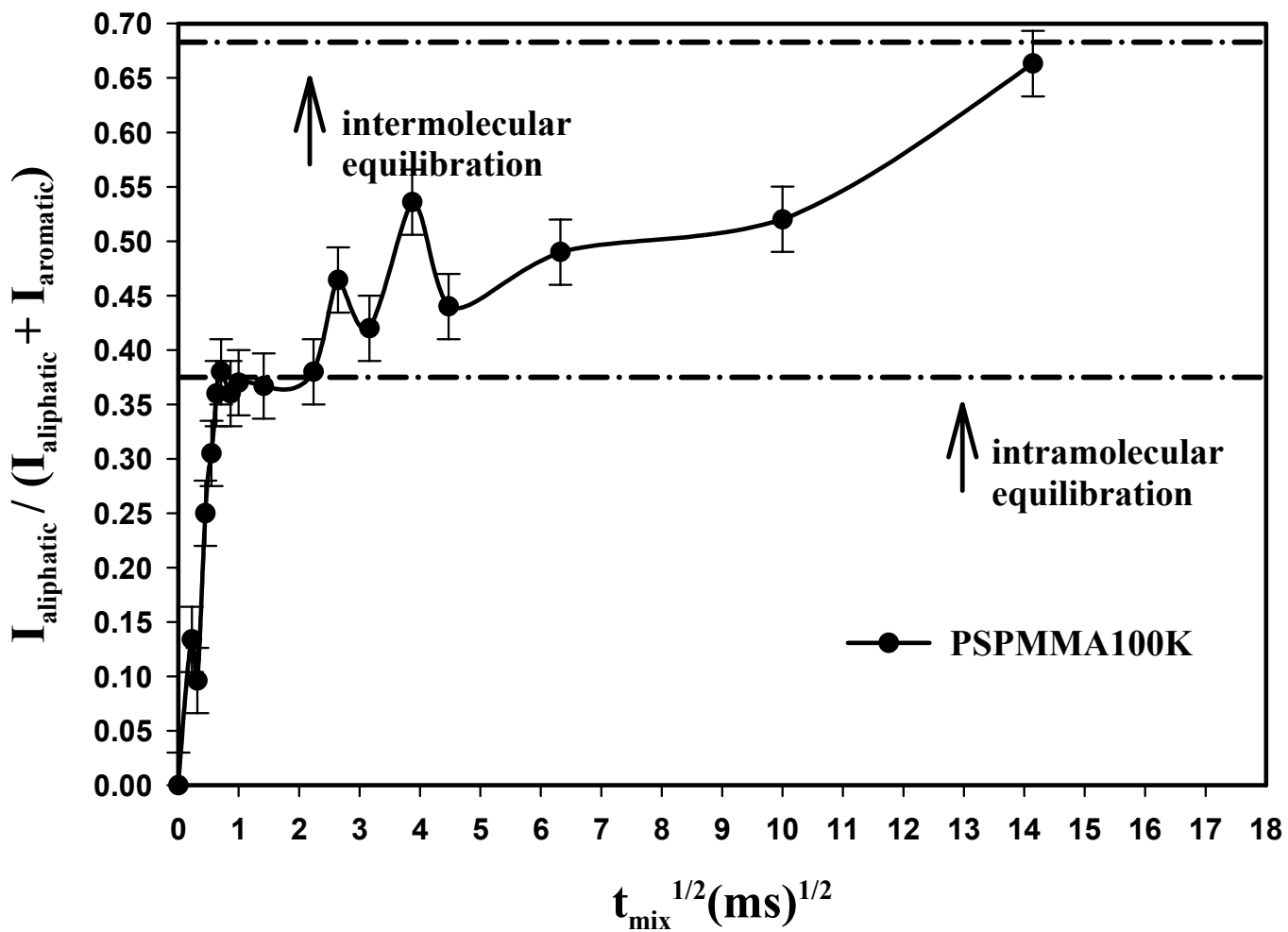
Figure 29. Total spin-diffusion curves obtained using Lee-Goldburg (FSLG) vs. multiple-pulse HeteroCorrelation (MP-WIM) for (a) PS-b-PMMA with a total molecular weight of 50K (25K blocks for each component); (b) PS-b-PMMA with a total molecular weight of 100K; (c) PS-b-PMMA with a total molecular weight of 200K. In (d), a schematic of a typical spin-diffusion curve resulting from the measurement of only interdomain polarization transfer is shown. The lines are drawn merely to guide the eye in examining the different responses.

Examination of the total spin-diffusion curves in 29a-c reveals larger oscillations near the interfacial/intermediate regions of the MP-WIM curves relative to those obtained with FSLG. Figure 30 summarizes the experimental measures we have taken to insure that the

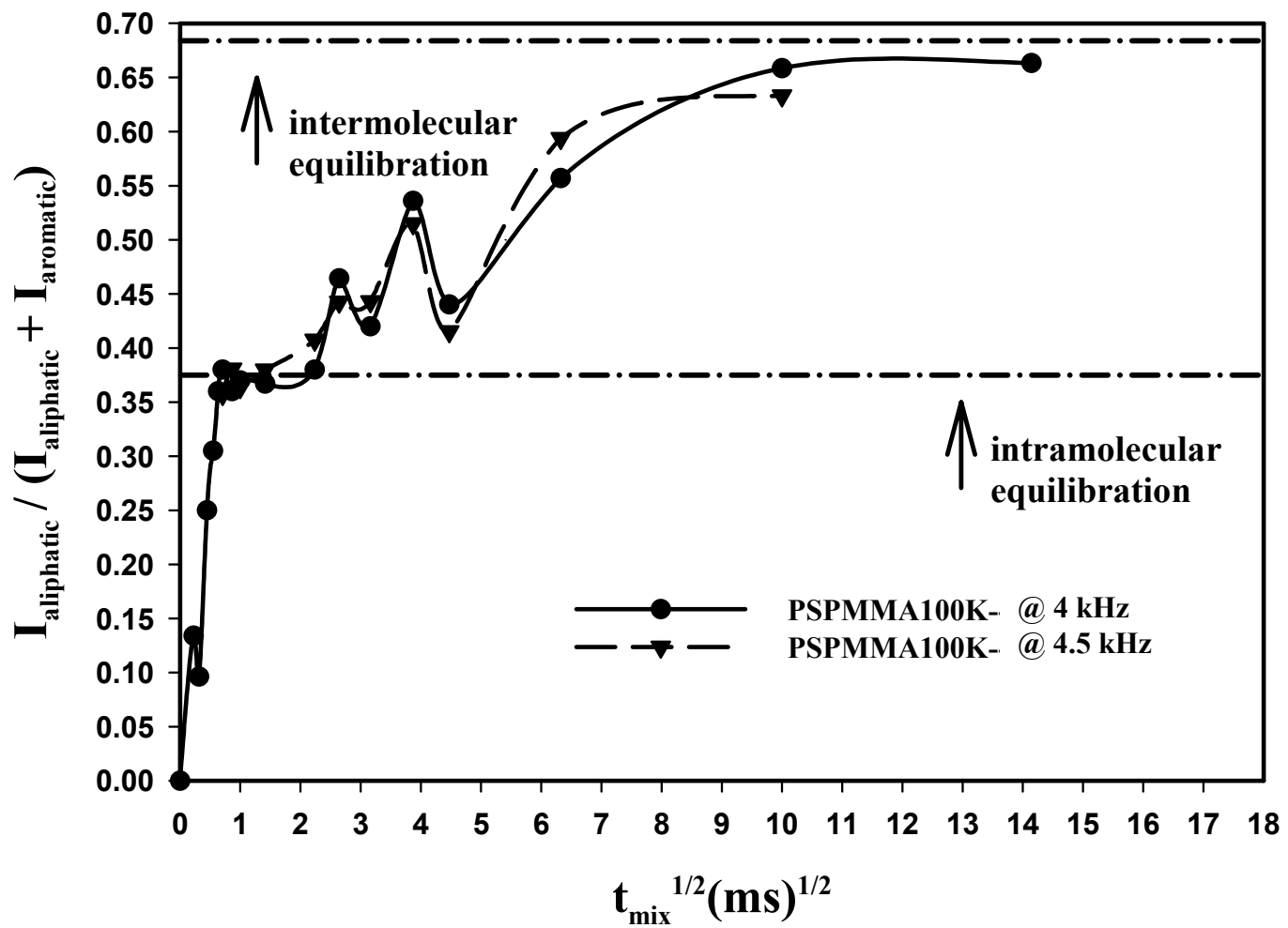
intensity ratios extracted from the MP-WIM 2D data are reproducible. Figure 30a shows the results of duplicate data analysis on the same set of 50K data. Lines have been added as visual aids, and from this, one observes good point-by-point reproducibility for the process of slice selection, deconvolution, and integration of the 2D data. Figure 30b shows representative error bars calculated based on the acquisition of four random data points from all three diblocks in triplicate, i.e., three separate MP-WIM Hetcor experiments at the same spin-diffusion time. Four different spin-diffusion times were chosen, ranging from very short to the long-time regime, resulting in twelve separate experiments probing reproducibility. The error bar given is simply the maximum range obtained for any one of the four randomly sampled points.



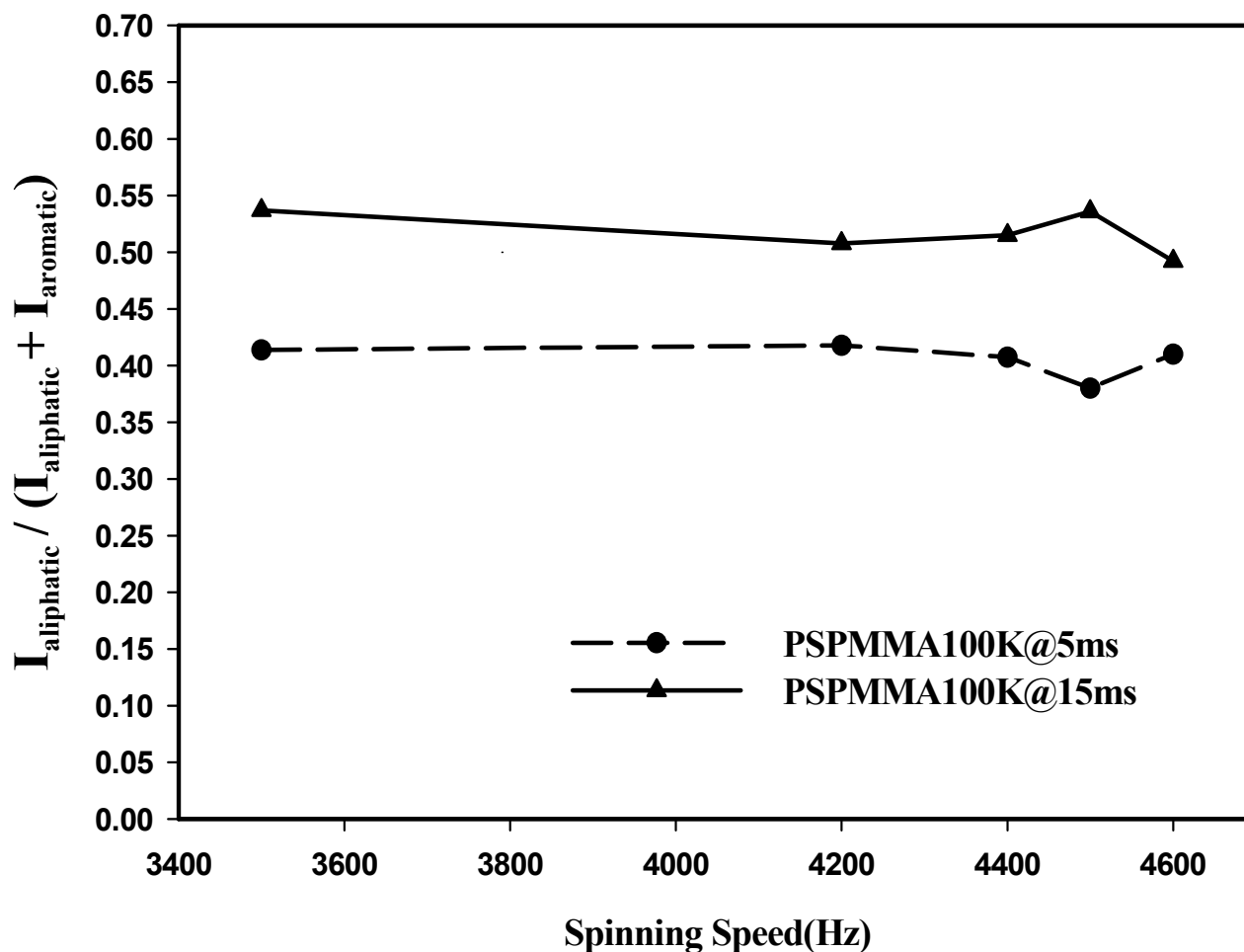
A.



B.



C.



D.

Figure 30. (a) MP-WIM spin-diffusion curves for PS-b-PMMA with a total molecular weight of 50K, in which the same 2D Hetcor data set was analyzed twice (phasing, slice selection, deconvolution, and intensity ratio determination). (b) MP-WIM spin-diffusion curve for PS-b-PMMA 100K with representative error bars determined by triplicate experiments on four randomly selected spin-diffusion mixing times (details described in the text). (c) MP-WIM spin-diffusion curve for PS-b-PMMA 100K obtained at two different MAS speeds. (d) Plot of 128-ppm PS aromatic C-H slice intensity versus MAS speed for MP-WIM spin-diffusion experiment at two different spin-diffusion times.

Since the range of 0.06 presented in Figure 30b was obtained in only one measurement, and all three others had ranges less than half of that indicated (< 0.03), we feel that these error limits are quite generous. Therefore, the oscillations of the type seen in Figures 29 and 30, which appear near the interface region of the curve where interdomain polarization transfer begins, are outside the limit of error in most cases. Since these oscillations do not appear with the same intensity in the FSLG experiments, we must conclude that they are experimental artifacts associated with the simultaneous application of the multiple pulse BLEW-12 (^1H channel) and BB-12 (^{13}C channel) $\pi/2$ pulse trains during the evolution time. While we have attempted to change the relationship between the effective multiple-pulse cycle time and the rotor period by varying MAS speeds (Figure 30c and 30d) and $\pi/2$ pulse widths (data not shown), the magnitude of these reproducible oscillations in the MP-WIM intermediate-time data could not be reduced. In this regard, the FSLG method is a superior alternative, and also delivers increased sensitivity relative to the MP-WIM (see caption on Figure 28). While there was a small resolution enhancement using FSLG relative to MP-WIM HetCor, large improvements are not to be expected for glassy, amorphous polymers like the ones used in this study.

4. Conclusions and Future Work

The experimental approach described here results in the acquisition of the complete spin-diffusion response of an amorphous polymer system, and in particular, an enhanced resolution of the induction period for inter-domain polarization exchange. Future work will focus on the development of a robust simulation strategy for the integration of

intramolecular, interface, and interdomain spin-diffusion responses and pertinent structural correlations in amorphous blends and copolymers.

Chapter 4. Two-Dimensional Spin Diffusion NMR Reveals Differential Mixing in Biodegradable Polyester Blends

1. Introduction

Characterization of amorphous mixtures is central to intelligent design and application of multicomponent materials, including inorganic glasses, organic polymers, or composites containing both organic and inorganic constituents¹³⁵. Understanding of structure in these “disordered” systems is constrained by the obvious limits on diffraction experiments, and optical, electron, or neutron scattering often suffer from insufficient contrast for mixtures of chemically similar materials. Blends of biodegradable polymers, such as aliphatic esters, are a typical example of targeted amorphous mixtures whose physical properties are currently deficient relative to more established polyolefins^{127-133,136}. Optimization of physical properties in biodegradable polymers, and the resulting environmental benefits from new commercial applications, is hampered by the lack of molecular- and meso-scale characterization data on the end-use polymer mixtures. Magnetic resonance has proved useful in the analysis of phase behavior in many amorphous polymer blends, since several types of experiments can provide mixing scale information without having to dissolve the macromolecules, incorporate isotopic labels, or synthetically incorporate contrast agents^{26,117,137}. In general, there are distinct characteristics common to the polymers in most previously published reports where NMR was successfully used to study bulk mixing behavior. The individual blend constituents possessed either (1) significantly different values of T_g , and therefore, differential chain dynamics in the blend; (2) different relaxation rates (e.g., T_1 , $T_{1\rho}$, or T_2); or (3) a large range of ^1H chemical shifts in their NMR spectrum (e.g., both aliphatic

and olefinic/aromatic). While variable-temperature experiments may improve spectroscopic contrast in systems that do not exhibit sufficiently disparate values in any of these categories, such changes are often incongruent with critical solution temperatures. Therefore, a clear need exists for a generally applicable approach to determine mixing length scales in amorphous blends of polymers with similar chemical, physical, and spectroscopic properties.

In this contribution, we describe the extension of a previously published experimental approach to such a class of materials^{94, 128}. Specifically, we prepare binary, amorphous polymer blends of PCL (polycaprolactone) and PLLA (poly-L-lactic acid), using two different preparation methods. These aliphatic polyesters are important candidates for economically viable biodegradable polymers, and in addition offer the promise of biocompatibility. PCL has high flexibility with low tensile strength. Its melting point is 60°C and it has a glass transition temperature of -40°C. On the other hand, PLLA has a high tensile strength, high melting point (ca. 160°C), and a relatively high T_g = 60°C. Due to its high crystallinity, PLLA is very brittle with low elongation at break. Separately, neither polymer offers attractive performance attributes. Together, as a compatible blend, they can offer a sufficiently tough but pliable biopolymer suitable for a variety of pharmaceutical, biomedical, and environmental applications^{124,125,138,139}. However, PCL and PLLA are incompatible, and phase separate when prepared using simple solution or melt-blending methods. Recently, Rusa and coworkers have shown that compatibility in PCL-PLLA blends is enhanced using inclusion-compound coalescence methods^{120,125}. However, quantitative proof of the length scales of mixing in solution vs. inclusion-compound blending methods were not reported.

Here we demonstrate that two-dimensional spin-diffusion NMR experiments indicate that the length scale of mixing is reduced via the inclusion compound coalescence method, i.e. enhanced compatibility for the PCL/PLLA blend. The PCL/PLLA system is an excellent representative example of a blend in which the constituents have similar NMR relaxation properties, similar chain dynamics once they are blended, and a relatively small ^1H chemical shift dispersion. In addition, there is a clear connection between the practical utility of this amorphous blend as a biocompatible/biodegradable material, and subtle differences in its morphology. Permeability and biodegradation rates are critical determinants for controlled-drug delivery candidates, as well as general environmental reclamation concerns, and these in turn depend upon the morphological details of blends¹²⁵. As such, the general applicability of the two-dimensional spin-diffusion technique to mixing problems in polymer blends is clearly demonstrated.

2. Experimental section

2.1. Sample Preparation

PCL and PLLA were each synthesized at 115°C by ring-opening polymerization of ϵ -caprolactone and L-lactide (both from Aldrich), respectively¹²⁵. Syntheses were carried out in toluene, with 1-dodecanol and SnOct (ca. 0.1% of monomer in molar amount) used as the initiator and catalyst, respectively. Polymers were purified by cold methanol precipitation, followed by drying at 40°C in a vacuum oven for 48 hours. Both polymers had $M_n \approx 10,000$ g/mol, with polydispersity ≈ 1.2 . Blend preparation by solution was accomplished by dissolving an equimolar mixture of each polymer in acetone to generate a ca. 2-5 wt% solution of the polymers, followed by precipitation with water. Preparation of PCL-PLLA blends via coalescence from their inclusion compounds with cyclodextrin

in acetone has been described in detail previously, and the identical method was used in this case¹²⁰⁻¹²³. Briefly, the coalesced PCL-PLLA blend was obtained by washing the inclusion compounds with DMSO, followed by subsequent drying in a vacuum oven for a minimum of 48 hours.

Characterization of the coalesced PCL-PLLA blend by polarizing microscopy, DSC, and X-ray diffraction revealed that only $\leq 5\%$ crystallinity was present in the blend, and that no distinct morphology or domain structure was present. In contrast, weak but distinct PCL and PLLA diffraction peaks remained for the dioxane-cast blend, suggestive of a longer length scale of mixing with some residual regions of crystallinity¹²⁰.

2.2. Solid-state NMR Methods

All the solid-state NMR experiments were performed on a Bruker DSX-300 instrument using 4mm zirconium oxide rotors, operating at field strength of 7.05 T, corresponding to a 300 MHz ¹H Larmor frequency and 75 MHz ¹³C Larmor frequency. ¹H Bloch decay spectra were acquired using magic angle spinning (MAS) speeds of 4 and 13 kHz and a 3.5 μ s $\pi/2$ pulse width. ¹³C Cross polarization/Magic angle spinning pulse sequence (CP/MAS), T₁(H), T_{1 ρ} (H) measurements were performed with 3-4 kHz MAS and 3-3.5 μ s $\pi/2$ pulse width. Radio-frequency field strengths for ¹H decoupling, unless otherwise specified, were 70-73 kHz. The cross-polarization contact time was 1 ms, the delay between two consecutive scans was 2-4s. ¹H T₁'s were measured via ¹³C detection using the combination of cross polarization and saturation-recovery pulse sequence, while ¹H T_{1 ρ} 's were acquired using a cross-polarization pulse sequence preceded by a variable proton spin-lock period.

The two dimensional (2D) ^1H - ^{13}C spin diffusion heteronuclear correlation (Hetcor) data were obtained using two different experimental techniques, with similar results obtained by each. The multiple-pulse windowless isotropic mixing Hetcor (MP/WIM) sequence first reported by Burum et. al. ⁴³, as well as a 2D frequency switched Lee-Goldburg with Lee-Goldburg cross-polarization (2D FSLG/LGCP), were used to obtain the 2D solid-state heteronuclear correlation data reported here^{95,102}. The FSLG/LGCP HetCor pulse sequence was shown at figure 31.

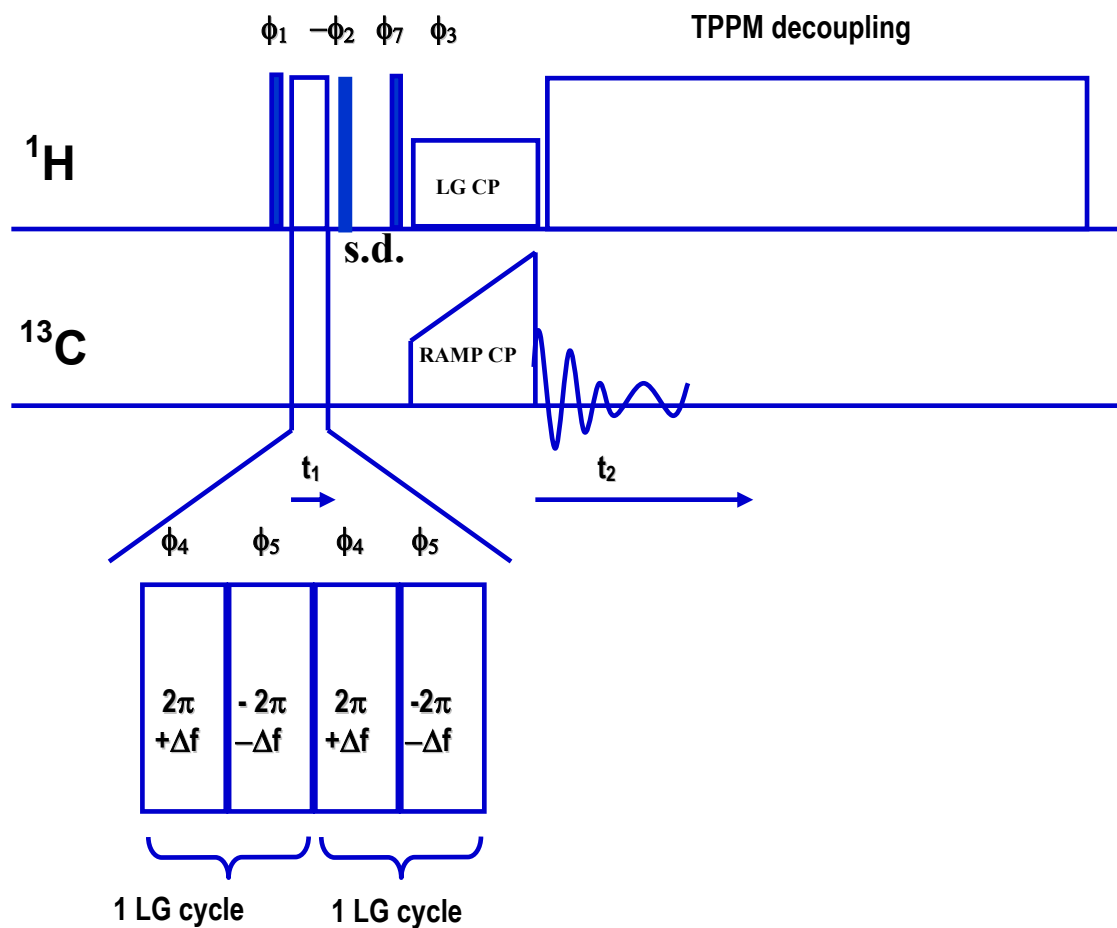


Figure 31. Two dimensional Frequency-switched Lee-Goldburg heteronuclear correlation experiment with Lee-Goldburg cross-polarization pulse sequence. ^1H

radiofrequency field strength during FSLG evolution period and TPPM decoupling period were set at 90-95 kHz, correspond with $\pi/2$ pulse of 2.65-2.75 μs . At ^1H LGCP period, radiofrequency field strength is 64-68 kHz, correspond with $\pi/2$ pulse of 3.7-3.9 μs . ^{13}C ramp CP is used, CP time = 100 μs . MAS speed = 13 kHz. Quadrature detection in t_1 is achieved by TPPI.

Specific parameters for the MP/WIM HetCor experiments are identical to those used in our previous study, but briefly include $\pi/2$ pulse widths = 3.2 μs on each channel, MAS speeds = 4 kHz, and insertion of controlled periods of $^1\text{H} - ^1\text{H}$ spin diffusion were introduced prior to the isotropic $^1\text{H}/^{13}\text{C}$ polarization transfer step. For the FSLG/LGCP HetCor data, the heteronuclear polarization transfer (CP time = 100 μs) under ^1H Lee-Goldburg conditions, and 13 kHz MAS, insures that homonuclear ^1H spin diffusion does not occur during the CP contact period¹⁰². (In contrast to similar experiments where a normal Hartman-Hahn spin-lock was applied for the same 100 μs CP period (FSLG/HHCP), no cross peaks were observed in the FSLG/LGCP experiments, in agreement with the MP/WIM data. The weak cross-peaks observed in the FSLG/HHCP version of the experiment revealed that some homonuclear ^1H spin-diffusion “leaked” between chemically distinct protons during the CP time, which is not desirable for quantitative determination of spin-diffusion coefficients.) The ^1H radiofrequency-field strength during the FSLG evolution period and TPPM decoupling period were set at ca. 95 kHz. Quadrature detection in t_1 was achieved by time proportional phase incrementation (TPPI) for each HetCor method. In all cases, experimental verification of proper HetCor calibration was done using monoethylfumarate¹³⁴. Spin-diffusion curves were constructed by extracting individual ^1H slices in the second dimension and quantitatively deconvoluting the appropriate intensity ratios using Jandel Scientific’s PeakFit software.

2.3. Simulation of Polymer Chain Units

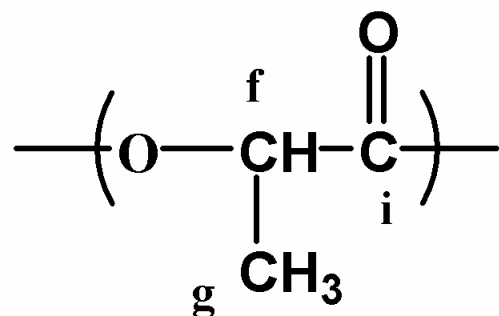
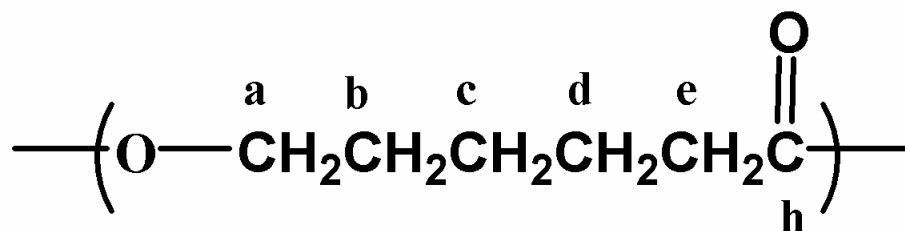
Characteristic monomer sizes for spin-diffusion were determined via molecular dynamics calculation and dimensional measurements on PLLA chains with degrees of polymerization = 99, using the Insight II molecular modeling package (Polymer version 3.0.0) with PCFF force field parameters running on a Silicon Graphics IRIS Indigo workstation. Energy minimization was computed with 5000 iterations of an adjusted-basis steepest-descents algorithm. Dynamics simulations were carried out at constant temperature of 300 K for 5 ps with time step of 1 fs. The minimum distance between pendant CH₃ protons and the OCH proton on the backbone (0.248 nm) defines the average PLLA monomer size for intramolecular ¹H spin-diffusion, since these are the only two unique PLLA protons present; an identical distance was calculated trigonometrically. PCL, which has a more complicated structure containing several different proton types, was found to have a characteristic monomer size $\chi = 0.38$ nm using a similar structure simulation routine. Details of the calculation for characteristic monomer dimensions have been described previously⁹⁴.

3. Results and Discussion

One-Dimensional ¹H and ¹³C Solid-State NMR Analysis.

Figure 32 shows ¹H one-pulse spectra for the two PCL-PLLA blends in bulk, obtained at 30°C using 13 kHz MAS. Identical spectra were collected using 4 kHz MAS (not shown). Examination of the spectra and structure assignments reveals that (1) the

total resolvable chemical shift separation is less than 3 ppm, (2) the peak widths are large, and (3) no resolved signals exist in the blend by which one can differentiate PCL and PLLA protons (Figure 32c). These spectral characteristics render difficult the use of direct ^1H spin-diffusion methods for quantitative interrogation of phase behavior in the blends. The ^1H spectrum for the solution blend (not shown) is identical to the coalesced blend. In contrast, the ^{13}C CP/MAS spectra in Figure 32d and 32e show well-resolved signals for each carbon type originating from both PCL and PLLA, including the aliphatic signals from the ester linkage (65-75 ppm). Poorly resolved ^1H spectra, but well-resolved ^{13}C data, are common in solid polymers, and ^{13}C detection of the ^1H spin-lattice ($T_{1\text{H}}$) and rotating-frame ($T_{1\rho\text{H}}$) relaxation times routinely provide a mechanism to discern length scales of mixing^{26,117,134}. However, this requires that the individual relaxation times be sufficiently distinct (typically \geq to a factor of 2) to obtain accurate domain size information¹¹⁷.



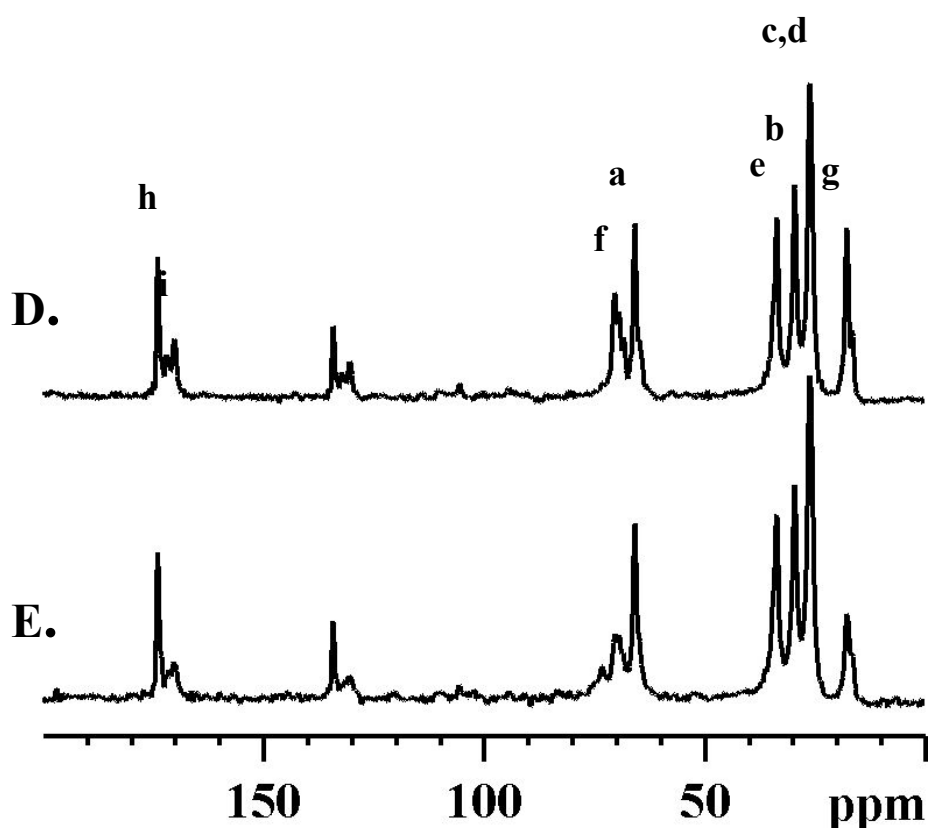
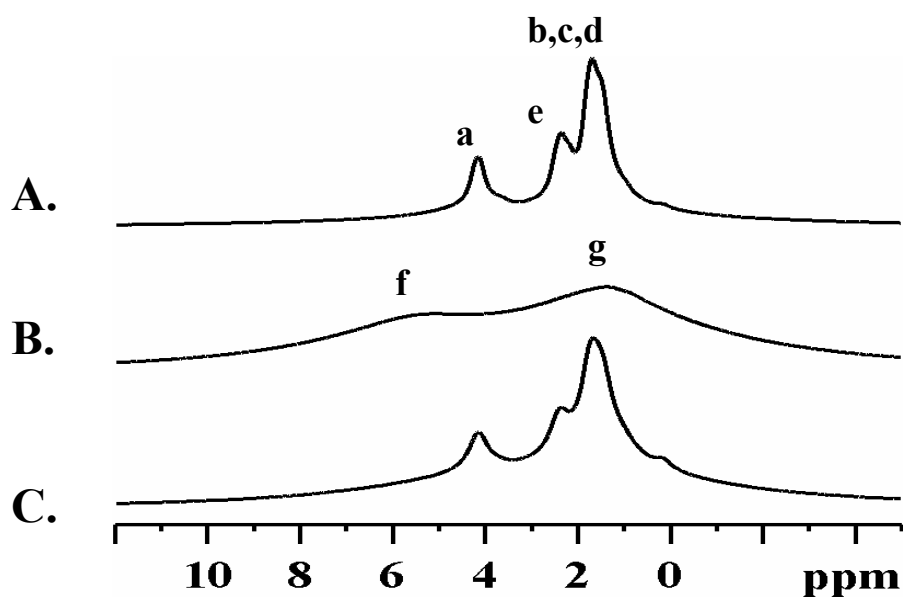


Figure 32 (a) ^1H Bloch decay spectrum of pure bulk PCL; (b) ^1H Bloch decay spectrum of pure bulk PLLA; (c) ^1H Bloch decay spectrum of coalesced PCL/PLLA blend; (d) ^{13}C CP/MAS spectrum for the solution PCL/PLLA blend; (e) ^{13}C CP/MAS spectrum for the same sample as in (c). Assignments follow the structure schematic (top). Spectra (a) – (c) were acquired with 13 kHz MAS. Asterisks denote spinning sidebands.

Tables 1 and 2 show that the ^1H relaxation times for the individual blend components are too similar to reliably extract mixing dimensions. In addition, we observe from Table 1 that $T_{1\rho\text{H}}$ values are different even within the pure polymers, further complicating the use of $T_{1\rho\text{H}}$ values for length scale of mixing calculations in this case, and also demonstrating the danger of this approach for blends of mobile polymers unless the temperature is reduced significantly¹⁴⁰. Finally, we note that attempts to exploit ^1H T_2 differences to selectively eliminate all of the ^1H magnetization from either the PCL or the PLLA component in the coalesced blend, which would have allowed spin-diffusion measurements using either a ^1H - or ^{13}C -detected dipolar filter experiment^{128,141,142}, were not successful. All peaks in the ^1H and ^{13}C spectra were equally attenuated with increasing filter cycle strength (data not shown).

<u>Peak (ppm)</u>	<u>Pure PCL (ms)</u>	<u>Pure PLLA (ms)</u>	<u>Blend (ms)</u>	<u>Coalesced (ms)</u>
67	62.9		70.6	49.9
30	38.9		47.7	38.6
27	32.6		37.8	37.6
71		38.7	30.1	40.2
19		25.2	42.3	45.3

Table 1. ^1H rotating-frame spin-lattice relaxation time constants $T_{1\rho\text{H}}$ (in milliseconds) for PCL/PLLA blends versus sample preparation method.

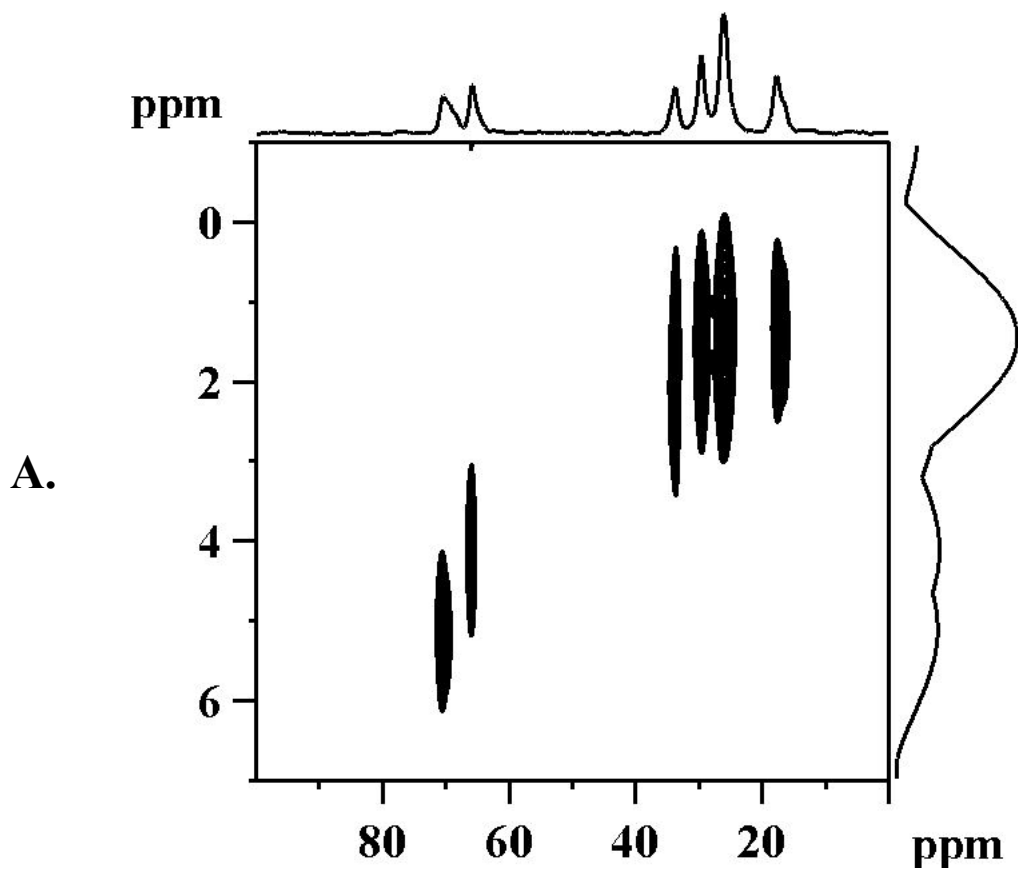
Peak (ppm)	Pure PCL (s)	Pure PLLA (s)	Blend (s)	Coalesced (s)
67	1.67		1.04	0.88
30	1.78		1.04	0.86
27	1.88		1.02	0.85
71		1.20	0.74	0.77
19		1.20	0.84	0.98

Table 2. ^1H spin-lattice relaxation time constants T_1 (in seconds) for PCL/PLLA blends versus sample preparation method.

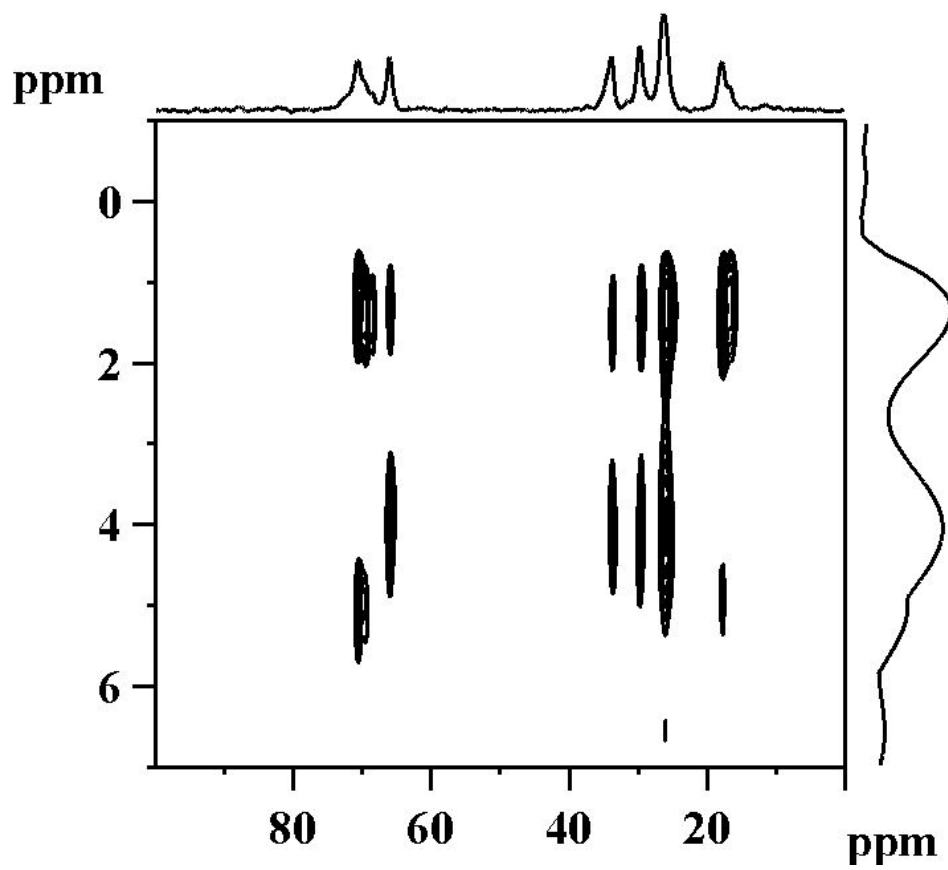
Two-Dimensional Spin-Diffusion NMR.

The constraints discussed above suggest that the PCL/PLLA blend system is an ideal candidate for analysis using 2D spin-diffusion HetCor methods^{43,79-81}. We have previously demonstrated that this technique can independently determine spin-diffusion coefficients and length scale of mixing in polymers and copolymers, since both polarization equilibration within monomeric units and between distinct polymer domains may be resolved⁹⁴. Representative 2D spin-diffusion HetCor plots are shown in Figure 31 for the coalesced blend. While many plots (> 30) were obtained using both types of HetCor pulse sequences with several spin-diffusion times, only a small subset of the data is shown in Figure 33 for brevity. Figures 33a/33b and 33c/33d illustrate that identical results were obtained using both the FSLG/LGCP and MP/WIM Hetcor sequences, and

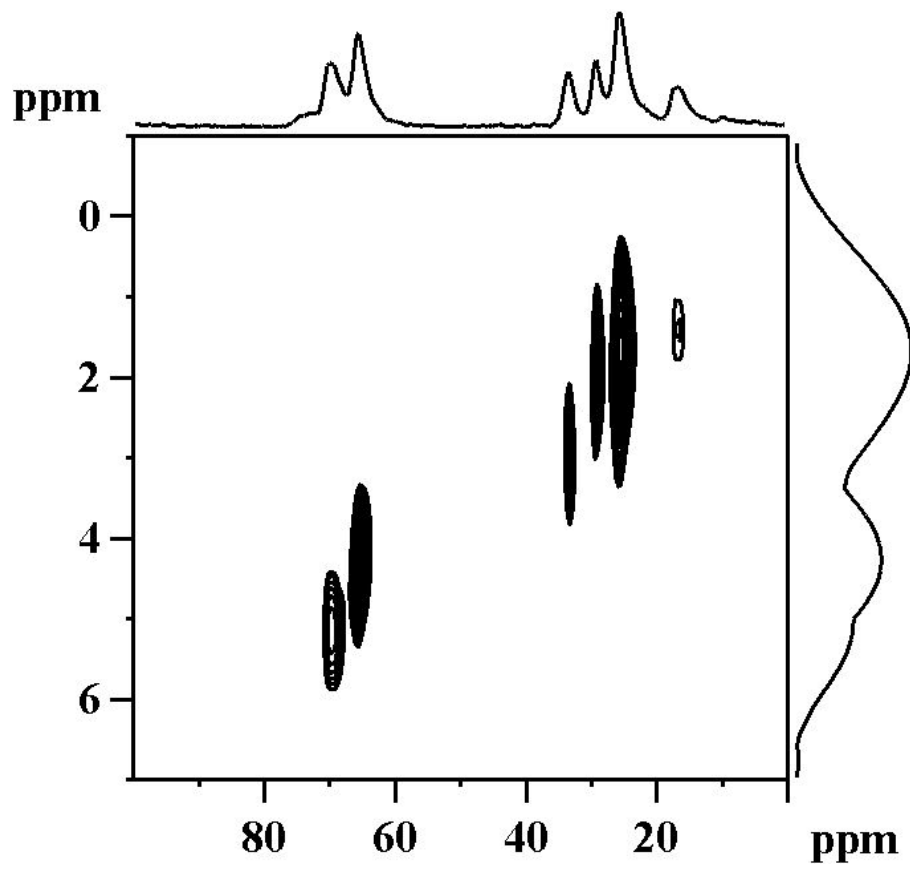
as expected based on the results of Figure 32, the ^1H lineshapes are broad in the second dimension for this amorphous system. Extraction of ^1H slices as a function of mixing time at the PLLA CH_3 (19 ppm) and the PCL OCH_2 (65 ppm) ^{13}C peaks provided the necessary time-dependent data for quantitative spin-diffusion analysis.



B.



C.



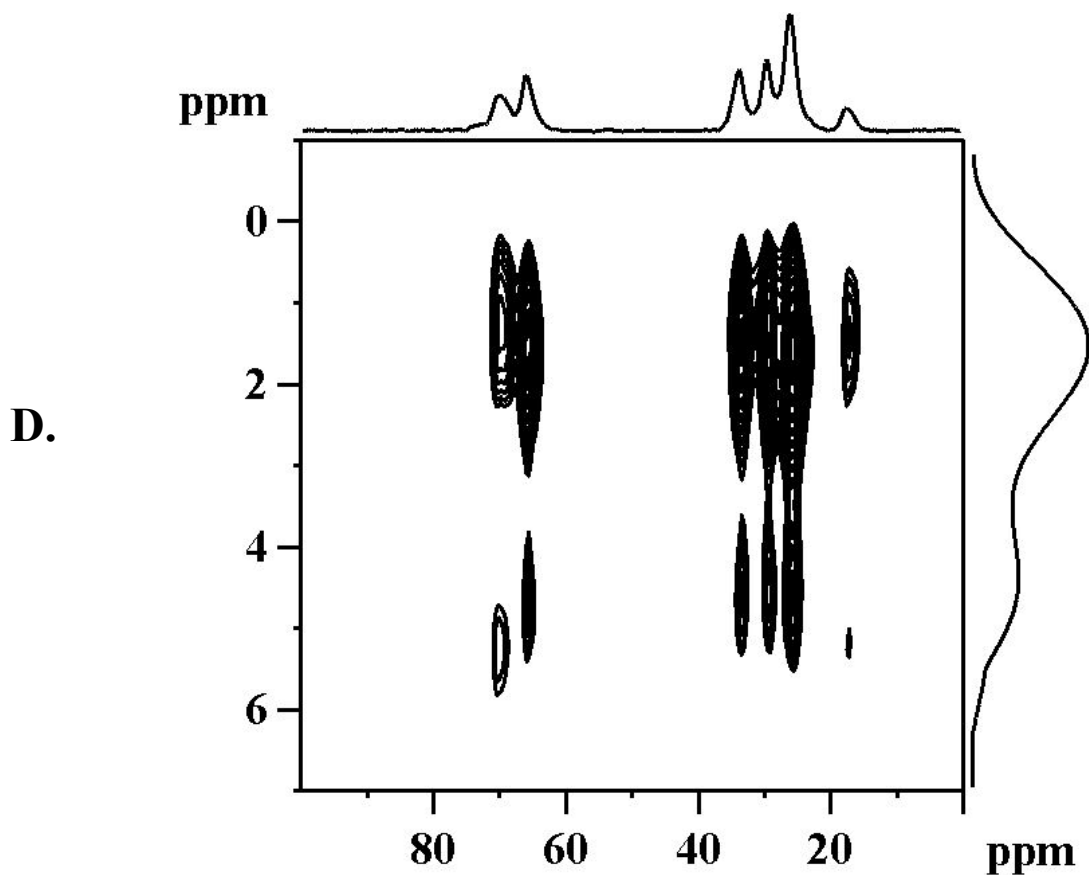


Figure 33. Representative two-dimensional ^1H - ^{13}C solid-state HetCor plots of the aliphatic ^{13}C region for: **(a)** FSLG/LGCP acquisition on the solvent-cast blend with no spin-diffusion time; **(b)** same as (a), after 1 ms spin-diffusion time; **(c)** MP/WIM acquisition on the coalesced blend with no spin-diffusion time; **(d)** same as (c), after 1 ms mixing time. ^1H slices were extracted at 19 ppm and 65 ppm for the spin-diffusion analysis. Summed projections from each dimension are shown along the ^{13}C (horizontal) and ^1H (vertical) axes.

Quantitative analysis of the ^1H slices extracted from the HetCor data represented by Figure 33 over the full range of spin-diffusion times produced the spin-diffusion curves shown in Figure 34 for the coalesced versus the solvent-cast PCL/PLLA blends. Again, the method for slice extraction and deconvolution has been previously discussed in detail⁹⁴. The intensity ratio plotted on the ordinate of Figure 34 is simply the fraction of

the OCH_x region (4-6 ppm) intensity relative to the total intensity in the ^1H slice at the PLLA CH_3 peak position (19 ppm) in the ^{13}C dimension.

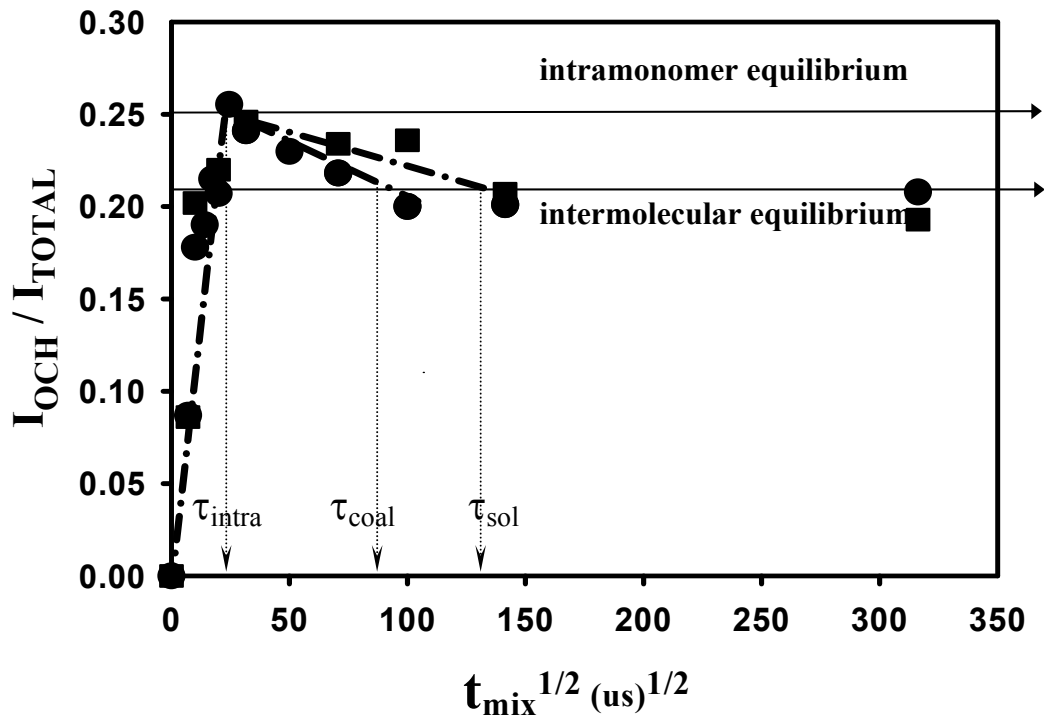


Figure 34. ^1H Spin-diffusion curves extracted from slices at the PLLA CH_3 signal (19 ppm) for the solution-cast (\blacksquare) and coalesced (\bullet) PCL/PLLA blends. The horizontal arrows indicate the predicted equilibrium intensity ratios for intramonomer vs. intermolecular (interdomain) spin-diffusion based on the monomer structures. The dashed line in the short time regime is the regression through the first five points of the curve to the intramonomer equilibrium intensity ratio (0.25). From this latter analysis, the equilibration time for intramonomer spin-diffusion was $20 \mu\text{s}^{1/2}$ (τ_{intra} vertical arrow). Additional vertical arrows indicate the equilibration times for intermolecular or interdomain spin-diffusion between PLLA and PCL in the coalesced ($\tau_{\text{coal}} = 88 \mu\text{s}^{1/2}$) and solution-cast ($\tau_{\text{sol}} = 132 \mu\text{s}^{1/2}$) blends, obtained by regression of the four experimental points between the intramonomer and intermolecular plateaus.

From the data shown in Figure 34, we see that the experimental results for the intensity distribution in the ^1H slice follow our expectation based on the monomer structures. More importantly, a well-defined intramolecular spin-diffusion equilibrium point is observed, the absolute intensity ratio for which (0.25) is larger than that for complete polarization redistribution among both polymers in the blend (0.21). Referring back to the structures and spectra in Figure 32, we observe that the extraction of ^1H slices at the PLLA CH_3 ^{13}C peak as a function of spin-diffusion time is tantamount to following the propagation of methyl proton polarization first within the PLLA monomer (intramolecular equilibrium), and then to neighboring chains (intermolecular equilibrium). Ultimately, that magnetization is distributed, and mixed, between both PCL and PLLA protons according to the stoichiometric values from the monomer structures and the overall blend composition. As such, at final equilibrium the ^1H slice has two broad peaks reflecting the combined ester (3 protons contributing to the 3.5-5.5 ppm region) and aliphatic hydrogens (11 protons contributing to the 1-3.5 ppm). In summation, the intensity from 3 ester protons relative to the total 14 protons in the system gives the 0.21 value for intermolecular equilibration, as expected for the equimolar blend compositions.

Initial rate analysis of the first five data points in Figure 34 with respect to the intramolecular equilibrium ratio yields a value for the PLLA intramolecular time (τ_{intra})^{1/2} = 20 $\mu\text{s}^{1/2}$. This spin-diffusion time, along with the characteristic monomer dimension x from the structure simulation (see Experimental), can be used to determine the spin-diffusion \mathbf{D} coefficient via solution of the diffusion equation $\mathbf{D} = (\pi x^2) / (4\tau_{\text{intra}})^{127}$. From this, we determine $\mathbf{D} = 1.1 \times 10^{-12} \text{ cm}^2 \text{ s}^{-1}$ for PLLA *in the coalesced blend* ($\mathbf{D}_{\text{PLLA}}^{\text{coal}}$).

An important point to note is that this spin-diffusion coefficient $D_{\text{PLLA}}^{\text{coal}}$ was determined by direct measurement on PLLA in the environment of interest, did not require reference to any other measurement technique or reference polymer, and may not be equal to the D value for pure PLLA (vide infra). As we have previously discussed, the intramolecular model for any given polymer defines a quantitative upper limit on the value of D ⁹⁴.

Figure 34 shows that intermolecular polarization transfer reaches the equilibrium condition much faster for the coalesced blend compared to the solution blend ($\tau_{\text{coal}}^{1/2} = 88 \mu\text{s}^{1/2}$ vs. $\tau_{\text{sol}}^{1/2} = 132 \mu\text{s}^{1/2}$, respectively), proving that the average distance between PLLA-rich and PCL-rich regions is significantly smaller in the blends prepared by coalescence from the cyclodextrin inclusion compound. From figure 34, and using a modified form of the diffusion equation appropriate for a binary mixture⁶¹, we calculate that the average length scale of mixing x in the coalesced PCL/PLLA blend is 4.9 nm, while in the amorphous regions of the solution-cast blend this dimension is 7.4 nm. The expected radii of gyration for the PLLA and PCL molecular weights used here (3.5- 5.0 nm) are comparable with the length scale of mixing calculated for the coalesced blend. On the other hand, the 7.5 nm length scale for the amorphous regions of the solution-cast blend significantly exceeds the radii of gyration of both polymers. While the mixing of PCL and PLLA is truly at molecular level in the coalesced blend, additional phase segregation appears to occur between PCL and PLLA chains in the amorphous regions of the solution-cast blend. As expected, all dimensions are significantly smaller than the calculated upper limit from the average $T_{1H} = 1$ s value (55 nm).

Change in spin-diffusion coefficient D after blending.

One aspect of the 2D HetCor spin-diffusion method is the ability to determine spin-diffusion coefficients for the polymer in the blend, and compare them to the values for the pure polymer prior to blending. By comparison, this would be analogous in theory to the measurement of T_g 's on a polymer in its pure vs. mixed state. The spin-diffusion coefficient should reflect changes in molecular dynamics of the polymer after blending. Figure 35 shows that the time required to reach intramolecular polarization equilibration is shorter in pure, bulk PLLA than it is for PLLA in the coalesced blend with PCL ($15.5 \mu\text{s}^{1/2}$ vs. $20 \mu\text{s}^{1/2}$, respectively). These values translate into spin-diffusion coefficients for the pure and mixed PLLA reflective of the expected increased chain mobility (and decreased D value) of PLLA when it forms an intimate mixture with the much lower glass transition PCL; we obtain $D_{\text{PLLA}}^{\text{pure}} = 2.1 \times 10^{-12} \text{ cm}^2 \text{ s}^{-1}$ and $D_{\text{PLLA}}^{\text{coal}} = 1.1 \times 10^{-12} \text{ cm}^2 \text{ s}^{-1}$. This reduction in D is consistent with x-ray diffraction data, which shows that almost all PLLA crystallinity is lost in the coalesced blend.

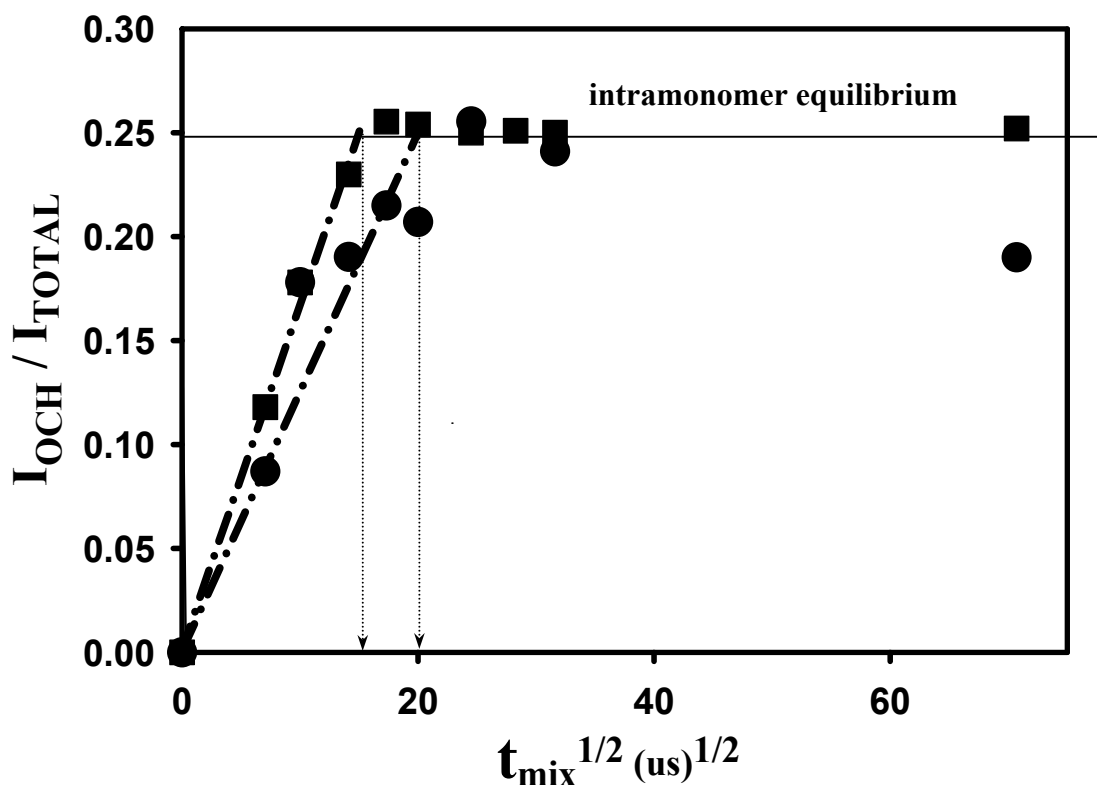


Figure 35. ^1H Spin-diffusion curve from pure PLLA (■) vs. PLLA in the coalesced blend with PCL(●), demonstrating a decrease in the spin-diffusion coefficient D upon blending. The last data point for the PLLA/PCL coalesced blend is already at the intermolecular equilibrium value, as previously seen in Figure 32.

The value of $D_{\text{PLLA}}^{\text{pure}} = 2.1 \times 10^{-12} \text{ cm}^2 \text{ s}^{-1}$ is in agreement with our previous determinations of D 's based on intramonomer spin-diffusion^{94,128}. For the higher- T_g polycarbonate ($T_g = 140 \text{ }^\circ \text{C}$) and lower- T_g polyisobutylene ($T_g = -70 \text{ }^\circ \text{C}$), the previously reported spin-diffusion coefficients were $5.1 \times 10^{-12} \text{ cm}^2 \text{ s}^{-1}$ and $4.4 \times 10^{-14} \text{ cm}^2 \text{ s}^{-1}$, respectively. Since the PLLA T_g is intermediate between these two extreme ($T_g = 60 \text{ }^\circ \text{C}$), an intermediate value of D expected.

Bioexponential fit for coalesced PCL/PLLA sample.

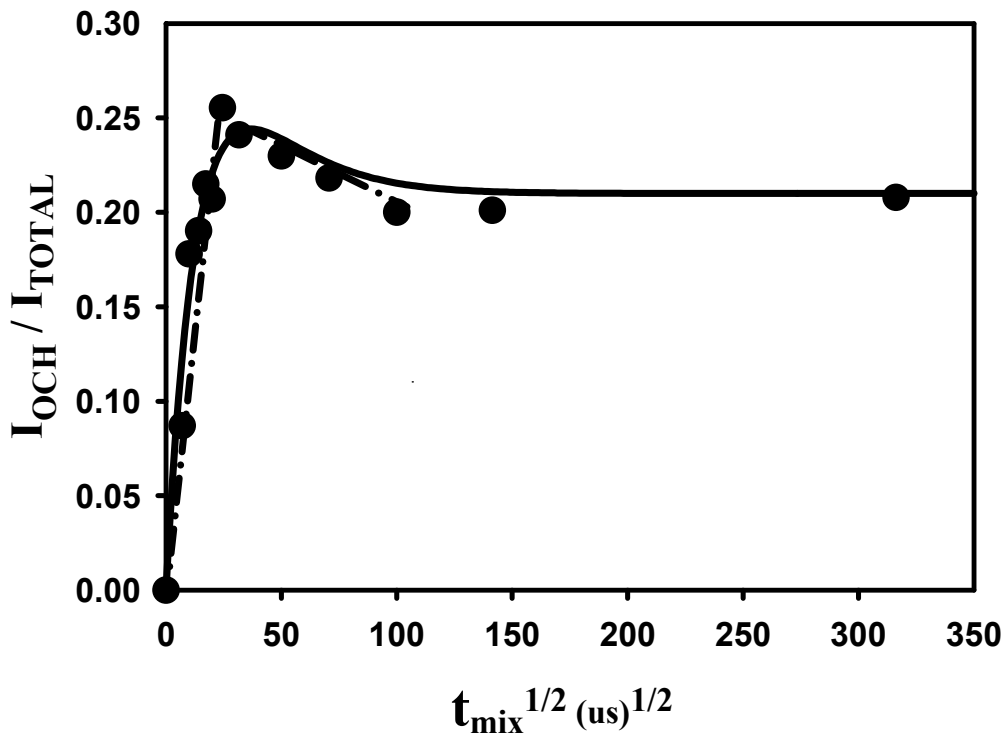


Figure 36. Biexponential fit for ^1H spin-diffusion curves extracted from slices at the PLLA CH_3 signal (19 ppm) for the coalesced (●) PCL/PLLA blends at figure 32. The biexponential equation is $f = a*(1-\exp(-b*x)) + c*(1-\exp(-d*x))$, the parameters are as following: $a = 2.4302$, $b = 0.0547$, $c = -2.2202$, $d = 0.0495$ $R^2 = 0.948$. The solid line is the two-component fit, with the short time response attributed to intramolecular polarization equilibration, and the long time component to interdomain spin-diffusion.

Figure 36 is a biexponential fit for ^1H spin-diffusion curves extracted from slices at the PLLA CH_3 signal (19 ppm) for the coalesced PCL/PLLA blends at figure 32. The parameters are as following: $a = 2.4302$, $b = 0.0547$, $c = -2.2202$, $d = 0.0495$. The $R^2 = 0.948$. The purpose of this figure is to demonstrate that the linear least squares analysis of the short-time data (to determine the intramolecular equilibrium time) plus descending intensities to the intermolecular equilibrium is an accurate representation of the total data.

Relative sensitivity for trace components.

In figure 32e, the PLLA OCH peak (peak **f** at 69 ppm) appears to broaden, and a downfield shoulder is evident at 72 ppm. Initially, we considered that this change in peak shape for the coalesced blend, which was not observed in the solution blend spectrum of Figure 32d, might arise from some specific chemical interaction between the methine group of PLLA and carbonyl groups on PCL. However, close inspection of this region of the 2D HetCor plot, obtained without any spin-diffusion time, reveals that this weak shoulder in the CP spectrum is a unique chemical moiety, based on its correlation to a new, unique ^1H chemical shift. No other carbon peaks in the spectrum share this ^1H shift.

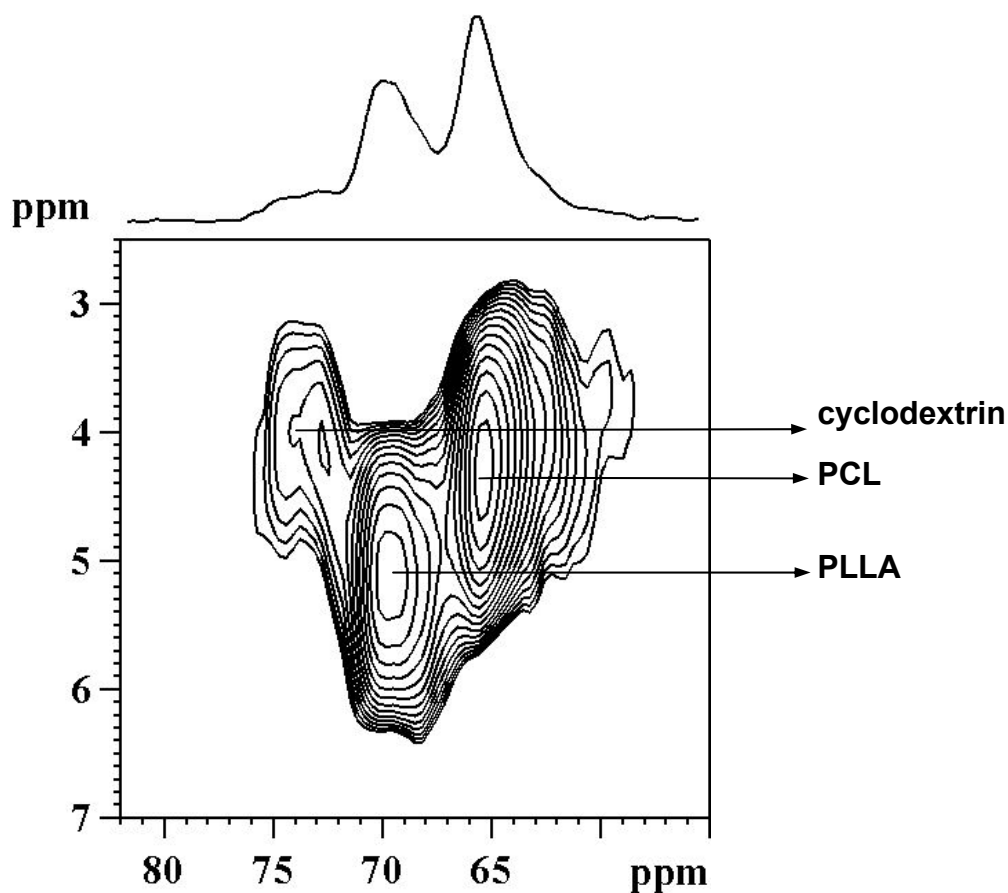


Figure 37. Expanded HetCor plot of the OCH and OCH₂ region of the spectrum showing that the broad downfield (in the ¹³C dimension) shoulder off the PLLA peak is clearly correlated to an upfield ¹H shift.

Control experiments on pure cyclodextrin indicate that this “new” peak in the coalesced blend is simply the peak from trace amounts of α -cyclodextrin that were not completely removed by the DMSO-washing step. However, its detection does raise an interesting point. Quantitative analysis of the coalesced blend using single-pulse ¹³C excitation reveals that the amount of α -cyclodextrin remaining in the blend is only 2-3 mole %, and yet we are able to see a strong, well-resolved correlation even in this crowded spectral region. The detection limit for a rigid structure like α -cyclodextrin is obviously lower than that for a highly mobile trace component. Nonetheless, the HetCor

approach, which is often ignored in materials analysis due to its perceived low sensitivity, provides the necessary data to clarify the questions arising from the one-dimensional CP/MAS data in Figure 32.

4. Conclusions

Two-dimensional spin-diffusion HetCor experiments revealed that more intimately mixed blends of PCL and PLLA could be prepared using inclusion compound coalescence techniques, relative to standard solution blending. The average minimum dimension for the amorphous coalesced PCL/PLLA blend was 4.9 nm, while the amorphous PCL/PLLA blend prepared by dissolution in dioxane was 7.4 nm. The former dimension is comparable to the 4-5 nm radii of gyration of the particular PLLA and PCL polymers used, indicative of molecular level mixing in the coalesced blend. Individual spin-diffusion coefficients for PLLA and PCL chains *in the blends* were calculated based on direct experimental measurement of the polymers in the blend. The magnitude of D was found to decrease by a factor of two for PLLA chains in the coalesced blend compared to the pure polymer. The extension of our previously published experimental strategy to these important biocompatible and biodegradable polyester blends demonstrates its general utility for characterizing multicomponent amorphous materials.

Chapter 5. Conclusions and Future Directions

This dissertation demonstrated the utility of the solid-state spin diffusion 2D HetCor methods on the study of solid amorphous polymers. The rate of intrapolymer and interchain polarization transfer can be easily differentiated by this method. It is successfully applied to pure amorphous polymers, PC, PPO, diblock copolymer, PS-*b*-PMMA, as well as inclusion compounds and its coalesced product PCL-PLLA. This solid-state spin diffusion NMR method can achieve the measurement of spin diffusion coefficient for the amorphous polymers, and probe its changes when they form blends, copolymers or composites with no requirements of isotopic labeling, a neutron source, or any special sample preparation treatments. It provides a new attractive strategy for the determination of polymers' structures and interrogation of their miscibility. It solved the problem that X-ray scattering method can not determine the structure of amorphous polymers.

References:

1. Spiess, H. W. NMR Methods For Solid Polymers *Annu. Rev. Sci.* **1991**, 21, 131
2. Yu, Tongyin, Guo, Mingming *Prog. Polym. Sci.* **1990**, 15, 825
3. Frydman, Lucio *Annu. Rev. Phys. Chem.* **2001**, 52, 463
4. Schmidt-Rohr, K.; Spiess, H.W. *Multidimensional Solid-State NMR and Polymers*; Academic Press, New York, **1994**, Chapter 1
5. Melinda, J. *Duer Solid-State NMR Spectroscopy Principles and Applications* Blackwell Science Ltd, **2002**, Part 1
6. Pethrick, R. A., Viney, C. *Techniques for Polymer Organization and Morphology Characterization*, John Wiley & Sons, Chichester, **2003**
7. Pethrick, R. A., Dawkins, J. V. *Modern Techniques for Polymer Characterization*, John Wiley & Sons, Chichester, **1999**
8. Siesler, H. W., in *Structure – Property Relations in Polymers*, Ed. Urban, M.W., Craver, C.D., *Advances in Chemistry Series 236*, American Chemical Society, Washington, DC, **1993**,3
9. Mandelkern, L., Alamo, R.G., in *Structure – Property Relations in Polymers*, Ed. Urban M.W., Craver, C.D., *Advances in Chemistry Series 236*, American Chemical Society, Washington, DC, **1993**,157
10. Campbell, D., Pethrick, R.A., White, J.R. *Polymer Characterization – Physical Techniques*, **2000**, Chapter 8, 194
11. Hall, I.H., in *Structure of Crystalline Polymers*, Ed. Hall, I.H., Elsevier Applied Science, London and New York, **1984**, Chapter 2,39
12. Herglotz, in *Structure of Crystalline Polymers*, Ed. Hall, I.H., Elsevier Applied Science, London and New York, **1984**, Chapter 6, 229

13. Cullity, B.D., *Elements of X-ray Diffusion*, Addison-Wesley, Reading, MA, **1978**
14. Nguyen L.T., *New Characterization Techniques for Thin Polymer Films*, Ed. Tong, H.M., Nguyen, L.T., Wiley, New York, **1990**, 57
15. Sadler, D.M., in *Structure of Crystalline Polymers*, Ed. Hall, I.H., Elsevier Applied Science, London and New York, **1984**, Chapter 4, 125
16. Lovesay, S.W., *Theory of Neutron Scattering from Condensed Matter*, Vol. 1, Oxford University Press, Oxford, **1984**
17. Higgins, J.S., Benoit, H.C., *Polymers and Neutron Scattering*, Oxford Science Publications, Oxford, **1994**
18. Jones, R.A.L., Richards, R.W., *Polymers at Surfaces and Interfaces*, Cambridge University Press, Cambridge, **1999**, 94
19. Campbell, D., Pethrick, R.A., White, J.R., *Polymer Characterization Physical Techniques*, Stanley Thornes, Cheltenham, **2000**, Chapter 9
20. Williams, D.B., *Practical Analytical Electron Microscopy in Materials Sciences*, Verlag Chemie International, Weinheim, **1984**
21. Campbell, D., Pethrick, R.A., White, J.R., *Polymer Characterization Physical Techniques*, Stanley Thornes, Cheltenham, **2000**, Chapter 10
22. Reneker, D.H., *New Characterization Techniques for Thin Polymer Films*, Ed. Tong, H.M., Nguyen, L.T., Wiley, New York, **1990**, 327
23. Sanders, J.K.M.; Hunter, B.K. *Modern NMR Spectroscopy: A Guide for Chemists*, Oxford University Press, **1993**
24. Harris, R.K. *Nuclear Magnetic Resonance Spectroscopy: A physicochemical View* Longman Scientific & Technical, **1986**
25. VanderHart, D. L.; McFadden, G. M. *Solid State NMR* **1996**, 7, 45.

26. Schmidt-Rohr, K.; Spiess, H. W. *Multidimensional Solid-State NMR and Polymers*, **1994**, Academic Press, New York; Chapter 13.
27. Mattson, J., Simon, M. *The pioneers of NMR and Magnetic Resonance in Medicine: The Story of MRI*, Jericho: Dean Books Co, **1996**
28. Jonas, J., Gutowsky, H.S., NMR in Chemistry- An Evergreen, *Ann. Rev. Phy. Chem.*, **1980**, 31,1-27
29. Stejskal, E.O, Memory, J.D., *High resolution NMR in the solid state : fundamentals of CP/MAS*, Oxford University Press, New York,**1994**
30. Freeman, Ray, *Spin Choreography: Basic Steps in High Resolution NMR*, Spektrum Academic Publishers, University Science Books, Oxford,**1997**
31. Homans, S.W. *A dictionary of Concepts in NMR*, Clarendon Press, Oxford, **1989**
32. Fitzgerald, J.J., *Solid-State NMR Spectroscopy of Inorganic Materials*, ACS Symposium Series 717, Washington, DC, **1999**
33. Andrew, E.R., Bradbury, A. and Eades, R.G. *Nature*, London, **1961**, 182, 1659
34. Schaefer, J. and E. O. Stejskal *J. Am. Chem. Soc.*, **1976**, 98, 1031
35. Mehring, M. *Principles of High Resolution NMR in Solids*; Springer- Verlag, Berlin, **1983**
36. Muller, L., Kumar, A. and Ernst, R.R. *J. Chem. Phys.*, **1975**, 63, 5490
37. Aue, W.P., Bartholdi, E. and Ernst, R.R. *J. Chem. Phys.*, **1976**, 64, 2229
38. Ernst, R.R., bodenhausen, G. and Wokaun, A. *Principles of Nuclear Magnetic Resonance in One and Two Dimensions*, Clarendon Press, Oxford, **1987**
39. Waugh, J.S., Huber, L.M., Haeberlen, U., *Phys. Rev. Lett.*, **1968**, 20, 3740
40. Mansfield, P., *J. Phys. Chem.*, **1971**, 4, 1444
41. Rhim, W.K., Elleman, D. D., Vaughan, R.W., *J. Chem. Phys.*, **1973**, 59, 3740
42. Burum, D.P., Linder, M., Ernst, R.R., *J. Magn. Reson.*, **1981**, 44, 173

43. Burum, D.P., Bielecki, A., *J. Magn. Reson.*, **1991**, 94, 645
44. Hartmann, S.R. and Hahn, E.L. *Phys. Rev.*, **1962**, 128, 2042
45. Solomon, I. *Phys. Rev.* **1955**, 99, 559
46. Bloembergen, M., Purcell, E.M., Pound, R.V., *Phys. Rev.*, **1948**, 73, 679
47. Kubo, R. Tomita, K., *Phys. Soc. Japan*, **1954**, 9, 888
48. Redfield, A.G., *Adv. Mag. Reson.*, **1965**, 1, 1
49. Jones, G.P., *Phys. Rev.*, **1966**, 148, 332
50. Ailion, D.C., *Adv. Magn. Reson.*, **1971**, 5, 177
51. Stejskal, E.O., Tanner, J.E., *J. Chem. Phys.* **1965**, 42, 288
52. Herzfeld, J. Berger, A.E., *J. Chem. Phys.*, **1979**, 70, 3300
53. Dixon, W.T., *J. Chem. Phys.*, **1980**, 73, 6021
54. Antzutkin, O.N., Song, Z., Feng, X., Levitt, M.H., *J. Chem. Phys.*, **1994**, 100, 130
55. Haeberlen, U., Waugh, J.S., *Phys. Rev.*, **1968**, 175, 453
56. Rhim, W.-K., Elleman, D.D., Vaughan, R.W., *J. Chem. Phys.*, **1973**, 59, 3740
57. Burum, D.P., Rhim, W.-K., *J. Chem. Phys.*, **1979**, 71, 944
58. Peersen, O.B., Wu, X., Kustanovich, I., Smith, S.O., *J. Magn. Reson.*, **1993**,
A104, 334
59. Metz, G., Wu, X., Smith, S.O., *J. Magn. Reson.*, **1994**, A110, 219
60. Stejskal, E.O., Schaefer, J., Waugh, J.S., *J. Magn. Reson.*, **1977**, 28, 105
61. Clauss, J.; Schmidt-Rohr, K.; Spiess, H.W. *Acta Polym.* **1993**, 44, 1
62. Cheung, T.; Gerstein, B. *J. Appl. Phys.* **1981**, 52, 5517
63. Spiegel, S.; Schmidt-Rohr, K.; blumich, B.; Domke, W.D.; Stapp, B. *J. Appl.*
Polym. Sci. **1992**, 44, 289
64. Bloembergen, N. *On the interaction of Nuclear Spins, Physica, XV*, **1949**, 386
65. Zhang, S., Meier, B.H. and Ernst, R.R. *Phys. Rev. Lett.*, **1992**, 69, 2149

66. Goldman, M. and Shen, L. *Phys. Rev.*, **1996**, 144, 321
67. Caravatti, P., Neuenschwander, P., Ernst, R.R., *Macromolecules*, **1985**, 18, 119
68. Schmidt-Rohr, K., Clauss, J., Spiess, H.W., *Magn. Reson. Chem.*, **1990**, 28, 3
69. Kenwright, A.M., Say, B.J., *solid-State NMR*, **1996**, 7,85
70. Packer, K.J., Poplett, I.J.F., Taylor, M.J., *J. Chem. Soc. Faraday Tran. 1*, **1988**, 84, 3581
71. Geppi, M., Harris, R.K., Kenwright, A.M., Say, B.J., *Solid-State NMR*, **1998**, 12, 15
72. Egger, N.; Schmidt-Rohr, K. S.; Blumich, B.; Domke, W. D.; Stapp, B. *J. Appl. Polym. Sci.* **1992**, 44, 289.
73. Gentzler, M.; Reimer, J. A. *Macromolecules* **1997**, 30, 8365.
74. Mulder, F. M.; Heinen, W.; van Duin, M.; Lugtenburg, J.; de Groot, H. J. M. *J. Am. Chem. Soc.* **1998**, 120, 12891.
75. da Silva, N. M.; Tavaneres, M. I. B.; Stejskal, E. O. *Macromolecules* **2000**, 33, 115.
76. Wu, R. R.; Kao, H. M.; Chiang, J. C.; Woo, E. M. *Polymer* **2002**, 43, 171.
77. Mirau, P. A., S. Yung *Chem. Mater.* **2002**, 14, 249.
78. VanderHart, D. L.; McFadden, G. M. *Solid State NMR* **1996**, 7, 45.
79. Kaplan, S. *Macromolecules* **1993**, 26, 1060
80. White, J.L.; Mirau, P.A. *Macromolecules* **1994**, 27, 1648
81. Li, S.; Rice, D.M.; Karasz, F.E. *Macromolecules* **1994**, 27, 2211
82. Bielecki, A., Burum, D.P., Rice, D.M., Karasz, F.E., *Macromolecules*, **1991**, 24, 4820
83. Caravatti, P., Bodenhausen, G., Ernst, R.R., *Chem. Phys. Lett.* **1982**, 89, 363
84. Caravatti, P., Braunschweiler, L., Ernst, R.R., *Chem. Phys. Lett.* **1983**, 100, 305

85. Blumich, B., Spiess, H.W., *Angew. Chem. Int. Ed. Engl.*, **1988**, 27, 1655
86. Schmidt-Rohr, K., Clauss, J., Blumich, B., Spiess, H.W., *Polym. Prepr. (Am. Chem. Soc. Div. Polym. Chem.)*, **1990**, 31, 1, 172
87. Liu, Y.; Inglefield, P. T.; Jones, A. A. *Magn. Reson. Chem.* **1994**, 32, S18.
88. Schmidt-Rohr, K.; Clauss, J.; Spiess, H.W. *Macromolecules* **1992**, 25, 3273
89. VanderHart, D.L.; McFadden, G.M. *Solid State NMR* **1996**, 7, 45
90. Brus, J.; Dybal, J.; Schmidt, P.; Kratochvil, J.; Baldrian, J. *Macromolecules* **2000**, 33, 6448
91. White, J.L.; Dias, A.J.; Ashbaugh, J.R. *Macromolecules* **1998**, 31, 1880
92. Assink, R. A. *Macromolecules* **1978**, 11, 1233.
93. VanderHart, D. L. *Macromol. Chem., Macromol. Symp.* **1990**, 38, 125
94. Jia, X.; Wolak, J.; Wang, X.; White, J. L. *Macromolecules* **2003**, 36, 712-718.
95. Lee, M., Goldberg, W.I., *Phy. Rev.*, **1965**, 140, A1261
96. Sozzani, P., Bracco, S., Comotti, A., Simonutti, R., Camurati, I., *J. Am. Chem. Soc.*, **2003**, 125, 12881
97. Umetsu, M., Hollander, J.G., Matysik, J., Wang, Z.Y., Adschiri, T., Nozawa, T., de Groot, H.J.M., *J. Phys. Chem.*, **2004**, 108, 2726
98. Hong, M., Yao, X., Jakes, K., Huster, D., *J. Phys. Chem. B*, **2002**, 106, 7355
99. Fu, R., Hu, J., Cross, T.A., *J. Magn. Reson.*, **2004**, 168, 8
100. Van Rossum, B.J., Castellani, F., Rehbein, K., Pauli, J., Oschkinat, H., *Chembiochem*, **2001**, 2, 906
101. Lesage, A., Sakellariou, D., Steuernagel, S., Emsley, L., *J. Am. Chem. Soc.*, **1998**, 120, 13194
102. van Rossum, B.J., Forster, H., de Groot H.J.M., *J. Magn. Reson.*, **1997**, 124, 516

103. van Rossum, B.J., de Groot, C.P., Ladizhansky, V., Vega, S., de Groot, H.J.M.,
J. Am. Chem. Soc., **2000**, 122, 3465
104. Lesage, A., Emsley, L., *J. Magn. Reson.*, **2001**, 148, 449
105. Schmidt-Rohr, K., Hong, M., *J. Am. Chem. Soc.*, **2003**, 125, 5648
106. Lesage, A., Charmont, P., Steuernagel, S., Emsley, L., *J. Am. Chem. Soc.*, **2000**,
122, 9739
107. Fu, R., Tian, C., Cross, T.A., *J. Magn. Reson.*, **2002**, 154, 130
108. van Rossum, B.J., Schulten, E.A.M., Raap, J., Oschkinat, H., de Groot, H.J.M.,
J. Magn. Reson., **2002**, 155, 1
109. Ladizhansky, V., Vega, S., *J. Chem. Phys.*, **2000**, 112, 7158
110. Yao, X.L., Schmidt-Rohr, K., Hong, M., *J. Magn. Reson.*, **2001**, 149, 139
111. van Rossum, B.J., Boender, G.J., de Groot, H.J.M., *J. Magn. Reson.*, **1996**, 120,
274
112. Alia, Matysik, J., de Boer, I., Gast, P., van Gorkom, H.J., de Groot, H.J.M., *J.*
Biomol. NMR, **2004**, 28, 157
113. Varshney, S.K., Fayt, R., Teyssle, P., Hautekeer, J.P., *US Patent*, **1993**,
5,284,527
114. Teyssle, P., Bayard, P., Jarome, R., Varshney, S.K., Wang, J.S., 36th IUPAC
international Union of Pure & Applied Chemistry International Symposium on
Macromolecules, **1994**, 87
115. Varshney, S.K., Hautekeer, J.P., Feyt, R., Jerome, R., Teyssle, P.,
Macromolecules, **1990**, 23, 2618
116. Jerome, R., Forte, R., Varshney, S.K., Fayt, R., Teyssle, P., *NATO ASI Series*,
C215, 101 (**1987**), CA Vol. 108, 12, 094992

117. Bovey, F. A., Mirau, P. A. *NMR of Polymers*, **1996**, Academic Press, San Diego, CA, Chapter 4.
118. The $T_1(H)$ values for the PS and PMMA are equivalent for the 50K diblock (800 ms), but begin to diverge for the 100K (PS = 925 ms and PMMA = 710 ms), and are significantly different for the 200K sample (PS = 1050 ms and PMMA = 690 ms). These disparate T_1 's contribute to the long-time divergence from intermolecular equilibration for the 200K copolymer, as the proton reservoir becomes preferentially depleted in PMMA aliphatic polarization.
119. Wang, J.; Jack, K. S., Natansohn, A. L. *J. Chem. Phys.*, **1997**, 107, 1016.
120. Rusa, C. C.; Shuai, X.; Shin, I. D.; Bullions, T. A.; Wei, M.; Porbeni, F. E.; Lu, J.; Huang, L.; Fox, J.; Tonelli, A. E. *Journal of Polymers and the Environment* **2004**, 12(3), 157
121. Rusa, C.C., Tonelli, A.E., *Macromolecules*, **2000**, 33, 5321
122. Rusa, C.C., Fox, J., Tonelli, A.E., *Macromolecules*, **2003**, 36, 2742
123. Wei, M., Tonelli, A.E., *Macromolecules*, **2001**, 34, 4061
124. Wei, M., Shuai, X., Tonnelli, A.E., *Biomacromolecules*, **2003**, 4, 783
125. Shuai, Xintao; Porbeni, Francis E.; Wei, Min; Shin, I. Daniel; Tonelli, Alan E. *Macromolecules*, **2001**, 34(21), 7355
126. Clauss, J., Schmidt-Rohr, K., Spiess, H.W., *Acta. Polymer.*, **1993**, 44, 1
127. Mellinger, F., Wilhelm, M., Spiess, H.W., *Macromolecules*, **1999**, 32, 4686
128. Wang, X., White, J.L., *Macromolecules*, **2002**, 35, 3795
129. Hlatkey, G.G., *Chem. Rev.*, **2000**, 100, 1347
130. Single-Site Catalysts, *Chem. Eng. News*, **2000**(Aug 7), 78, 35
131. Yamaguchi, M., Miyata, H., *Macromolecules*, **1999**, 32, 5911
132. White, J.L., Lohse, D.J., *Macromolecules*, **1999**, 32, 958

133. Krishnamoorti, R., Graessley, W.W., Fetters, L.J., Garner, R.T., Lohse, D.J.,
Macromolecules, **1995**, 28, 1252
134. Bronniman, C. E., Ridenour, C. F., Maciel, G. E., *J. Magn. Reson.*, **1992**, 97,
522
135. Smith, B. L., Schaffer, T. E., Viani, M., Thompson, J. B., Frederick, N. A.,
Kindt, J., Belcher, A., Stucky, G.D., Morse, D. E., Hansma, P. K., *Nature*, **1999**,
399, 761
136. John, J., Mani, R., Bhattacharya, M., *J. Polym. Sci. Polym. Chem.*, **2002**, 40,
2003
137. Ando, I., Asakura, T., *Solid State NMR of Polymers*, **1998**, Elsevier,
Amsterdam, Netherlands
138. Choi, N. S., Kim, C. H., Cho, K. Y., Park, J. K., *J. Appl. Polym. Sci.*, **2002**, 86,
1892
139. Jeon, O., Lee, S. H., Kim, S. H., Lee, Y. M., Kim, Y. H., *Macromolecules*,
2003, 36, 5585
140. Wagler, T., Rinaldi, P. L., Han, C. D., Chun, H., *Macromolecules*, **2000**, 33,
1778
141. Egger, N., Schmidt-Rohr, K.S., Blumich, B., Domke, W. D., Stapp, B., *J. Appl.*
Polym. Sci., **1992**, 44, 289
142. Mirau, P. A., Yung, S., *Chem. Mater.*, **2002**, 14, 249

APPENDICES

MP-WIM Pulse Program used at Bruker Avance 300 MHz instrument.

```
;jwcphtcor_sd.rel
;solids Hetcor using BLEW-12 and BB-24 with non-delayed RF gating
;see: Burum and Bielecki, J.M.R, 94, 645, 1991

;set:
;p1 = 90 degree X and 1H pulse
;p12 to drive H-transmitter,
;p11 to drive X-transmitter
;l0 = 0
;l1 = 1-3
;ns = 16*n
;parmode = 2D
;td1 to 64 or 128 depending on the expected resolution
;l2=td1/2
;MC2= states-TPPI
;

"p20=(p1*63)/90"

#include <preamp.incl>
#include <powswi.incl>

1 ze
  1m do:f2
  10u p11:f1
  10u p12:f2
2 d1
  protect
  10u fq2:f2
  1u hgain2
  10u:f2 ph30
  (5u ph1):f2
  3 (p1 ph1):f2
  (1u ph2):f2
  ;set phase for decoupler channel
  ;90 degree 1H pulse
```

```

;-----BLEW-12 and BB-24

4 (p1 ph12):f1 (p1 ph14):f2
  (p1 ph13):f1 (p1 ph17):f2
  (p1 ph12):f1 (p1 ph16):f2
  (p1 ph10):f1 (p1 ph16):f2
  (p1 ph13):f1 (p1 ph15):f2
  (p1 ph12):f1 (p1 ph16):f2

  (p1 ph12):f1 (p1 ph14):f2
  (p1 ph13):f1 (p1 ph17):f2
  (p1 ph10):f1 (p1 ph14):f2
  (p1 ph12):f1 (p1 ph14):f2
  (p1 ph13):f1 (p1 ph15):f2
  (p1 ph12):f1 (p1 ph16):f2

  (p1 ph10):f1 (p1 ph14):f2
  (p1 ph11):f1 (p1 ph17):f2
  (p1 ph10):f1 (p1 ph16):f2
  (p1 ph12):f1 (p1 ph16):f2
  (p1 ph11):f1 (p1 ph15):f2
  (p1 ph10):f1 (p1 ph16):f2

  (p1 ph10):f1 (p1 ph14):f2
  (p1 ph11):f1 (p1 ph17):f2
  (p1 ph12):f1 (p1 ph14):f2
  (p1 ph10):f1 (p1 ph14):f2
  (p1 ph11):f1 (p1 ph15):f2
  (p1 ph10):f1 (p1 ph16):f2

lo to 4 times 10
;-----tilt and TPPI pulses

(p20 ph2):f2 ;63 degree pulse
lu:f2 ph0
(p1 ph3):f2 ;90 degree pulse for TPPI selection
d6 ;spin-diffusion time
(p1 ph3):f2 ;90 degree pulse for TPPI selection

;-----WIM-24:
5 (p1 ph27):f1 (p1 ph23):f2
  (p1 ph24):f1 (p1 ph20):f2
  (p1 ph27):f1 (p1 ph23):f2
  (p1 ph27):f1 (p1 ph23):f2
  (p1 ph24):f1 (p1 ph20):f2
  (p1 ph27):f1 (p1 ph23):f2

  (p1 ph25):f1 (p1 ph21):f2
  (p1 ph24):f1 (p1 ph20):f2
  (p1 ph25):f1 (p1 ph21):f2
  (p1 ph25):f1 (p1 ph21):f2
  (p1 ph24):f1 (p1 ph20):f2
  (p1 ph25):f1 (p1 ph21):f2

  (p1 ph27):f1 (p1 ph23):f2
  (p1 ph26):f1 (p1 ph22):f2
  (p1 ph27):f1 (p1 ph23):f2
  (p1 ph27):f1 (p1 ph23):f2
  (p1 ph26):f1 (p1 ph22):f2
  (p1 ph27):f1 (p1 ph23):f2

```

```

(p1 ph25):f1 (p1 ph21):f2
(p1 ph26):f1 (p1 ph22):f2
(p1 ph25):f1 (p1 ph21):f2
(p1 ph25):f1 (p1 ph21):f2
(p1 ph26):f1 (p1 ph22):f2
(p1 ph25):f1 (p1 ph21):f2

lo to 5 times l1
;-----

1u cw:f2
2u fq2:f2
1u pl12:f2
1u:f1 ph6
1u adc ph31
aq
1m
10u hgain1
rcyc=2
2m do:f2

100m wr #0 if #0
10m ip30
lo to 1 times 2
1m iu0
lo to 1 times 12

6 exit
ph0=0
ph1= +y +y -y -y ;alternation of initial proton 90
ph2= +x ;proton phase for CRAMPS part
ph3= +x -x +x -x ;alternation of TPPI proton 90
ph6= +x
ph10= +x
ph11= +y
ph12= -x
ph13= -y
ph14= +x
ph15= +y
ph16= -x
ph17= -y
ph20= +x
ph21= +y
ph22= -x
ph23= -y
ph24= +x +x +x +x +y +y +y +y -x -x -x -x -y -y -y -y
ph25= +y +y +y +y -x -x -x -x -y -y -y -y +x +x +x +x
ph26= -x -x -x -x -y -y -y -y +x +x +x +x +y +y +y +y
ph27= -y -y -y -y +x +x +x +x +y +y +y +y -x -x -x -x
ph30=0
ph31= 0 0 2 2 1 1 3 3 ;receiver phase
      2 2 0 0 3 3 1 1

```

FSLG-LGCP Pulse Program used at Bruker Avance 300 MHz instrument.

```

define loopcounter count
"count=td1"

"p11=(p3*547)/900"

1 ze
2 d1 do:f2
  1u:f2 ph0
  10u pl11:f1
  10u fq=cnst21:f2
  10u pl2:f2
  p3:f2 ph1 ;p3=pi/2 pulse
  0.5u
  (p11 ph11):f2 ; magic angle pulse, p11=(547/900)* p3
  0.6u fq=cnst22:f2 ;cnst22= 106 / (p3*4*squ-root2) +- 1000-5000
5 (p6 ph4):f2 ;FSLG period during t1/2,p6=(294/90)*p3- p13
  p13:f2 fq=cnst23:f2 ;p13=0.5-1 us, cnst23 =-106 / (p3*4*squ-root2)
  ; +- 1000-5000

  (p6 ph5):f2
  p13:f2 fq=cnst22:f2
  lo to 5 times 10
  1u fq=cnst21:f2 ;cnst21=0
; 1u pl1:f1
  (p12 ph7):f2 ;p12= 353/900*p3
; 0.5u
; (p3 ph8):f2
  d6 ;s.d. time
  (p11 ph9):f2
  1u fq=cnst24:f2 ;cnst24 FSLG frequency at contact time
; 1u
; (3u ph3):f2
  (p15:sp1 ph2):f1 (p15:sp0 ph3):f2 ;sp0=p11=pl11 from lgcp
  1u pl12:f2 fq=cnst21:f2 ; cross polarisation
; 1u pl12:f2 ; set power level for decoupling
  2u cpd2:f2
  1u:f1 ph30
  2u adc ph31
  aq
  1m do:f2
  rcyc=2
  30m wr #0 if #0 zd
  1m ip3
  1m ip9 ;TPPI
quadrature
15 1m iu0
  1m iu0
  lo to 15 times l1
  lo to 2 times count
exit

```

ph0=0
ph30=0
ph1=+y -y
ph2=+x +x -x -x +y +y -y -y
ph11=+y
ph3=+x
ph4=+x
ph5=-x
ph14=+x +x -x -x
ph7=+y
ph8=-y
ph9=-y
ph10=0
ph31=0 2 2 0 1 3 3 1

Preparation and Characterization of Poly (acetoxystyrene)/Poly (ethylene oxide) Blends

Motivation: We tried to make the blends, and use multidimensional solid-state NMR to investigate the weak CH...O hydrogen bonds between the carbonyl group of PAS and the methylene group of PEO.

Materials: PAS was synthesized by free radical polymerization in benzene at 80 degree under a nitrogen atmosphere using azobis(isobutyronitrile) (AIBN) initiator. Then it was purified by dissolving in benzene, reprecipitated from cyclohexane, and dried in a vacuum oven at 80 degree for overnight.

Preparations of PAS/PEO blends: THF was used to mix the two polymers.

PAS/PEO blends were made of two compositions: 1:1 molar ratio, and 1:2 (PAS:PEO) weigh ratio (1:7 molar ratio). DSC data showed that the blends are well mixed to each other.

Characterization: HETCOR and FSLG-HETCOR:

When the cross polarization time is longer than 500 us, the carbonyl carbon forms a contour with the nearby methyl protons. When increasing the cross polarization time, we can observe that the carbonyl groups form contours with PEO's methylene groups.

The future work will focus on development of FSLG-LGCP HETCOR pulse sequence.

functional groups in the alkylammonium cations can react with the polymer matrix to form more stable polymer clay nanocomposites.

Polymers and solvents:

Polycarbonate (PC), polyethylene oxide (PEO), and polypropylene (PP) were used to form clay nanocomposites. Solvents were the following: THF, Cyclohexane, toluene and methylene chloride.

Nanocomposites made:

The following polymer clay nanocomposites were made.

5%, 10%, 15%, 20% weight percent of 30B MMT-PC were made by using methylene chloride solution-cast method.

5% Na⁺ MMT-PC was made by using methylene chloride solution cast method.

5% 25A MMT-PC was made by using methylene chloride solution cast method.

5% Na⁺ MMT-PEO was made by using THF solution cast method.

5% 25A MMT-PEO was made by using THF solution cast method.

5% 30B MMT-PP was made by using cyclohexane solution cast method.

In order to get the solution cast method work, one has to find a suitable solvent. In general, the polymer should be soluble, and the clay should be swellable. For some rarely soluble polymers, such as polypropylene, we found that it is a practical way to find a solvent which has the similar solubility parameter as the polymer. For example, at first we tried to use toluene, solubility parameter is $8.9 \text{ cal}^{1/2} \text{ cm}^{-3/2}$, to dissolve

polypropylene, solubility parameter is 7.9. But even heated up to 120 degree, there were some small pieces of PP in the solution. After we used cyclohexane, whose solubility parameter is 8.2, after heated at about 50-60 degrees, we can get a homogeneous solution system.

Characterization of Nanocomposites:

There are three types of nanocomposites:

Intercalated nanocomposites: the insertion of a polymer matrix into the interlayer occurs regardless of the clay to polymer ratio.

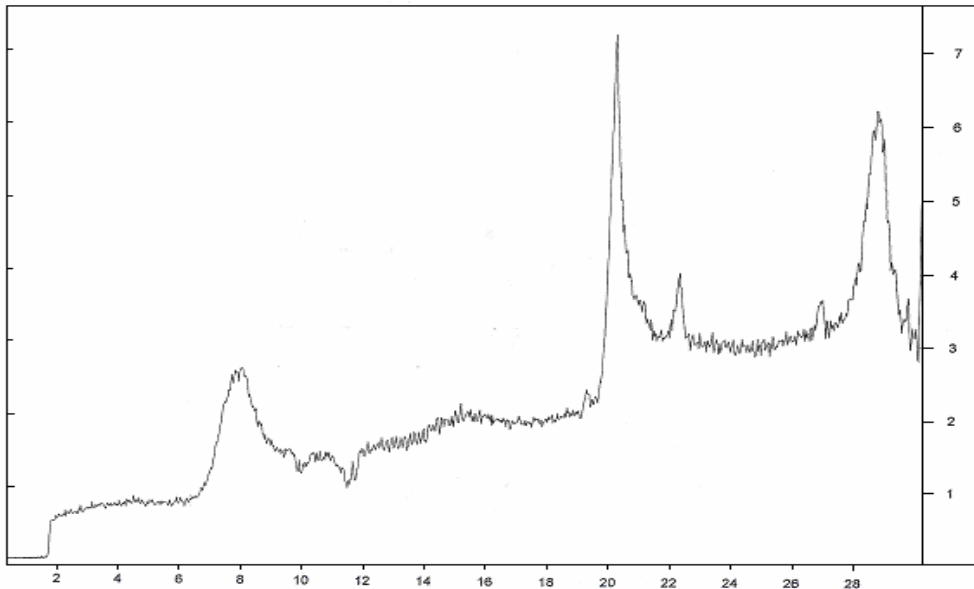
Flocculated (aggregated) nanocomposites: silicate layers are sometimes flocculated due to hydroxylated edge-edge interaction of the silicate layers.

Exfoliated nanocomposites: the individual clay layers are separated in a continuous polymer matrix by an average distances that depends on clay loading. The clay to polymer ratio is usually smaller than the intercalated nanocomposites.

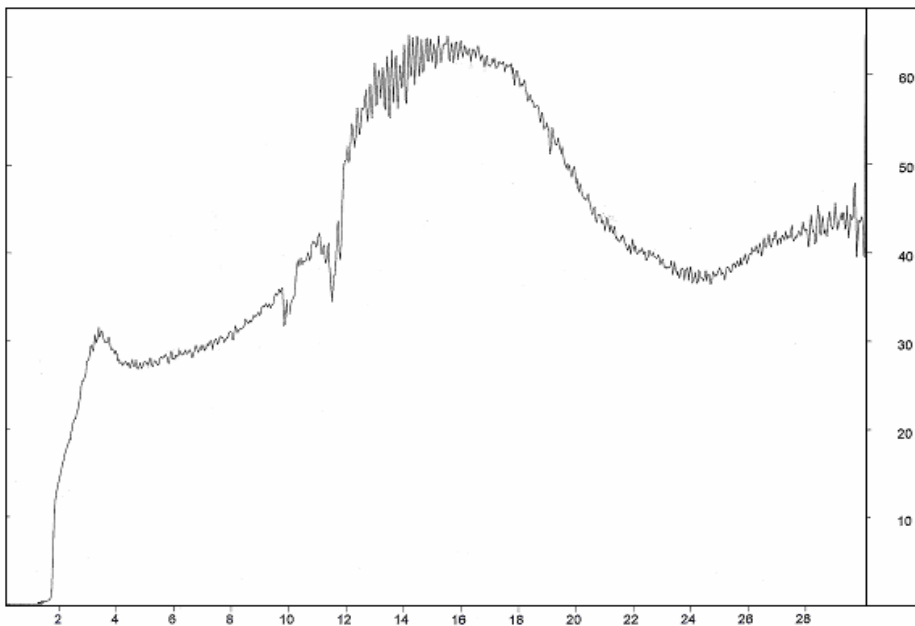
The two traditional techniques for characterization of structures of nanocomposites are WAXD analysis and transmission electron micrographic (TEM) observation.

In WAXD method, by monitoring the position, shape, and intensity of the basal reflections from the distributed silicate layers and interlayers, and by using the Bragg's law, which is $d = \gamma / (2 \sin \theta)$, one can identify the structures of nanocomposites. The following are some of WAXD patterns of the polymer nanocomposites. The disappearance of the coherent X-ray diffraction from the distributed silicate layers of the pure clay at nanocomposites associated the formation of exfoliated nanocomposites.

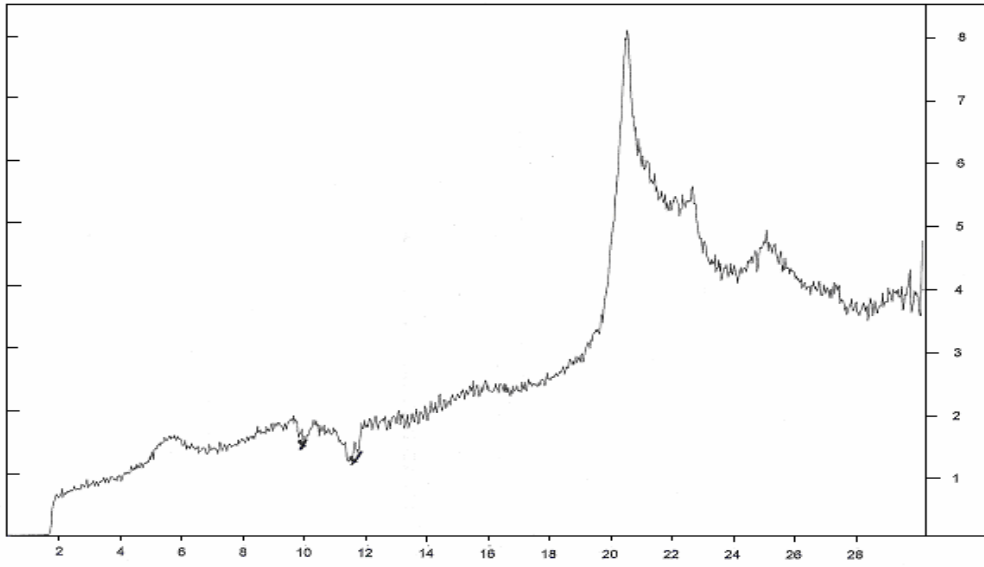
While the appearance of a new basal reflection corresponding to the larger gallery size associated the intercalated nanocomposites. The 5% Na⁺ MMT-PC nanocomposite is one intercalated nanocomposites. Also from the WAXD pattern of 15% 30B MMT-PC, there are two basal reflections. The nanocomposites structure associates the formation of both intercalation and flocculation.



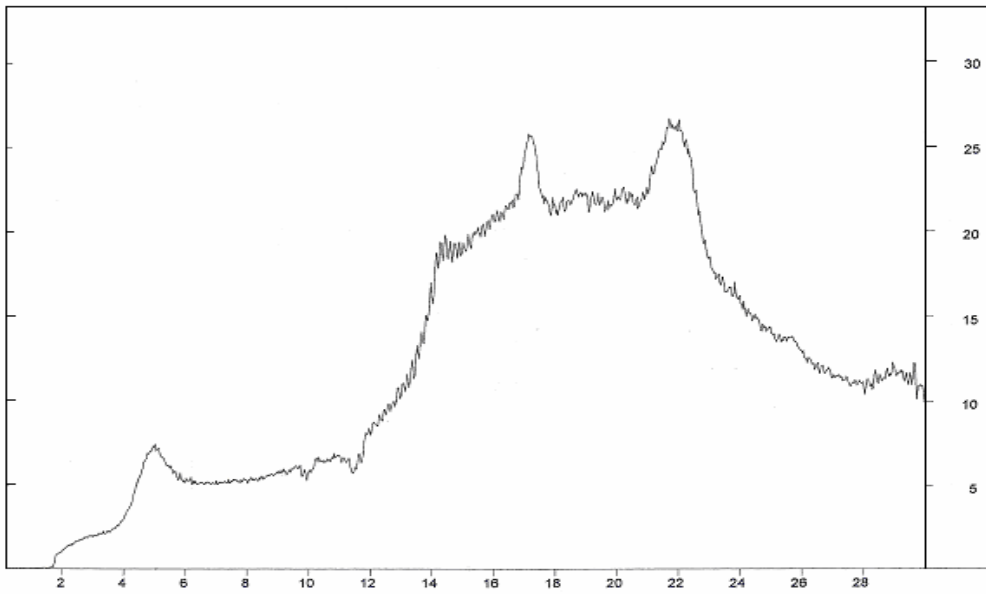
Wide Angle X-ray diffraction for MMT Na⁺ cloisite



WAXD graph for nanocomposite PC-Na⁺ cloisite

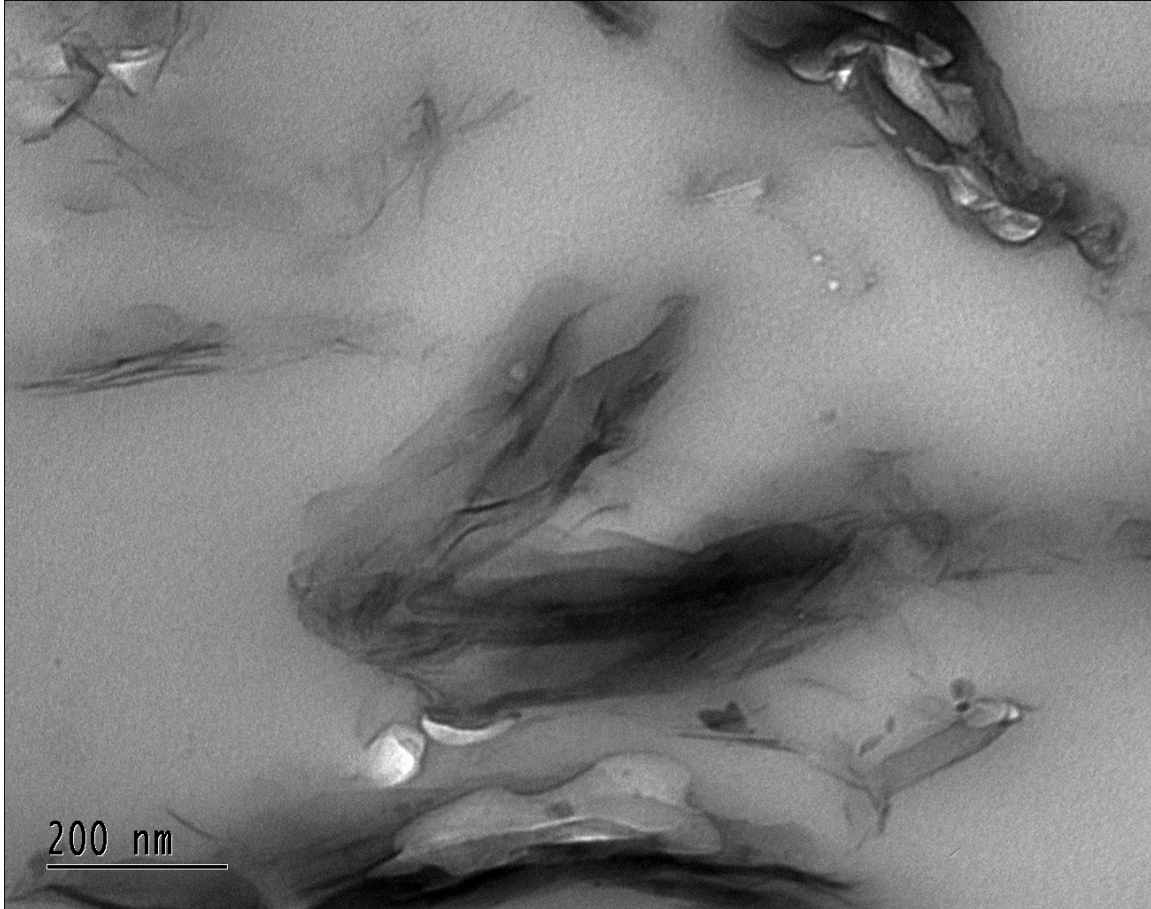


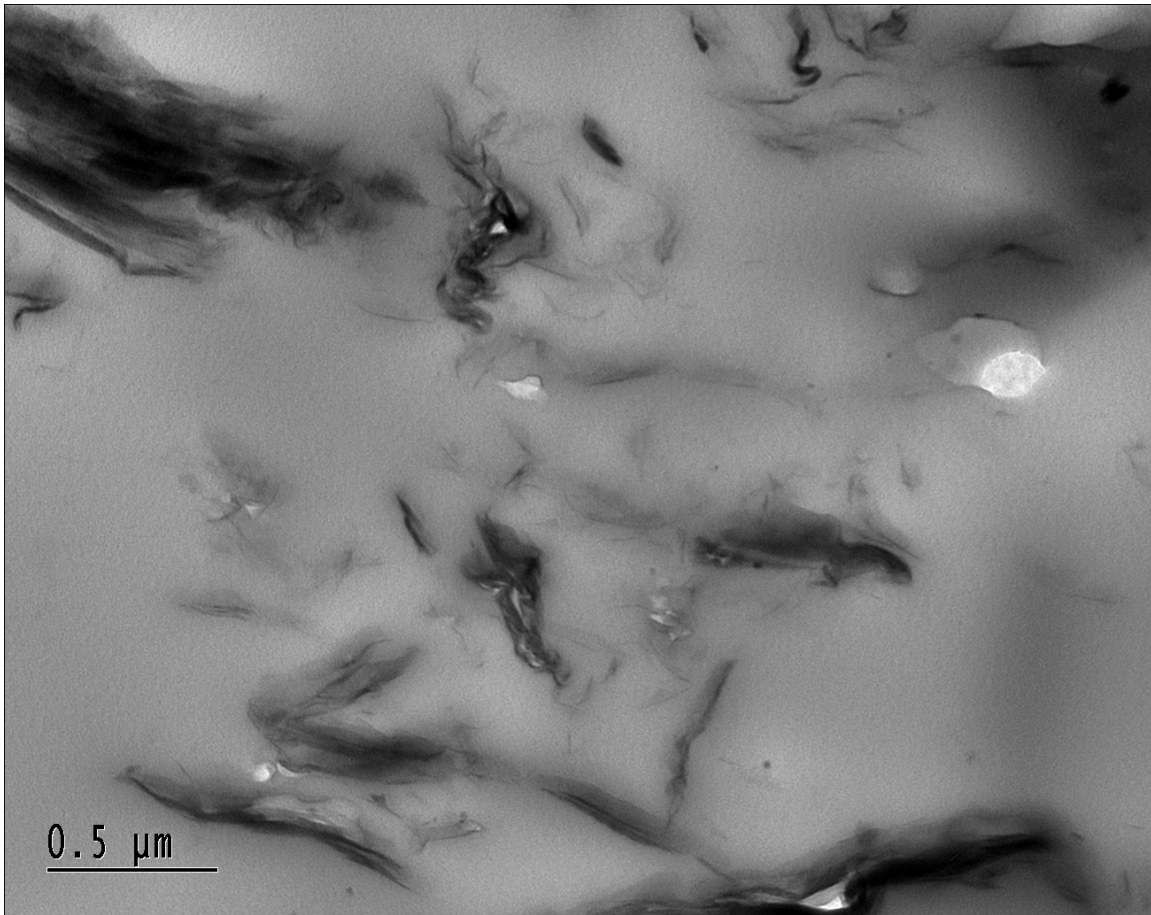
WAXD graph for MMT cloisite 25A



WAXD diffraction for nanocomposite PP-cloisite 25A

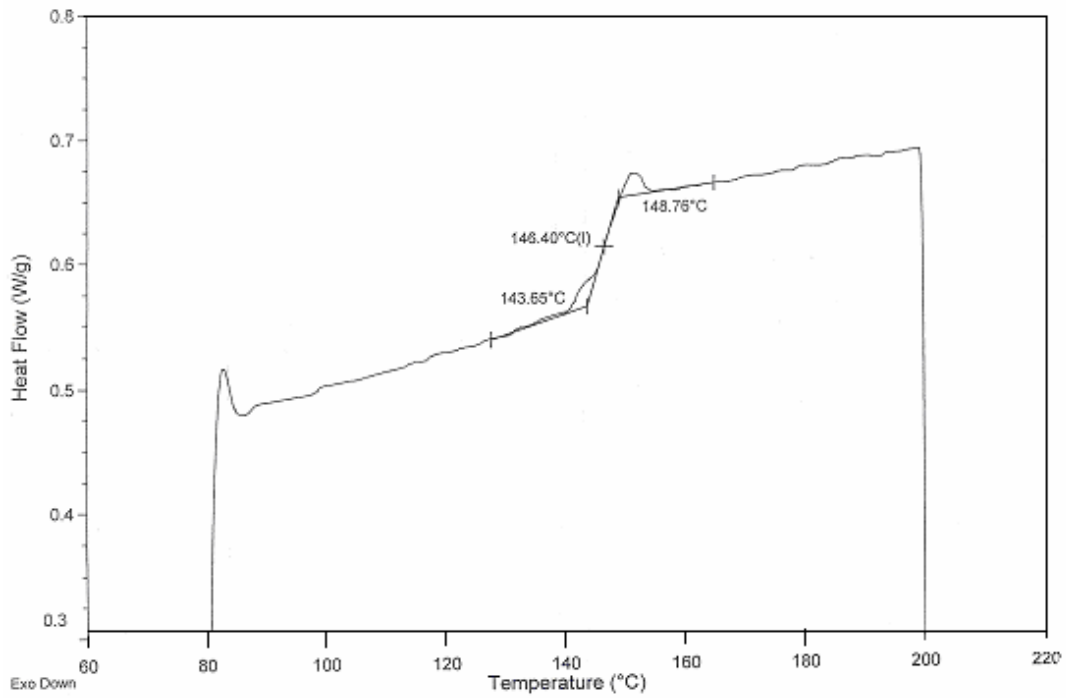
TEM directly visualizes the structure of nanocomposites. Here we had a TEM of 5% weigh percent 30B MMT-PC nanocomposites.



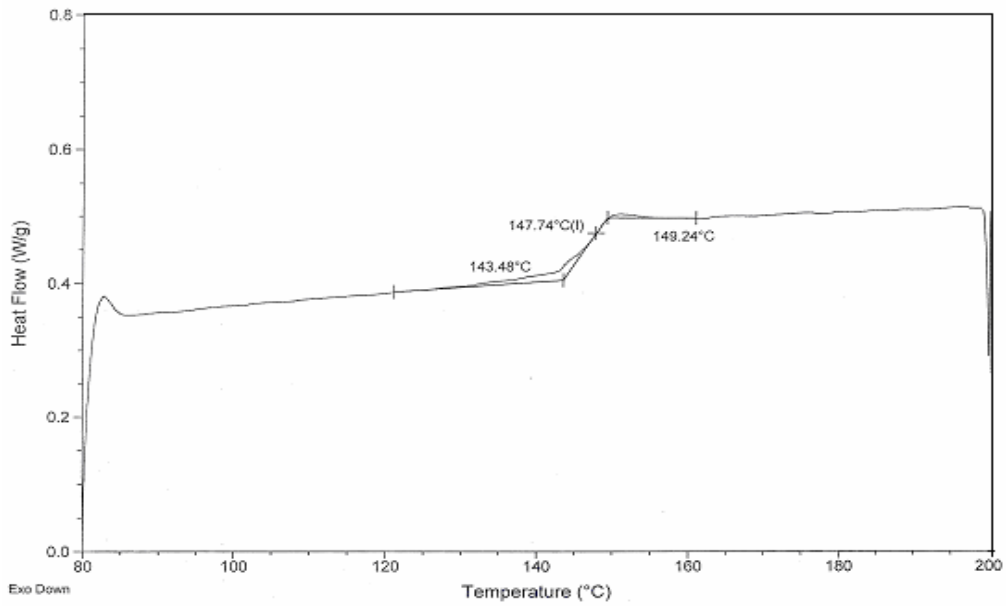


From WAXD, we know that it is an intercalated-flocculated structure. Now the TEM shows us the direct pattern of it.

We also have some DSC data of the 5% Na⁺ MMT-PC, 5% 25A MMT-PC, 5% 30B MMT-PC, 15% 30B MMT-PC nanocomposites. From these data, we can see that the formation of polymer-clay nanocomposites do change some mechanical behaviors of the polymers.



DSC of pure PC



DSC of nanocomposite PC-Na⁺ cloisite

Solid-state NMR is a relatively new tool to investigate the morphology, surface of polymer-clay nanocomposites. The CPMAS spectra can show the movements of the chemical shift of carbon in the polymer before and after it forms a nanocomposites.

We also tried to use multidimensional NMR to characterize the polymer-clay nanocomposites.

The future work will focus on (1) developing a successful solution cast preparation of various polymer-clay nanocomposites, (2) using solid-state NMR to characterize the structure of nanocomposites,(3) finding the driving force of forming exfoliated polymer-clay nanocomposites.